

University of Alberta

STUDY OF BUBBLE-FLAT SURFACE INTERACTIONS

by

Aref Seyyed Najafi

A thesis submitted to the Faculty of Graduate Studies and Research
in partial fulfillment of the requirements for the degree of

Doctor of Philosophy

in

Chemical Engineering

Chemical and Materials Engineering

© Aref Seyyed Najafi
Spring 2010
Edmonton, Alberta

Permission is hereby granted to the University of Alberta Libraries to reproduce single copies of this thesis and to lend or sell such copies for private, scholarly or scientific research purposes only.

Where the thesis is converted to, or otherwise made available in digital form, the University of Alberta will advise potential users of the thesis of these terms.

The author reserves all other publication and other rights in association with the copyright in the thesis and, except as herein before provided, neither the thesis nor any substantial portion thereof may be printed or otherwise reproduced in any material form whatsoever without the author's prior written permission.

Examining Committee

Jacob Masliyah, Chemical and Materials Engineering

Zhenghe Xu, Chemical and Materials Engineering

Tony Yeung, Chemical and Materials Engineering

Subir Bhattacharjee, Mechanical Engineering

Marek Pawlik, Mining Engineering, University of British Columbia

TO MY PARENTS

ABSTRACT

Canada has the largest known reserve of oil in the world in the form of oil sands: an estimated 1.7 to 2.5 trillion barrels of oil are deposited in combination of the sand, water and clay.

The presented research is devoted to bubble-solid surface interaction, which is one of the critical areas of the oil sand processing and it is also a key point for many other processing technologies, such as mineral recovery, froth flotation, soil remediation, de inking of paper, heat transfer in boilers tube, biological and medical sciences.

The goal of this work was to investigate new theoretical and practical approaches, which would help in better understanding of fundamentals of the flotation process in oil sands extraction. Among many achievements of this research are:

- 1) development of the method for generation of a single micro bubble. Dependence of this process on micropipette tip size and inclination, gas type, taper length and other parameters has also been studied (Chapter 3);
- 2) study of gas bubble - flat surface interactions based on a practical approach of determination of two dynamic parameters, sliding velocity and induction time of a gas bubble. Various types of gas bubbles (CO_2 , Air, H_2 , and O_2) and collector surfaces (bitumen, treated hydrophobic and hydrophilic silica) were used in sliding velocity and induction time measurements. The sliding velocity of gas bubbles under an inclined

collector surface was found to be in a strong dependence of water chemistry, type of gases, temperature, initial separation between bubble and collector surface (Chapter 4);

3) developing an analytical model for predicting bubble sliding velocity based on previously developed models. The model was in a good agreement with experimental results (Chapter 5);

4) establishing a new method for bubble zeta potential measurements. The measurements were in a good agreement with previously studies reported in literature (Chapter 6).

Summarized above findings from this research represent valuable advances in understanding oil sands processing. The prospects of future work are provided in Chapter 8.

ACKNOWLEDGEMENTS

I am grateful to my supervisors, Drs. Jacob Masliyah and Zhenghe Xu, for their support and encouragement. I appreciate their enthusiasm and advices through my research program.

I would like to thank my other Ph.D. committee members for their interest in my work.

I would like to thank members of the department of Chemical Engineering for collaboration and/or support.

This research was possible by funding provided from National Sciences and Engineering Research Council (NSERC) through Industrial Research Chair in Oil Sands Engineering held by Dr. Masliyah.

Finally, I would like to thank my wife, Sabina, for her understanding, patience and support.

TABLE OF CONTENT

Abstract

Acknowledgments

Table of content

List of tables

List of figures

Nomenclature

Chapter 1: Introduction

1.1 Oil sands deposit 1

1.2 Bitumen extraction 2

1.3 Objectives 4

Chapter 2: Literature review

2.1 Oil sands 5

2.2 Hydrotransport pipeline 7

2.3 Bitumen aeration 7

2.4 Source of air for primary flotation 8

2.5 Bitumen-air bubble approach and attachment 9

2.6 Aeration 11

2.7 Effect of conditioning parameters 14

2.8 Bubble dynamics 17

2.9 Summary 19

Chapter 3: Single micro bubble generation

3.1 Introduction 20

3.2 Concept for generation of single micro-bubbles	22
3.3 Experimental procedure	29
3.3.1 Bubble pressure	30
3.3.2 Reproducibility	31
3.4 Theoretical model for bubble generation from an inclined pipette	31
3.5 Results and discussion	
3.5.1 Effect of gas type	45
3.5.2 Effect of taper length	46
3.5.3 Effect of tip diameter on bubble size	46
3.5.4 Effect of micropipette inclination on bubble size	49
3.6 Conclusions	49
Chapter 4: Bubble sliding velocity and induction time	
4.1 Introduction	53
4.2 Experimental procedure	54
4.3 Results and discussion	61
4.3.1 Effect of temperature	62
4.3.2 Effect of bubble size	68
4.3.3 Effect of type of gas bubbles	68
4.3.4 Effect of surface wettability	72
4.3.5 Effect of dissolved air	77
4.3.6 Effect of surface non-uniformity	80
4.3.7 Effect of dissolved surfactants	84
4.4 Conclusions	87

Chapter 5: Experimental and theoretical study of single small bubble sliding motion along an inclined plate

5.1 Introduction	88
5.2 Experimental procedure	89
5.3 Equation of motion	93
5.3.1 Bubble motion in zone 1	95
5.3.2 Bubble motion in zone 2	96
5.3.3 Bubble motion in zone 3	98
5.4 Results and discussion	
5.4.1 Effect of plate inclination angle	100
5.4.2 Effect of temperature	105
5.4.3 Effect of bubble size	108
5.4.4 Effect of natural surfactant	110
5.4.5 Effect of calcium	113
5.4.6 Effect of surface wettability	115
5.5 Conclusions	115

Chapter 6: A novel method of measuring electrophoretic mobility of gas bubbles

6.1 Introduction	117
6.2 Novel approach for generation of small air bubbles	120
6.3 Experimental procedure	126
6.4 Zeta potential measurements	131
6.5 Results and discussion	

6.5.1 Effect of pH on zeta potential of air bubbles	135
6.5.2 Effect of electrolyte concentration	138
6.5.3 Effect of surfactant concentration	141
6.5.4 Zeta potential of bubbles in industrial process water	147
6.6 Conclusions	150
Chapter 7: Effect of colloidal forces on bubble and solid interactions	
7.1 Colloidal surface forces	151
7.1.1 van der Waals interaction	152
7.1.2 Electrostatic double layer (EDL) interaction	154
7.1.2.1 Electrical double layer force	154
7.1.2.2 Derjaguin approximation	156
7.2 Non DLVO forces	157
7.2.1 Hydrophobic force	157
7.2.2 Hydration force	158
7.2.3 Steric force	158
7.3 Classical DLVO and extended DLVO theory	158
7.4 Induction time measurement and calculation	159
Chapter 8. Summary and future work	
8.1 Research contributions	163
8.1.1 Single micro bubble generation	163
8.1.2 Sliding velocity and induction time results	163
8.1.3 Sliding velocity modeling	164
8.1.4 Bubble zeta potential measurements	165

8.2 Prospect of future work	165
Bibliography	167
Appendix A. Derivation of Plesset equation.	183
Appendix B. Effect of inclination angle on added mass force	186
Appendix C. Derivation of induction time equation	191

LIST OF TABLES

Table 3.1 Viscosity and density of gases used in this study	45
Table 4.1 Concentration of ions of interest in the industrial process water (pH = 8.3).	59
Table 4.2 Recipe used for the preparation of the simulated process water (pH = 8.1).	60
Table 6.1 Composition of air (Eaton and Franson, 2005).	121
Table 6.2 Coefficients for the calculation of Ne, N ₂ and Ar solubility from Equation (6-4) (Garcia and Gordon, 1992).	123

LIST OF FIGURES

Figure 3.1 A schematic diagram of the experimental set-up for single micro-bubble generation.	23
Figure 3.2 A schematic view of the pressure distribution on a micropipette tip for a non-flow system.	25
Figure 3.3 Bubble generation process and pressure variation with time.	28
Figure 3.4 Bubble detachment criterion: bubble will detach from a micropipette tip when its center travels a distance equal to the bubble radius R plus the micropipette radius, r_0 .	34
Figure 3.5 Separation of a bubble from micropipette tip with different inclination angle: a) downward inclination and b) upward inclination.	35
Figure 3.6 Effect of micropipette inclination angle on the back and front angles: a) $\Theta_{\text{Back}} \approx \Theta_{\text{Front}}$ and b) $\Theta_{\text{Back}} > \Theta_{\text{Front}}$.	36
Figure 3.7 Illustration of free body diagram of buoyancy and surface tension forces acting on the tip of the micropipette.	37
Figure 3.8 Experimental measurements and curve fit results of bubble front and back angles with respect to the inclination angle of micropipette.	41
Figure 3.9 Illustration of solution for bubble growth and motion of bubble center. The intersection point gives the bubble radius at detachment.	42
Figure 3.10 Maximum bubble pressure (P_{bubble}) as a function of tip diameter.	43

Figure 3.11 Absolute frequency and histogram of produced bubbles in a given size (micropipette I.D. =7 μm , inclination angle = 150° , taper length = 17mm).	44
Figure 3.12 Effect of gas type on the produced bubble size (micropipette I.D. = 13 μm , inclination angle = 150° , taper length = 17 mm).	47
Figure 3.13 Effect of taper length on the size of air bubbles (micropipette I.D. = 5 μm , inclination angle = 150°).	48
Figure 3.14 Effect of tip diameter on the diameter of generated air bubbles (micropipette inclination angle = 150° , taper length = 27 mm).	51
Figure 3.15 Effect of inclination angle on the diameter of generated bubbles (micropipette I.D. =13 μm , taper length = 17 mm).	52
Figure 4.1 Bubble rising, transient and sliding velocity profiles. A crossing point of tangents of sliding velocity and transient velocity profiles is defined as the zero time point.	57
Figure 4.2 Effect of temperature on interaction of rising air bubbles (bubble diameter, $D = 0.22 \text{ mm}$) with a hydrophobic silica surface immersed in process water (surface inclination = 60°).	65
Figure 4.3 Effect of temperature on interaction of rising CO_2 bubbles (bubble diameter, $D = 0.22 \text{ mm}$) with the hydrophobic silica surface in process water (surface inclination = 60°).	66
Figure 4.4 Effect of temperature on induction time and viscosity of water (bubble diameter, $D = 0.254 \text{ mm}$).	67
Figure 4.5 Velocity profile of air and CO_2 bubbles (open	70

symbols for $D = 0.23$ mm and filled symbols for $D = 0.275$ mm) toward and along hydrophobized silica surface in process water (surface inclination = 60° , $T = 23^\circ\text{C}$).

Figure 4.6 Effect of gas types on bubble rising and sliding velocities ($D = 0.23$ mm) toward the hydrophobized silica surface in process water (surface inclination = 60° , $T = 23^\circ\text{C}$).

Figure 4.7 Effect of collector surface types on bubbles (bubble diameter, $D = 0.25$ mm) rising and sliding velocities in process water (surface inclination = 60° , $T = 23^\circ\text{C}$).

Figure 4.8 Effect of surface type (uniform bitumen surface and hydrophobic silica surface) and gas type (air and CO_2) on dynamic contact angle variation in process water.

Figure 4.9 Effect of de-aeration of process water on bubble rising and sliding velocities ($D = 0.25$ mm) with hydrophobized silica surface at surface inclination of 60° and $T = 23^\circ\text{C}$.

Figure 4.10 Schematic representation of a surface non-uniformity effect on bubble attachment.

Figure 4.11 Micrograph of: (A) hydrophobized silica surface; (B) teflon plate; (C) non-uniform layer of bitumen on teflon surface; and (D) uniform bitumen layer on teflon surface.

Figure 4.12 Effect of surface non-uniformity on bubble rising and sliding velocities ($D = 0.25$ mm) in process water with surface inclination 60° and $T = 23^\circ\text{C}$.

Figure 4.13 Effect of surfactants on oxygen bubble's rising and sliding velocities ($D = 0.25$ mm) with uniform layer bitumen surface in process water and simulated process

water at surface inclination of 60° and $T = 50^\circ\text{C}$.

- Figure 5.1 Experimental apparatus for micro-bubble generation by electrolysis. 92
- Figure 5.2 Sliding of a hydrogen bubble under a silica wafer surface, $D = 0.35\text{ mm}$, $T = 23^\circ\text{C}$. 102
- Figure 5.3 Effect of surface inclination on sliding velocity of hydrogen and oxygen bubbles under a hydrophilic silica wafer surface, $D = 0.35\text{ mm}$, $T = 23^\circ\text{C}$. 103
- Figure 5.4 Effect of inclination on rising velocity of hydrogen bubbles ($D = 0.35\text{ mm}$) under a hydrophilic silica surface ($T = 23^\circ\text{C}$). 104
- Figure 5.5 Effect of temperature on water viscosity and bubble ($D = 0.3\text{ mm}$) terminal velocity. 106
- Figure 5.6 Effect of temperature on bubble velocity ($D = 0.3\text{ mm}$) under an inclined hydrophilic silica wafer surface (surface inclination = 60°). 107
- Figure 5.7 Effect of bubble size on hydrogen bubble velocities sliding under a silica wafer surface (surface inclination = 45°), $T = 23^\circ\text{C}$. 109
- Figure 5.8 Comparative analysis of the effect of bubble size on its terminal velocity, calculated for clean or contaminated water environment and compared with the measured values for oxygen bubbles. 111
- Figure 5.9 Effect of surfactants on oxygen bubble rising and sliding velocities ($D = 0.25\text{ mm}$) under a uniform layer of bitumen coated on a silica surface in process water and simulated process water (surface inclination = 60° and $T = 50^\circ\text{C}$). 112

Figure 5.10 Effect of calcium addition on oxygen and hydrogen bubble rising and sliding velocities ($D = 0.25$ mm) against silica surface in process water and simulated process water with surface inclination = 30° and $T = 50$ °C.	114
Figure 5.11 Effect of surface wettability on the bubble sliding velocity ($D = 0.25$ mm) towards silica and bitumen layer surface in process water with surface inclination = 60° and $T = 50$ °C.	116
Figure 6.1 Effect of temperature on concentration of dissolved oxygen, nitrogen, and air in water.	125
Figure 6.2 Schematic of the column used in fractionation of the industrial process water.	129
Figure 6.3 Schematic of a cell with the Uzgiris electrode of the Brookhaven ZetaPALS instrument equipped with a temperature control system. A) before heating (no nano-bubble) and B) after heating, (with nano-bubbles nucleated in the form of a dispersion).	133
Figure 6.4 Two photographs with a laser beam passing through the cuvette filled with the air-saturated water: a) temperature of water as saturated at 8 °C, b) temperature of air-saturated water raised to 23 °C. A scattered beam is observed on photograph (b) due to Tyndall effect caused by nucleated bubbles dispersed in water.	134
Figure 6.5 Variation with pH of zeta potential of air bubbles in 0.01 M NaCl solution.	137
Figure 6.6 Zeta potential of air bubbles dispersed in 0.0001 M SDS solution of (pH 6.5) with dissolved salts of varying concentrations.	140

Figure 6.7. Zeta potential of air bubbles in SDS at pH = 7.0.	144
Figure 6.8 Effect of pH on zeta potential of air bubbles in 0.001 M solutions of SDS.	145
Figure 6.9 The effect of pH on zeta potential of air bubbles in 0.001 M DAH solutions.	146
Figure 6.10 Zeta potential of air bubbles in industrial process water, its foam and residual fractions, and simulated process water with increasing concentration of CaCl ₂ . pH of solution was adjusted by CO ₂ gas to pH 8.15 ± 0.10.	149
Figure 7.1 Experimental and calculated induction time values for rising air bubbles (D = 0.22 mm) towards a hydrophobic silica surface in water (surface inclination = 60°), $\psi_{\text{Silica}} = -20$ mV (Yordan, 1989), $\psi_{\text{Bubble}} = -45$ mV, $H_{\text{cr}} = 110$ nm (Yordan, 1989), $K_{123} = 6.13 \times 10^{-19}$ (Yoon and Aksoy, 1999), $A_{132} = -3.12 \times 10^{-21}$.	162
Figure B.1 Added mass force on a spherical bubble.	189
Figure B.2 Effect of inclination on added mass force.	190
Figure C.1 Schematic gas bubble approaching a planar collector surface.	196

NOMENCLATURE

D	Bubble diameter (mm)
F	Net driving force acting on the bubble (N)
g	Acceleration due to gravity (m/s^2)
L	Micropipette taper length (m)
h	Distance between top of the bubble and planar collector surface (m).
h_0	Initial thickness of liquid film between bubble and planar collector surface (m).
h_{cr}	The critical thickness of liquid film (m).
H	Parameter defined for h (m).
P_o	Atmospheric pressure (Pa)
P_C	Capillary pressure (Pa)
P_B	Pressure inside the bubble (Pa)
P_L	Pressure outside the bubble (Pa)
P_{bubble}	Maximum bubble pressure (Pa)
r_c	Radius of capillary (m)
r_o	Radius of micropipette tip (m)
R	Curvature radius of bubble (m)
R_b	Radius of bubble (m)
R_x	Radius of deformed bubble in x direction (m)
R_z	Radius of deformed bubble in z direction (m)
\dot{R}	First derivative of bubble radius to time
\ddot{R}	Second derivative of bubble radius with time

t	Time (s).
$t_{\text{induction}}$	Induction time (s).
V	Bubble rise velocity toward planar collector surface (m/s).
v_r	Velocity component at r direction (m/s).
v_z	Velocity component at z direction (m/s).
V_b	Volume of the bubble at time t (m^3)
U	Velocity of bubble growth (m/s)
\dot{U}	Acceleration of bubble growth (m/s^2)
z	Bubble center travel distance (m)

Greek symbols:

α	Inclination of micropipette (degrees)
θ	Inclination of a inclined flat solid surface (degrees)
θ_F	Front angle (degrees)
θ_B	Back angle (degrees)
μ_G	Gas viscosity (Pa.s)
μ_L	Liquid viscosity (Pa.s)
ρ_G	Density of gas (kg/m^3)
ρ_L	Density of liquid (kg/m^3)
μ	Viscosity of liquid (Pa.s)
ρ	Density of liquid (kg/m^3)
σ	Surface tension (Nm)
γ	Surface tension of liquid (mN/m)

CHAPTER 1: INTRODUCTION

“It is time that a theory for hot water separation should commence to emerge”

Karl Clark, 1944

1.1 Oil sands deposit

Alberta's oil sands deposits, which called tar sands deposits as well, contain the biggest known reserve of oil in the world. An estimated 1.7 to 2.5 trillion barrels of oil are trapped in a complex mixture of sand, water and clay (Camp, 1976, 1977; Masliyah, 2003). One of the theories, which describe the formation of oil sands suggests that light crude oil from southern Alberta migrated north and east with the same pressures that formed the Rocky Mountains. With time, due to bacterial action, light crude transformed into bitumen (Conybeare, 1966; Vigrass, 1999). Bitumen is much heavier, carbon rich, and viscous oil. Three main oil sand deposits are located in Peace River, Cold Lake and Athabasca. The Athabasca oil sands deposits are the largest and closest to the surface. It resulted in large-scale open pit mining operations and oil sands development around Fort McMurray.

Recent high crude oil prices have attracted many companies to invest in the oil sands processing industry. The processing of oil sands includes mining oil sands, extracting bitumen from the mined oil sands, and upgrading the extracted bitumen to produce “synthetic crude oil”.

Currently, more than 700,000 barrels of crude oil are produced daily through mining, extraction and upgrading operations from the Athabasca oil sands deposit at Syncrude Canada Ltd., Suncor Energy Ltd. and Albian Sands. Moreover, many new oil sands mining plants in some companies such as CNRL became operational in the late 2008.

The major target in oil sands extraction process research is to obtain maximum bitumen recovery with minimum impact on the environment. To achieve such a goal it is necessary to understand the extraction process and factors which affect the process.

1.2 Bitumen extraction

In spite of different processes available for bitumen extraction, such as solvent extraction, supercritical fluid extraction, microbial extraction, direct coking, olephilic sieving, or spherical agglomeration, a variation of the hot water extraction process (HWEP), is the only one commercially used in oil sands industry. HWEP was pioneered by Clark in the 1920's (Hepler and Hsi, 1989; Hepler and Smith, 1994). Extensive amount of research during last decades made this process profitable and well developed. (Hepler and Hsi, 1989; Hepler and Smith, 1994; Masliyah et al., 2004).

In the HWEP process, the following fundamental steps are involved: liberation (separation) of bitumen from sand grains; aeration (attachment or engulfment, depending on the process temperature) of the liberated bitumen to air bubbles; and flotation of bitumen-air bubble aggregates to

the top of slurry to form a bitumen-rich froth. At Syncrude, the froth product is diluted with naphtha, and centrifuged to remove the remaining solids and water. The final bitumen is further upgraded by thermal cracking and/or catalytic hydrocracking to synthetic crude oils.

Although there have been significant advances in understanding and describing water based extraction process after Clark's pioneering work, many mechanisms remain poorly understood. Full understanding the sub-processes of a bitumen extraction system is essential to improve the efficiency of bitumen extraction. As indicated, in the HWEP, liberation of bitumen from sand grains and the subsequent stabilization against hetero-coagulation of the liberated bitumen with sand grains (silica and clay particles) are one of prerequisites for bitumen recovery. The attachment of bitumen with air bubble is critical for the liberated bitumen droplet to float. The size of bitumen droplets has a great impact on the attachment between bitumen droplets and air bubbles. Therefore, understanding interactions between bitumen/sands/bubble, which are dominated by their interfacial properties, is of great interest to researchers and of great importance to bitumen extraction process in industry.

Fundamental studies of bitumen extraction are highly appreciated and have been well developed so far. Many hypotheses and experimental methods have been proposed / developed to explain the mechanism of observed phenomena. Still there are many subjects which remain open for further investigation.

1.3 Objectives

The objectives of this work are to investigate the interactions between air bubble and solid collector surfaces, including bitumen surfaces. The target of this research is to advance the current knowledge and provide direct and indirect insights into bitumen extraction mechanism.

In this study two novel techniques were developed to study the fundamentals of water based bitumen extraction process. More specifically, we intend to:

- Generate micro size bubbles, in order to avoid bubble deformation in large bubbles, when studying bubble-solid surface interaction;
- Study the surface properties such as electrokinetics of bubbles, and understand the effect of surfactants on bubble surface charges to provide the basis for further studies on the interactions between the components in oil sands processing systems;
- Investigate the effect of the industrial operation parameters such as temperature, solution pH, salinity, and divalent ions on the interactions between oil sand components;
- Study sliding velocity of air bubble solid surfaces;
- Study induction time and bubble attachment to bitumen or solid surfaces;
- Establish optimum conditions for bitumen flotation.

CHAPTER 2: LITERATURE REVIEW

In this thesis, interaction of a micro size rising single bubbles against an inclined wall is studied. In this section, a bitumen extraction process will be reviewed in depth to establish the needs of this research.

2.1 Oil sands

The oil sand ore is a mixture of bitumen, sand grains and water. Knowledge of the structure of these materials helps to have a better understanding of extraction process, especially the conditioning step. The composition and structure may differ from one ore to another (Drelich, 1996), which is the origin of complications related to extrapolating results gained from one ore to the other ores.

Oil sands ore can be classified according to their bitumen content as: poor ore, which contains 6~8% bitumen, medium ore, which contains 8~10% bitumen and good ore, which contains more than 10% bitumen.

The oil sands extraction can be classified on the basis of solid wettability into two categories, water-wet sand and oil-wet sand. For the water-wet sand the extraction of bitumen from the oil sands ores is economically attractive, and bitumen can be extracted with water-based technology. Canadian oil sands deposits are mainly water-wet. Another type is oil-wet sand, which can be found in Utah oil sands deposits. Extraction of such deposits requires solvent-based extraction technology.

Water-Based Extraction Process (WBEP)

Hot water extraction process (HWEP) was developed by Dr. Clark for separation of bitumen from oil sands in 1920's. Clark's work was the basis for massive amount of research and developments toward commercial realization of HWEP (Hepler and Hsi, 1989; Hepler and Smith, 1994).

In HWEP, mined ore is mixed with caustic water and steam to obtain a slurry of pH 8~8.5 and 80°C. Liberated bitumen creates oil dispersion in water. Meanwhile air bubbles are blown in the slurry and bitumen droplets attach to introduced air bubbles. In a separation vessel bitumen droplets float to the top as froth product and coarse sands settle to the bottom as tailings.

Typical composition of produced froth is 60% bitumen, 30% water and 10% solids. The produced froth is diluted by adding naphtha to allow the remaining sand and water to be removed. After removal of added naphtha, the product is called bitumen. The produced bitumen is then upgraded to produce synthetic crude oils.

The Hot Water Extraction Process (HWEP) can be divided into two major sub processes: the first is conditioning, in which bitumen is liberated from the sand grains and the resultant bitumen droplets attach to the air bubbles. This process occurs in hydrotransport pipeline, tumblers or/and stirred tanks. The second is flotation step, in which bitumen-air bubble aggregate is separated from most of the minerals and water in the PSV.

After successful commercialization of the HWEF, producers and researchers concentrated on reducing operating and increasing bitumen recovery and minimizing environmental impacts to have sustainable operation. The output of such effects was the development of Low Temperature Bitumen Extraction Process (LTBEP), which was patented in 1990 (Sury, 1990, 1992).

In this process, hydrotransport pipeline is introduced. The oil sands are slurred in a hydrotransport pipeline at temperature around 40-55°C. Hydrodynamic and shear forces assist in bitumen liberation while air is introduced into the pipeline to increase air-bitumen attachment efficiency.

2.2 Hydrotransport pipeline

Mixing the ore with water and pumping the mixture to the plant are considered as the most practical and economic method. This pipeline is called hydrotransport pipeline. Part of extraction process, i.e. conditioning occurs in the hydrotransport pipeline as the slurry travels in pipeline.

2.3 Bitumen aeration

Removing liberated bitumen from water and clean sands is one of the key steps in Clark's HWEF (Clark, 1923). Since bitumen and water have similar densities, one way to separate them is by reducing the effective density of the bitumen. This is accomplished by aeration of the bitumen. In the early stage of the process development, Clark did not know why bitumen floated to the surface as froth (Clark, 1929). Later, he proposed

that the conditioned slurry contained entrained air that attaches to oil drops to float the bitumen (Clark, 1944).

Understanding of bitumen flotation mechanism requires fundamental knowledge of hydrodynamics and surface chemistry of particles and bubbles (Okada et al., 1990).

Early theories of the surface forces involved in bitumen aeration were based on calculation of electrical double layer and van der Waals forces (DLVO theory) (Takamura and Wallace, 1988; Takamura and Chow, 1985). Later studies have shown the important role of hydrophobic forces and thermodynamics when dealing with low energy bitumen surfaces (Zhou et al., 1998).

2.4 Source of air for primary flotation

Potential source for air in primary flotation can be the air entrapped in the mined ores, air dissolved in process water, and air entrained in the tumbler, screening or pumping stages.

Direct observation of ore samples placed in water indicated air bubbles originated from the ores (Drelich et al., 1996; 1995). The hydrophobic nature of the bitumen in the ore inhibited immediate penetration of the water, leading to trapped bubbles of air.

2.5 Bitumen-air bubble approach and attachment

Bitumen-air bubble attachment includes several sub processes: bubble approaching bitumen (collision frequency), thinning and rupture of the water layer between bitumen and bubble (induction time), and attachment. The probability of bitumen aeration is the product of the probabilities of collision, attachment and retention (Yoon and Luttrell, 1989). The collision is determined by hydrodynamic conditions, the attachment by interfacial forces, and the retention is a function of the adhesion and turbulence in the liquid.

A shorter induction time, solid free bitumen and optimal bubble size are favourable conditions for air bubble-bitumen attachment.

Particle collision

Drelich et al. (1995) observed that a bitumen droplet did not have to detach from the mineral matrix to aerate. They speculated that this might provide an advantage for aeration as the kinetic energy of collision between such a particle and an air bubble would be much greater than that between bitumen droplets and air bubbles leading to increased collision. The increased kinetic energy also helps to overcome electrostatic repulsive forces for improved attachment of bitumen to air bubbles.

There are two mechanisms, by which an air bubble can attach to a bitumen droplet for flotation once contact has been made (Bowman, 1968; Leja and Bowman, 1968):

Air bubble attaches at a discrete contact point if:

$$\gamma_{b/w} + \gamma_{w/a} > \gamma_{b/a}$$

Bitumen forms a film around the air bubble (engulfment) if:

$$\gamma_{w/a} > \gamma_{b/w} + \gamma_{b/a}$$

where $\gamma_{w/a}$ is the water/air surface tension, $\gamma_{b/a}$ the bitumen/air surface tension, and $\gamma_{b/w}$ the bitumen/water interfacial tension. As $\gamma_{w/a}$ is greater than $\gamma_{b/w} + \gamma_{b/a}$ under conditions of the Clark's hot water process (80°C, and pH 8.5, $\gamma_{w/a}$ is more than 50 mN/m, $\gamma_{b/a}$ is less than 30 mN/m, and $\gamma_{b/w}$ is about 10 mN/m), the second scenario should happen (Leja and Bowman, 1968) and bitumen should spread over the air bubble.

It is possible to predict engulfment by calculating the spreading coefficient (S) for bitumen on air (Drelich et al., 1996; Moran et al., 2000; Drelich and Miller, 1994 ; Adamson, 1982):

$$S = \gamma_{w/a} - \gamma_{b/a} - \gamma_{b/w}$$

A positive S means engulfment. It has been found that S can have a positive value at varying ionic strength and different pH (Moran et al.,

2000; Drelich and Miller, 1994). Drelich et al. (1996) found that equilibrium at the bitumen/air/water system causes a change in spreading coefficient, from a positive value to zero and even a negative value, as a result of surfactant migration which reduces surface tension.

Engulfment of air bubbles occurs in two stages: a rapid spreading of a thin bitumen film on the air/water interface followed by slower engulfment of bulk bitumen. (Drelich et al. 1995; 1996). The formation of a thick bitumen layer on air bubbles is dependent on temperature and spreading time, which decreases rapidly with increasing temperature (Drelich et al. 1995; 1996; Alexander and Li, 1996).

Drelich et al. (1996) proposed more complex mechanism, in which, instead of complete engulfment of an air bubble, the thin film of bitumen on the bubble can have a thicker patch of bitumen containing fine hydrophobic particles. These hydrophobic particles prevent the spreading of the bitumen.

2.6 Aeration

Yoon and Mao (1996) described the process of bubble-particle attachment in flotation. Whether a particle will attach to a bubble depends on DLVO forces (London - van der Waals, and electrostatic) as well as on attractive non-DLVO force that has been called the hydrophobic force.

Impinging jet (Dabros et al., 2000), micro bubble (Moran et al., 2000), single bubble (Gu et al., 2003) and induction time experiments showed

that increasing pH results in a decrease in air bubble attachment to bitumen surfaces. They also found that increasing ionic strength at alkaline pH affects the electrical double layer interaction, which has a major effect on bubble-bitumen interaction.

Dabros et al. (2000) reported that increase in pH causes a significant reduction in bubble-bitumen attachment as a result of increasing negative charge on the bitumen surface, which leads to a stronger repulsion between negatively charged bubble and bitumen

Impinging jet experiments shows that a higher flow intensity of air bubbles improves the bitumen-air bubble attachment.

Describing the attachment of negatively charged air bubbles and bitumen is a challenging task. Hydrophobic attractive force is an essential factor in bubble bitumen attachment (Yoon and Mao, 1996). Yang et al. (1999) showed the possibility of negatively charged air bubbles attaching to negatively charged surface even in the absence of hydrophobic force with repulsive van der Waals forces.

They attributed this phenomenon to asymmetric electric double layer attraction between particles of the same sign of charge but of different potentials.

The size of air bubble and bitumen droplet is an important factor in the attachment process. Yoon and Mao (1996) showed that smaller bubbles have higher attachment to both fine and coarse particles. Alexander and Li

(1996) showed that the probability of bitumen-bubble attachment increases with increasing the size ratio of bitumen droplets to air bubbles. They concluded that for best attachment, the bitumen droplet and air bubble should be in the same size range.

Leja and Bowman (1968) showed that surfactants of different charges have different impact on air-bitumen attachment. In some cases, the presence of surfactant improves the attachment and, in other cases, it hinders the attachment. The presence of surfactant can set up energy barriers to air-bitumen attachment and flotation by increasing electrostatic forces or/and reducing hydrophobic forces.

There are different ideas about the effect of fines on aeration. Some researchers claim that fines reduce the air-bitumen attachment (Gu et al., 2003, Kasongo et al., 2000). They showed that fines attach to either bitumen-water and air-water interfaces and inhibit the attachment.

Gu et al. (2000) reported that fines do not have impact on induction time unless Calcium ions are also present in the solution. They proposed that Calcium ions cause fines to attach to the bitumen surface via surfactants, which inhibits the attachment of bubbles to fine-coated bitumen. Measurements of air bubble attachment to a bitumen surface using an impinging jet technique also showed a reduction in the air bubble-bitumen attachment in the presence of montmorillonite clays and small amounts of added CaSO_4 (14mg/L).

2.7 Effect of conditioning parameters

The densities of bitumen and water are very close. It makes bubble injection a critical step in bitumen extraction. Optimum air flow through air injection nozzles is important. Air flow below an optimum flow rate would not be able to float all bitumen in flotation tank (Flynn et al., 2001). A higher amount of injected air can cause solid entrapment and reduce froth quality (Camp, 1976).

There are many different models that describe bitumen-bubble attachment. Drelich et al. (1995) proposed that bitumen attaches to air bubbles before detaching from sand grains. Gu et al. (2003) and Wang et al. (2003a, b, c) studied systematically effects of temperature, bubble size and water chemistry on bitumen-air bubble attachment. In their study, they proposed that the gas nuclei or tiny bubble can enhance the bitumen-air bubble attachment.

Mechanism of bitumen extraction - bitumen/sands/bubble interactions

Masliyah et al. (2003) proposed the following model for bitumen extraction in hot water process. In this model, a mixture of hot water with process aids and oil sands lumps is exposed to shear force. The shear force, together with heating of oil sands lumps result in ablation of the outer layer bitumen of the lumps. The outer surface ablation gives a chance to fresh surface to be exposed to the hot slurry. The separated smaller parts of the lumps are a mixture of sand grains covered with bitumen. The bitumen on the sand surface later on liberates from sand grains. In first step bitumen

layer thins to form a hole and establish a three phase contact line. This three phase contact line continues to develop until reaching equilibrium between sand, water and bitumen. During this equilibrium stage bitumen forms a droplet on the sand surface. Depending on temperature, the bitumen droplets could attach to or engulf air bubbles and float as the result of the buoyant force.

More studies have been conducted to investigate parameters that are important in bitumen extraction. Drelich et al. (1996) studied bitumen spreading on an air bubble surface in a model system, in which air bubbles are placed on bitumen coated on a glass slide. They found that bitumen was favored to spread at the air bubble surface due to the positive spreading coefficient. Alexander and Li (1996) investigated the effects of bitumen films over air bubble surfaces on bitumen drop-air bubble attachment by measuring the time and temperature dependence of bubble surface tension and contact angle. It was found that a thin bitumen film will weaken the strength of the bitumen droplet-air bubble attachment by 1-10% depending on the size of bitumen droplets and air bubbles. In order to enhance the bitumen drop-air bubble attachment, the size of the bubbles should be the same as the size of the bitumen drops.

Malysa et al. (1999a, b) inserted a "Luba Tube" into a separation cell to sample and record the rise of bitumen-air aggregates. From the recorded images, the size, shape, mass, rising velocity and number of aggregates

could be determined. Ng et al. (2000a, 2000b) and Zhou et al. (2000b) have used this method to observe bitumen flotation from oil sands.

Moran et al. (2000) examined the factors affecting the aeration of small bitumen droplets from both a surface energetic perspective as well as from direct observations. Their study suggests that a positive spreading coefficient does not always guarantee the aeration of bitumen droplets, and bitumen aeration may best be described from a statistical stand point.

Bitumen-bubble attachment in the presence of montmorillonite clays and 1mM calcium (~40ppm) was also studied with impinging jet test (Yang et al, 2000a, b; Masliyah et al., 2003). It was found that only through a combination of montmorillonite clay and calcium decreased significantly the flux of gas bubbles attaching to the bitumen surface. In contrast, the presence of clay and calcium alone or the combination of calcium with kaolinite showed little effect on the gas bubble flux attaching to the bitumen surface. The induction time measurement (Gu et al., 2003) was also used to study the interactions between bitumen and air bubbles. A similar conclusion for bitumen and air bubble attachment in the presence of montmorillonite and calcium was obtained.

An on-line image analysis technique was used (Luthra, 2001; Wallwork, 2003) to evaluate the degree of bitumen liberation from oil sands slurry either in a loop or in a Couette device. A high speed CCD camera was used to monitor the degree of “darkness” of the oil sand-water mixture, which serves as a measure of bitumen liberation. This study made it

possible to gain an insight of the process of bitumen liberation and aeration.

As noted above, interactions between bitumen/silica/bubble were extensively studied by visualization, but there was no direct visualization for bitumen/clays and bitumen/fines interactions. Furthermore, all these research efforts focused on observation of phenomena and did not explore the essence of the observations.

2.8 Bubble dynamics

There have been numerous experimental and numerical studies on bubble dynamics. An early investigation of gas bubbles in an inclined tube was performed by Zukoski (1996). With very large bubbles, he run experiments in Reynolds number range between 100 to 1000 and Bond numbers 1 to 4. In this study, he found that the bubble's rise velocity increased as the inclination angle decreased from the vertical orientation and reached a maximum near a critical angle of about 45° . The critical angle was observed to increase as Bond number decreases. Zukoski (1996) also found that bubbles with a lower surface tension rise faster, and the effect of inclination angle on bubble rising velocity due to change in bubble deformation is complex.

Maxworthy (1991) carried out experiments for smaller bubbles with an effective radius between 0.0625 cm to 0.1425 cm. With $Re \approx 500$, Maxworthy (1991) observed maximum bubble rising velocity near a critical

angle of 50° , which is consistent with Zukoski's (1996) results. All the bubbles in these experiments are in the regime of spherical cap bubbles of low Bond number. They also observed that at small angles of inclination the thickness of liquid films between bubble and the wall decreased.

Masliyah et al. (1994) conducted experiments using system of much lower Reynolds and Bond number. They used very small bubbles with an effective radius of 0.085 cm to 0.145 cm, resulting in a range of Reynolds number from 10 to 575 and Bond number less than 1. In their study, they did not find a critical angle with a maximum bubble rising velocity. In contrast, the bubble velocity increased monotonically as the inclination angle increased toward vertical.

Tsao and Koch (1994) studied the dynamics of small air bubbles in water, with an effective radius of about 0.1 cm rising under an inclined plate. These bubbles have Reynolds number below the spherical cap regime. As a result, the behaviour of bubbles is significantly different from those observed in Maxworthy (1991) and Zukoski's (1996) experiments. Tsao and Koch (1994) found a critical angle of 55° , above this angle bubbles bounce repeatedly and below the critical angle bubble slide steadily along the wall.

2.9 Summary

In this project, gas bubble-flat surface interactions were investigated by determining two dynamic parameters, bubble sliding velocity and induction time of a gas bubble over a flat surface. Systematic bubble sliding and attachment experiments under a wide range of physical and chemical conditions have been conducted and significant amount of experimental data on bubble sliding and attachment process have been gathered as a base for validation and improvement of fundamental bubble attachment models. It was intended to adopt and modify existing developed models, in order to be applicable in oil sands research.

CHAPTER 3: SINGLE MICRO BUBBLE GENERATION¹

3.1 Introduction

The behaviour of a single bubble in a liquid has been studied extensively in the last few decades. Phenomena, such as bubble rise velocity, shrinkage rate due to gas dissolution, bubble-bubble coalescence, bubble-particle interaction, and bubble-solid attachment, are of great importance to fundamental studies and industrial applications. Generation of a bubble of controlled dimension in the range of several to a few hundred micrometers is of a special interest because small bubbles are more resistant to deformation and their spherical shape makes the analysis and modeling of bubble dynamics phenomenon much easier.

Single bubbles with a diameter larger than 1 mm are commonly produced by the release of gas from a submerged orifice (or nozzle) of a small diameter (Blanchard and Syzdek, 1977; Liow, 2000; Khurana and Kumar, 1969; Ramakrishnan et al., 1969; Oguz and Prosperetti, 1993). Smaller bubbles, however, cannot be generated easily due to limited buoyancy force, which is needed to assist bubble detachment from the orifice (Blanchard and Syzdek, 1977; Oguz and Prosperetti, 1993). Bubbles leave an orifice when the buoyancy force exceeds the surface tension force that holds the bubble to the orifice. As a result, small bubbles can

¹ A version of this chapter has been published. Seyyed Najafi A., Xu Z., and Masliyah J., 2008, Single micro bubble generation by pressure pulse technique, *Journal of Chemical Engineering Science*, 63 (7), 1779-1787.

only be generated if the surface tension of the liquid is sufficiently low. For aqueous solutions, the surface tension can be reduced by the addition of surface-active agents, but this limits the systems of interest to be studied. An alternative approach is to introduce additional external force to facilitate gas bubble detachment from the orifice/ micropipette.

Lack of gas pressure control at the tip of nozzles causes production of a chain of bubbles instead of the release of individual bubbles at well defined intervals, which would be desired for the study of single bubble behaviour.

A refined model for the production of bubbles from orifices and a discussion on the difficulties in generation of small bubbles were reported by Oguz and Prosperetti (1993). According to these authors, the difficulty in producing small bubbles is related to the build-up of overpressure at the very initial stage of the bubble formation process, in which the quasi-equilibrium of the pressure at the gas-liquid interface is not achieved. To overcome this difficulty, they suggested reducing the bubble pressure soon after the bubble starts to grow. Using this approach, they were able to produce bubbles of smaller diameter, but remained larger than 1 mm.

Kameda and Shirota (2001) succeeded in producing smaller size bubbles in viscous oil medium as higher viscosity helped to better control the pressure at the tip of nozzle and improved mechanical stability of the interface. However, their technique was not suitable for producing small bubbles in aqueous systems.

Blanchard and Syzdek (1977) succeeded in generating small single bubbles, but their method required trial and error to find the appropriate geometry for a given test. A reliable method for systematically producing small single bubbles of various gases directly from a gas cylinder in an aqueous system remains to be developed.

In this study, an elegant, yet simple and reliable technique was developed for the generation of bubbles with controlled diameters smaller than 1 mm, using a pressure pulse technique together with a micropipette.

3.2 Concept for generation of single micro-bubbles

A schematic diagram of the pressure pulse apparatus constructed for generation of single sub-millimetre size bubbles is shown in Figure 3.1. The experimental apparatus consists of: a) gas cylinder, b) gas regulator, c) micro needle valve for precise control of the gas flow rate, d) gillamount capillary syringe for adjusting the pressure inside the tubing, e) on-off electrical relay switch for generating pressure pulses, f) Validyne pressure transducer for measuring the pressure inside the tubing, g) glass chamber with the liquid in which bubbles are produced, and h) Motion scope CCD camera for videotaping the process of bubble generation and measurements of bubble sizes.

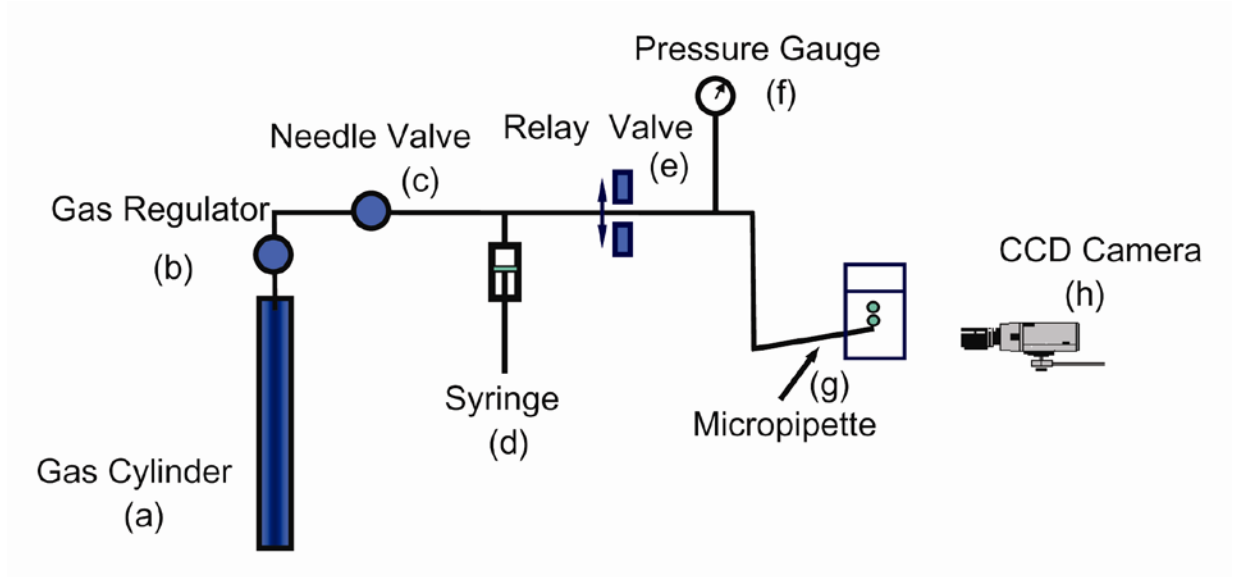


Figure 3.1 A schematic diagram of the experimental set-up for single micro-bubble generation.

To have a fine control on the gas flow rate, a micropipette of very small flow diameter (1-20 μm) was used as the flow line (Moran et al., 1999). Pressure pulses were controlled by a relay valve and used to create a pressure front. The instantaneous pressure front was created to disturb the gas-liquid interface, thereby promoting the formation of smaller bubbles. The size of gas bubbles was controlled by the applied gas pressure and the size of the installed micropipette.

For a non-flow system the pressure inside the bubble (P_B) is a sum of two independent pressures, the hydrostatic (P_h) and the capillary (P_c) pressures, as described in Figure 3.2:

$$P_B = P_h + P_c \quad (3-1)$$

Hydrostatic pressure is due to the atmospheric pressure (P_o) and the liquid head (h) above the micropipette:

$$P_h = P_o + \rho_L g h \quad (3-2)$$

where ρ_L is the density of liquid and g , acceleration due to gravity.

The capillary pressure, the pressure difference between inside and outside of the bubble on the other hand is given by the Young-Laplace equation below:

$$P_c = \frac{2\gamma}{R} \quad (3-3)$$

where γ is the surface tension of the liquid and R is the radius of the bubble.

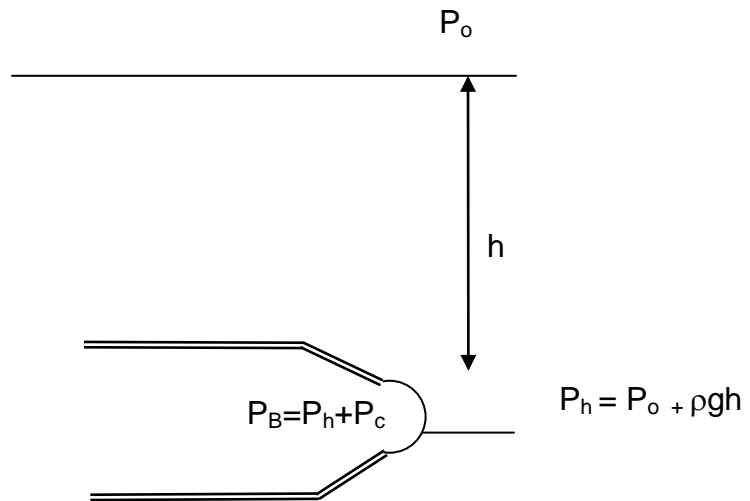


Figure 3.2 A schematic view of the pressure distribution on a micropipette tip for a non-flow system.

With the flowing gas inside the micropipette, the created bubble surface bulges out thereby continuously decreasing the radius of the bubble. As the bubble grows, the capillary pressure increases with decreasing bubble radius. As a result the pressure inside the bubble progressively increases. During this process the pressure rises to a maximum value, where the radius of the bubble equals the radius of the micropipette tip. At the maximum pressure, the bubble forms a half sphere and it is at its smallest radius of $R = r_0$ as shown in Figure 3.3 After passing this point of the maximum pressure (minimum radius), the pressure decreases spontaneously as the bubble experiences a sudden growth and breaks away from the micropipette. Subsequently, a new bubble can form at the micropipette tip. This critical maximum pressure is given as the maximum bubble pressure (P_{bubble}), (Hallowell and Hirt, 1994; Kovalchuk et al., 1998; Schnorf et al., 1994).

For single micro bubble generation, the pressure inside the micropipette is kept slightly less than (P_{bubble}) by closing the inlet valve and adjusting the pressure with the syringe. Generation and release of bubbles from the micropipette are accomplished by pressure pulses generated by the electrical relay switch. This switch introduces pressure pulses of duration in the range of about 50 ms by squeezing flexible tubing that is sandwiched between the relay switch.

The pressure pulse leads to an instantaneous increase in pressure by squeezing gas toward the gas-liquid interface. A sudden growth of the

bubble occurs when the pressure front reaches the interface. However as the bubble volume increases it causes an increase in the system volume (bubble + micropipette) and the pressure reaches the maximum bubble pressure (P_{bubble}), after which the pressure in the system decreases. As a result of the system pressure decrease with bubble growth, the bubble breaks at its neck, resulting in the generation of single bubbles of desired size in the micron range.

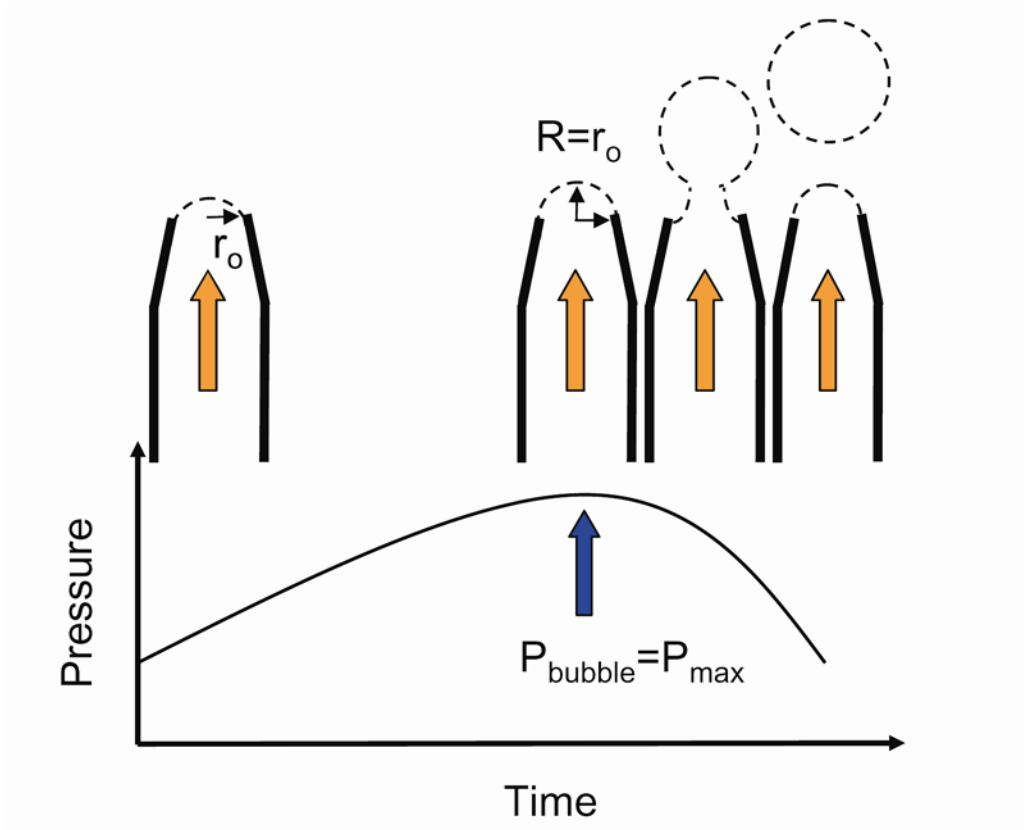


Figure 3.3 Bubble generation process and pressure variation with time.

3.3 Experimental procedure

The apparatus was used to generate air, carbon dioxide and nitrogen bubbles in ultra pure water with a resistivity of 18.2 M Ω cm produced by Millipore system (Elix 5 Millipore UV). This is the most difficult aqueous system to generate single bubbles of micron size. Micropipettes were made from glass capillary tubes (Kimble Glass Inc) with 1 mm OD and 0.7 mm ID. Vertical micropipette puller (David Kopf Instruments, Tujunga CA, model 730) was used to pull a capillary tube to obtain the desired diameter and length of the micropipette. A forging device was used to cut the micropipette, thereby producing an open and smooth tip. A precision microscope (divert Axiovert 200) was used to measure the inner diameter of the produced micropipette.

All experiments were video recorded with a high-speed digital imaging system (Motion Scope R 8000S, Red Lake Imaging, USA) at a selected capture speed of 500 frames per second (fps). The bubble travel time and velocity were measured by tracing the bubble motion for a series of consecutive frames. Dimensions of the field of view were calibrated using a scale of known length. The field of view for the experiments was set to 2.5 mm.

For bubble generation, the whole system, including the tubing, syringes and the micropipette is filled with the desired gas. The gas injection continued until the pressure in the micropipette tip has just reached P_{bubble} ,

at which the bubble formed a semi-spherical cap at the micropipette tip. The relay switch is activated, thereby cutting off the continuous gas supply while producing a pressure front, which would lead to the separation of the gas bubble from the micropipette tip. The diameter of the released bubble is much larger than the micropipette tip diameter. Nevertheless, due to the expansion of gas in the micropipette under the reduced capillary pressure, the bubble volume is well controlled and is related to the micropipette volume, tip size, pulse strength, and inclination angle of micropipette axis. Although the frequency of single bubble generation is controlled by the duration of relay switch in its closed position, the inclination angle of micropipette axis is found to be an important parameter on controlling the size of generated bubbles. A theoretical consideration for bubble generation from an inclined micropipette is considered below (p.31).

3.3.1 Bubble pressure

In order to generate single bubbles, operating pressure should be determined for each individual micropipette. The operating pressure was determined by measuring the maximum bubble pressure (P_{bubble}) for micropipettes with different tip sizes. Figure 3.10 illustrates the measured maximum bubble pressure for micropipettes of different tip sizes.

The measured maximum pressures were compared with the theoretical predictions from the Laplace equation. As shown in Figure 3.10, the

experimentally measured pressures are in good agreement with the theoretical predictions.

3.3.2 Reproducibility

To test the reliability and reproducibility of the proposal technique, about twenty bubbles were produced and measured for each individual micropipette, while all other conditions were kept the same. Figure 3.11 shows the frequency of the produced bubbles in a given size from a micropipette with a tip diameter of 7 μm , a taper length of 27 mm and an inclination angle of 150°. It is evident that bubbles of a very narrow size range can be produced.

3.4 Theoretical model for bubble generation from an inclined pipette

For a spherical bubble, the bubble growth is described by the Rayleigh-Plesset equation (Oguz and Prosperetti, 1993):

$$R\ddot{R} + \frac{3}{2}(\dot{R})^2 = \frac{1}{\rho_L} [P_B - \frac{2\gamma}{R} - P_h] \quad (3-4),$$

where the dots stand for time derivative, R is the bubble radius at time t , ρ_L is the density of the liquid and P_B is the internal pressure of the bubble.

During bubble growth, three major forces balance each other and determine the size of the detached bubbles (Oguz and Prosperetti, 1993). Among these forces, the buoyancy force assists bubble detachment, while the capillary and hydrodynamic forces resist bubble detachment. The

hydrodynamic force reduces to the added mass force, where the drag force is neglected. For the case where the density of the liquid is much larger than the density of the gas ($\rho_L \gg \rho_G$), we can neglect the bubble mass and write:

$$\frac{d}{dt} \left(\frac{1}{2} \rho_L V_b \frac{dz}{dt} \right) + 2\pi\gamma r_o = \rho_L V_b g \quad (3-5)$$

where z is defined as the position of the bubble center with respect to the tip of the micropipette and r_o is the radius of the micropipette tip. The added mass force (first term in equation (3-5)) (Lighthill, 1986) is directly proportional to the bubble volume (V_b), and in general it is much larger than the mass of the bubble. It is for this reason that the mass of the bubble has been neglected in the above force balance.

According to equation (3-5), the added mass and the surface tension force oppose the buoyancy force. To solve equations (3-4) and (3-5), a detachment condition has to be defined. We assume that a bubble detaches from the micropipette tip, when the bubble center travels a distance equal to the bubble radius plus the tip radius, as illustrated in Figure 3.4. This can be described mathematically as a detachment criterion:

$$z = R + r_o \quad (3-6)$$

In a typical bubble generation process, the bubble will remain attached to the micropipette tip and will continuously increase in size until the

buoyancy force exceeds the surface tension and the added mass force. Low values of the resistance force, i.e., the added mass and surface tension would subsequently lead to a smaller size of bubbles.

In our tests, we found that the size of the detached bubble can be altered by changing the inclination angle of the micropipette. This is illustrated in Figures 3.5 and 3.6. Changing the orientation of the micropipette affects the force balance on the micropipette tip and causes a change of bubble's position with respect to the micropipette. When the micropipette is in an upward vertical position, there is a perfect symmetry for the bubble and micropipette. However, a variation in the inclination causes an asymmetry of the bubble with respect to the micropipette, with the top apex of the hemisphere bubble inclined with respect to the micropipette. New angle positions between the bubble neck and the micropipette tube shown in Figure 3.6 are caused by the micropipette inclination. They are termed as front angle θ_F and back angle θ_B , respectively, as shown in Figure 3.7.

We will discuss the effect of inclination on the applied forces. As shown in Figure 3.7, for the upward vertical micropipette, there is a perfect symmetry between the bubble and micropipette, i.e. $\theta_F = \theta_B$. In this case, the buoyancy force is vertically upward while the surface tension force is vertically downward. The total surface tension force is a resistant force against bubble detachment. The resultant of the surface tension and the buoyancy force determines whether a bubble would detach.

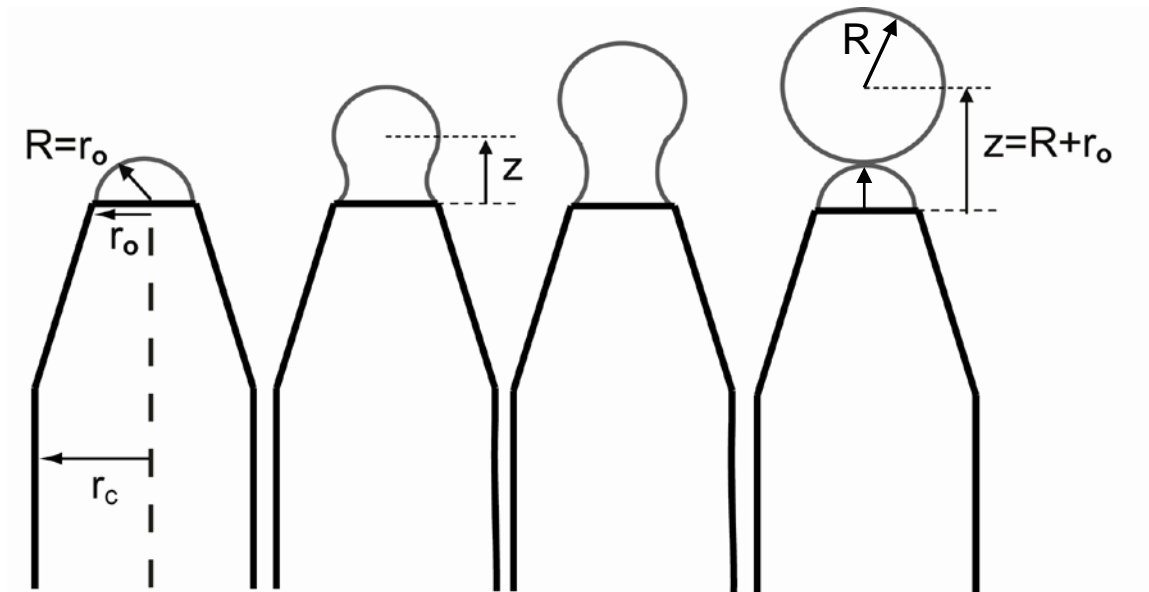


Figure 3.4 Bubble detachment criterion: bubble will detach from a micropipette tip when its center travels a distance equal to the bubble radius R plus the micropipette radius, r_o .

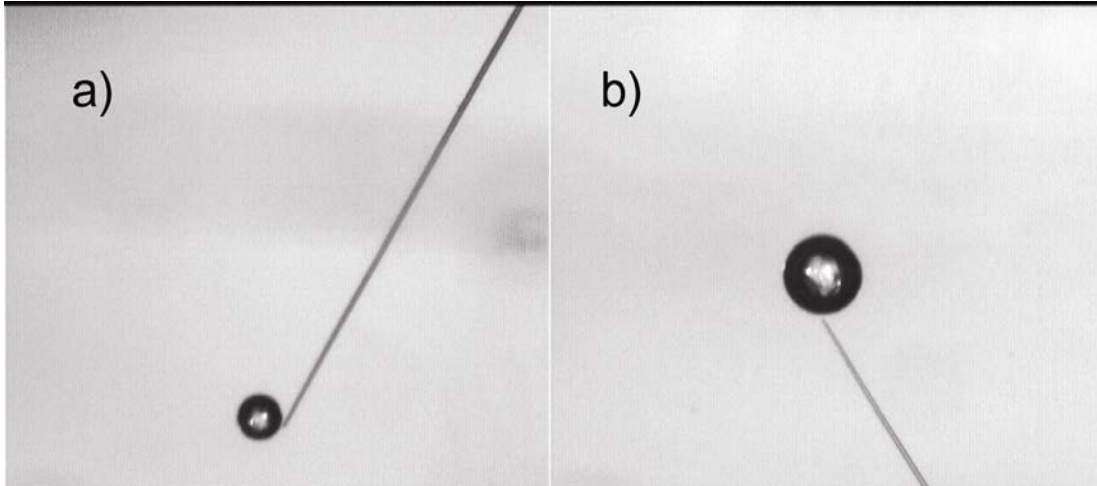


Figure 3.5 Separation of a bubble from micropipette tip with different inclination angle: a) downward inclination and b) upward inclination.

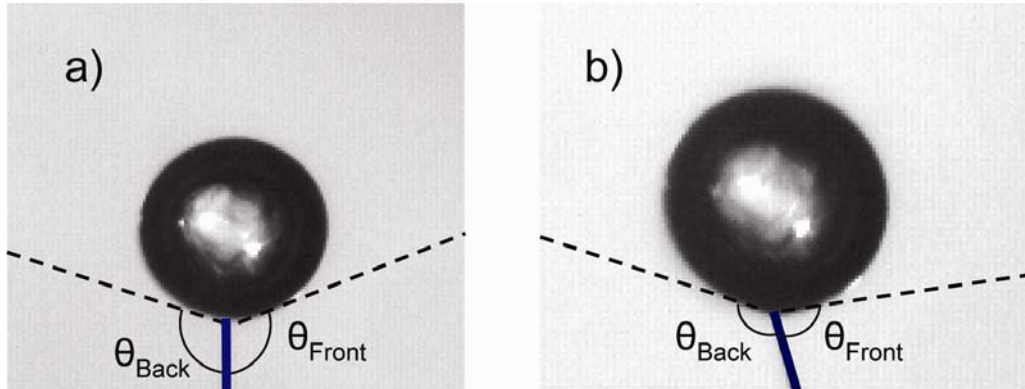


Figure 3.6 Effect of micropipette inclination angle on the back and front angles: a) $\theta_{\text{Back}} \approx \theta_{\text{Front}}$ and b) $\theta_{\text{Back}} > \theta_{\text{Front}}$.

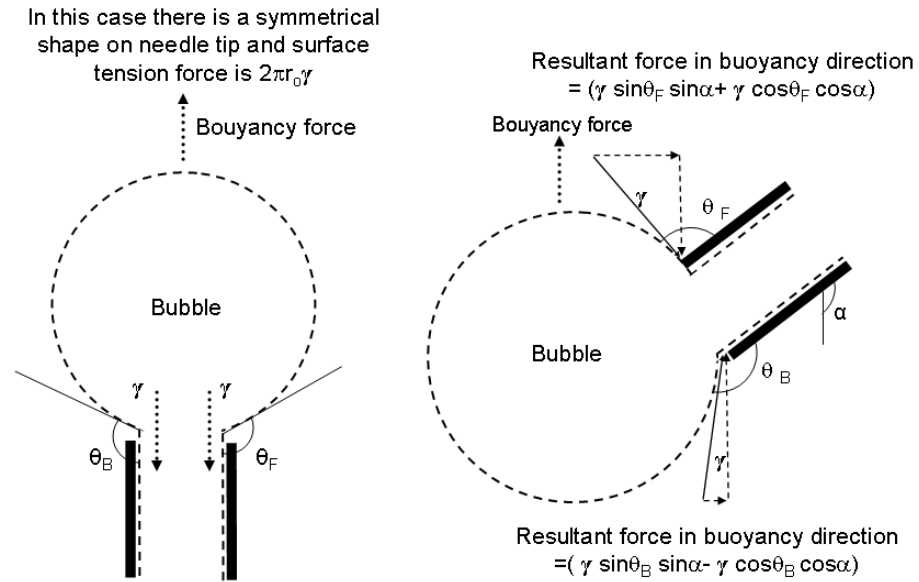


Figure 3.7 Illustration of free body diagram of buoyancy and surface tension forces acting on the tip of the micropipette.

When the micropipette position is changed from vertical to any other angle, as shown in Figures 3.5 to 3.7, the back and front neck angles are different and the bubble attains an asymmetrical shape. The attachment angle is assumed to have two different values, one for the lower part of the attached bubble and the other for the upper part, which are referred to as angles θ_F and θ_B , respectively. In this case, each surface tension force has components in vertical and horizontal directions. The direction and value of these component forces depend on the micropipette inclination. The resultant of these forces would either assist or resist the buoyancy force, depending on the inclination of the micropipette. With micropipette inclination, the vertical component of the resistant force for detachment is reduced and consequently, one would expect the generation of smaller bubbles with all other parameters being the same.

The inclination of the micropipette has also an effect on the added mass force. According to the definition of the added mass force, this force operates in the direction of bubble movement. In the vertical upward configuration of bubble generation, the added mass force is vertically downward and in the opposite direction to the buoyancy force.

In the case of inclined micropipette, the bubble will move upward while it is in the growth stage. Such movement complicates the calculation of the added mass force. As an approximation, the added mass force is only evaluated along the micropipette axis and its vertical component was used in the force balance equation. As the micropipette inclination angle α ,

increases from 0 to $\pi/2$, the vertical components of the added mass force decreases and it acts in the downward direction. For inclination angle, α , between $\pi/2$ to π , the added mass force increases, but it acts in the upward direction. As shown in the Appendix B, the added mass (I) for an inclined micropipette, can be written as:

$$I = \frac{1}{2} \rho_L V_b (\cos \alpha) \quad (3-7)$$

The force balance on the micropipette tip as given by equation (3-5) is modified to:

$$\frac{d}{dt} \left(\frac{1}{2} \rho_L V_b (\cos \alpha) \frac{dz}{dt} \right) + \gamma r_o \pi [-(\sin \theta_F \sin \alpha + \cos \theta_F \cos \alpha) + (\sin \theta_B \sin \alpha + \cos \theta_B \cos \alpha)] = \rho_L V_b g \quad (3-8)$$

With approximation of $V_b = Qt$, where Q is the gas flow rate (Oguz and Prosperetti, 1993), and solving equation (3-8), we have:

$$z = \frac{1}{2(\cos \alpha)} g t^2 - \frac{\gamma r_o t \pi [(\sin \theta_F \sin \alpha - \cos \theta_F \cos \alpha) + (\sin \theta_B \sin \alpha + \cos \theta_B \cos \alpha)]}{\rho_L Q (\cos \alpha)} \quad (3-9)$$

Equation (3-9) shows that at $t=0$, $z=0$, in the case of $\alpha=0$, i.e., at upward vertical position, equation (3-9) reduces to $z = \frac{1}{2} g t^2$, which was used by Oguz and Prosperetti (1993). In the above equation, Q is the gas flow rate in the conically tapered micropipette (Bird et al., 1987) and is given by:

$$Q = \frac{\pi (P_{\text{bubble}} - P_B) r_c^4}{8 \mu_G L} \left[1 - \frac{1 + (r_o/r_c) + (r_o/r_c)^2 - 3(r_o/r_c)^3}{1 + (r_o/r_c) + (r_o/r_c)^2} \right] \quad (3-10)$$

where μ_G is the gas viscosity, L is the taper length. To calculate z using equation (3-9), the values of the front and back angles for different inclinations of the micropipette are required. For this purpose, the back and the front angles between the bubble neck and the micropipette tip at different inclinations at the detachment stage are shown in Figure 6. In this set of measurements, the inclination angle of the micropipette changed while the micropipette tip was kept at the same liquid depth. The bubbles were generated under the same conditions and the bubble generation process was recorded. The recorded video was analyzed to determine the back and front angles with respect to the micropipette inclination by identifying tangents of these angles with an accuracy of ± 5 degree. The experimental results are shown in Figure 3.8. By curve fitting, the following two empirical equations relating the front and back angles to the inclination angle were obtained:

$$\theta_F = 0.0028\alpha^2 - 0.84\alpha + 90 \quad (3-11)$$

$$\theta_B = -0.0019\alpha^2 + 0.6\alpha + 90 \quad (3-12)$$

For $0 \leq \alpha \leq 180$, equations (3-4), (3-9) - (3-12) were then solved simultaneously. For a given time, two different curves were obtained (Figure 3.9), one representing the rate of bubble growth (equation 3-4) and the other, the position of bubble center, equation (3-9). The intersection point of these two curves determines the size of a detached bubble.

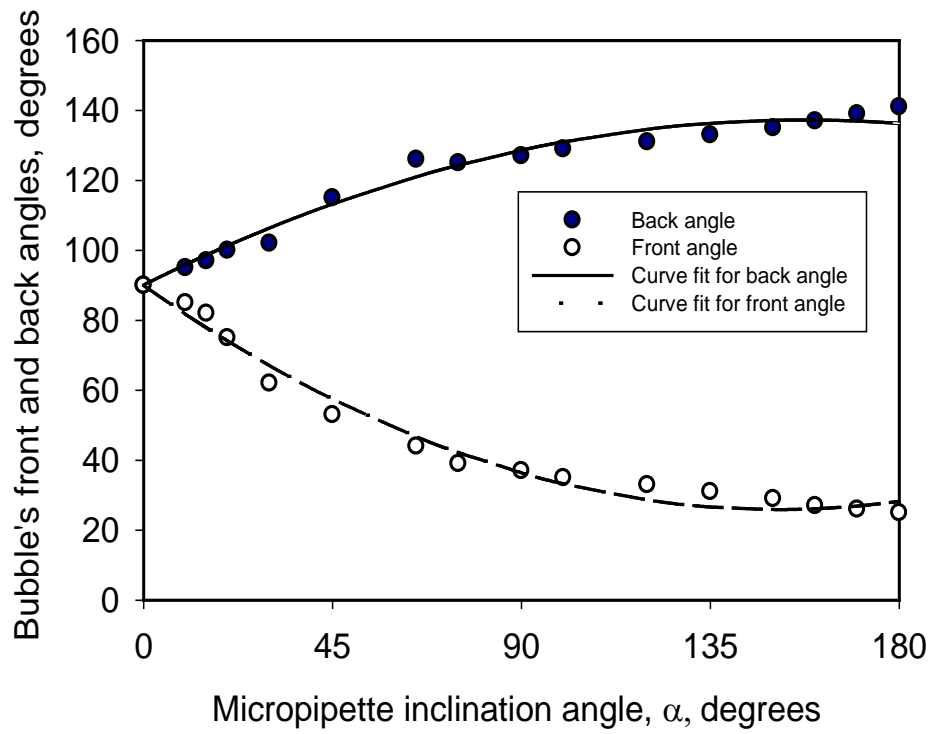


Figure 3.8 Experimental measurements and curve fit results of bubble front and back angles with respect to the inclination angle of micropipette.

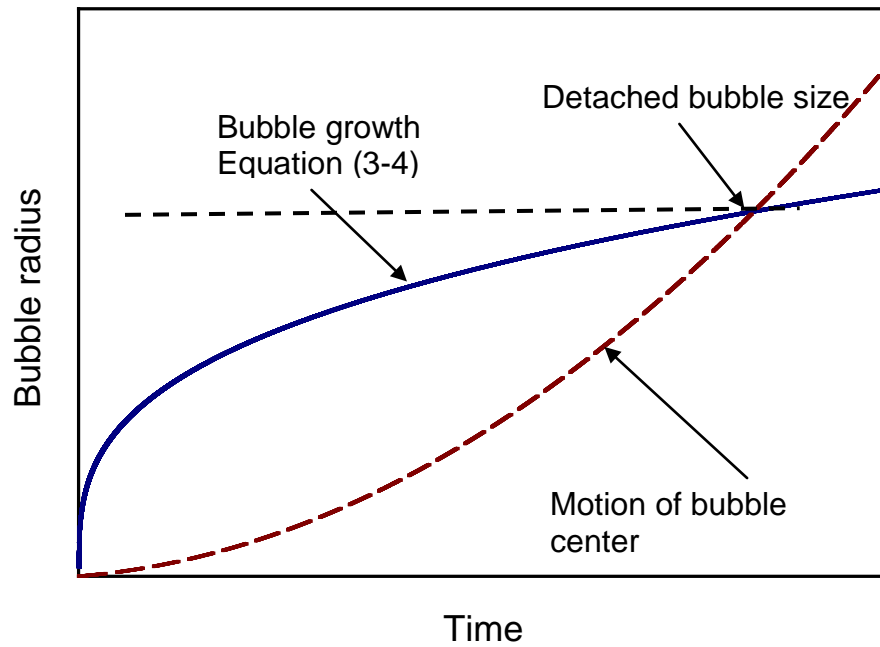


Figure 3.9 Illustration of solution for bubble growth and motion of bubble center. The intersection point gives the bubble radius at detachment.

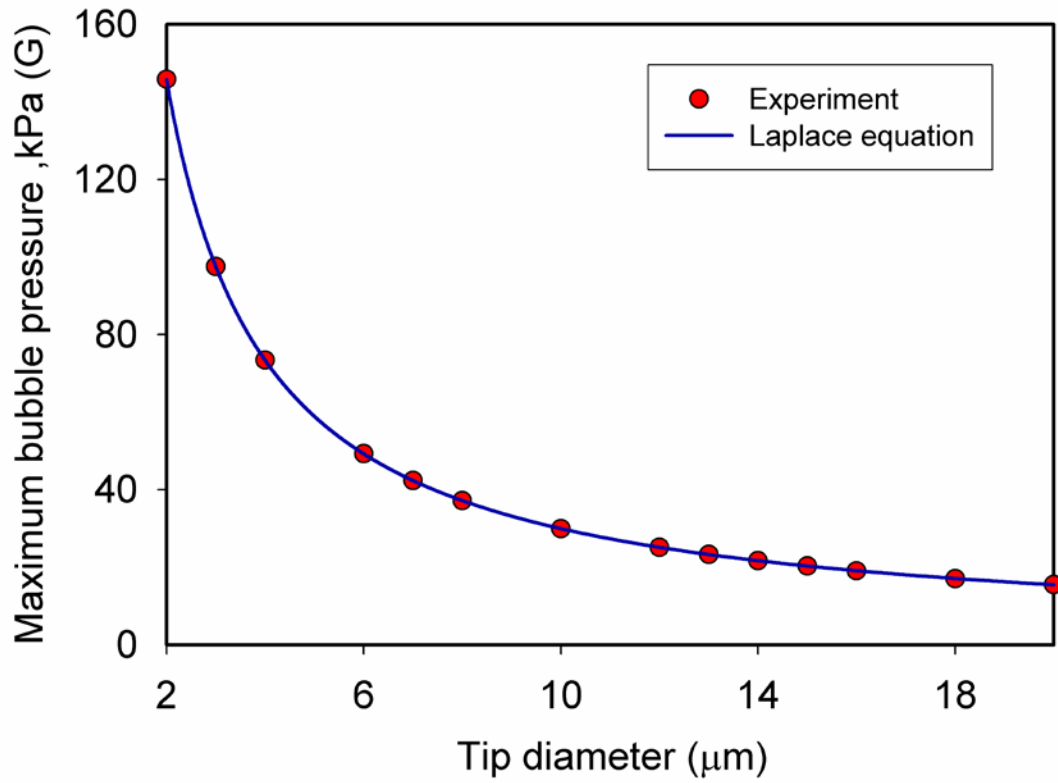


Figure 3.10 Maximum bubble pressure (P_{bubble}) as a function of tip diameter.

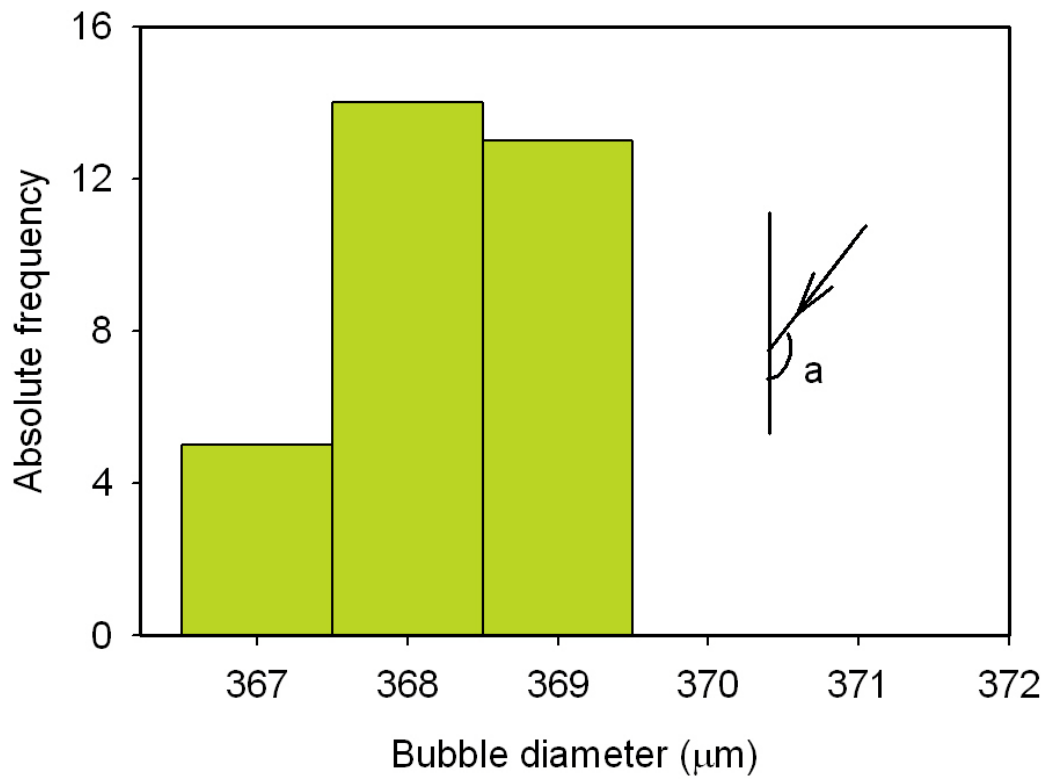


Figure 3.11 Absolute frequency and histogram of produced bubbles in a given size (micropipette I.D. =7 μm, inclination angle = 150°, taper length = 17mm).

3.5 Results and discussion

3.5.1 Effect of gas type

According to Martanto et al. (2005), the gas viscosity in conically tapered micropipettes is an important factor in gas flow. For gases of different viscosities a given driving force would cause movement of a different amount of gas toward the bubble. For example, a lower viscosity gas will give rise to a lower pressure drop in the micropipette, and consequently a higher gas mass flow rate moving toward the micropipette tip. A higher mass flow rate will cause the delivery of more gas to a bubble and would lead to bubbles of larger size.

In this study air, N₂ and CO₂ were used as the injection gas. The physical properties of these gases are given in Table 3.1. Experimental measured bubble sizes are compared to the model predictions as shown in Figure 3.12. As it was predicted, gases with higher density and lower viscosity produce larger bubbles compare to gases with lower density and higher viscosity.

Table 3.1 Viscosity and density of gases used in this study.

Gas	Viscosity (*10 ⁻⁵ Pa.s, T = 23° C)	Density (kg/m ³) (P = 101 kPa, T = 23° C)
Air	1.85	1.18
N ₂	1.76	1.25
CO ₂	1.49	1.98

3.5.2 Effect of taper length

One of the important factors that affects bubble size is the micropipette taper length. According to Martanto et al. (2005), the taper length is in direct relation with the flow resistance. Smaller bubbles can be produced with longer taper lengths. To illustrate this effect, micropipette of three different taper lengths of 9 mm, 17 mm, 27 mm, with an error of 0.2 mm, were used to generate bubbles, and the results are shown in Figure 3.13.

Figure 3.13 shows that with other experimental conditions hold the same, a longer taper length produces smaller size bubbles. It is interesting to note the excellent fit between the bubble size produced experimentally and that predicted. It should be noted that it is difficult to conduct experiments with very long taper length micropipettes as they become fragile.

3.5.3 Effect of tip diameter on bubble size

The micropipette tip diameter plays an important role in bubble generation. In order to show this effect, bubbles were generated with micropipettes of different tip sizes. As shown in Figure 3.14 the bubble diameter varies with the tip diameter. As anticipated, smaller bubbles are generated using the micropipette of smaller tip sizes. The size of bubbles generated compares, to some degree, well with that predicted from the model developed in this study.

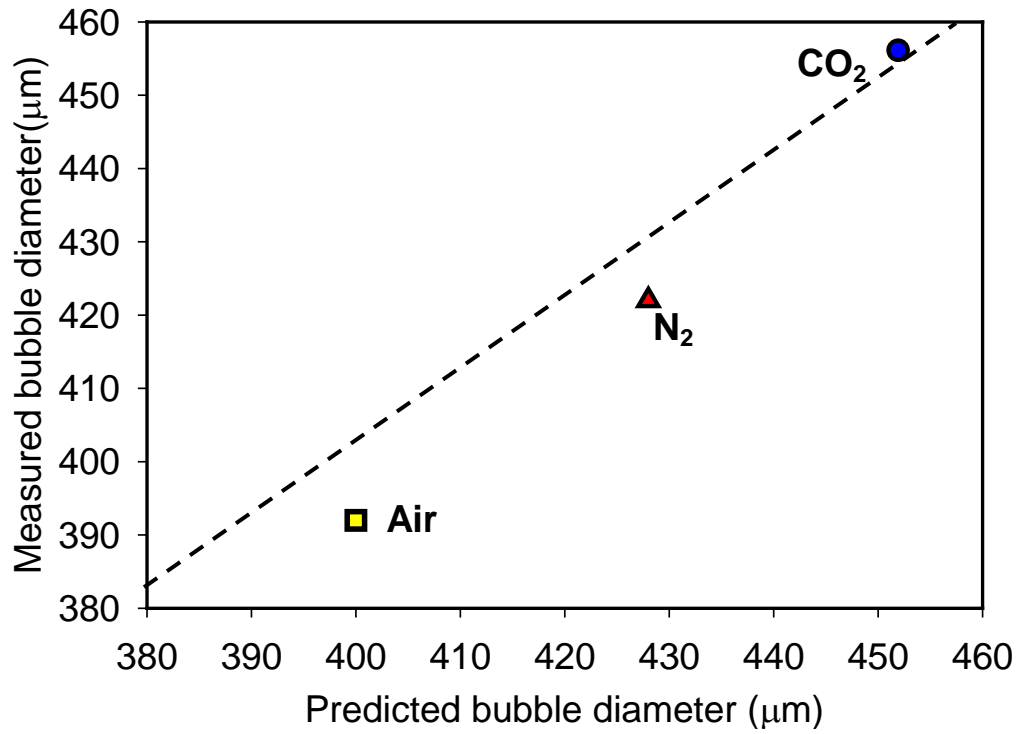


Figure 3.12 Effect of gas type on the produced bubble size (micropipette I.D. = 13 μm, inclination angle = 150°, taper length = 17 mm).

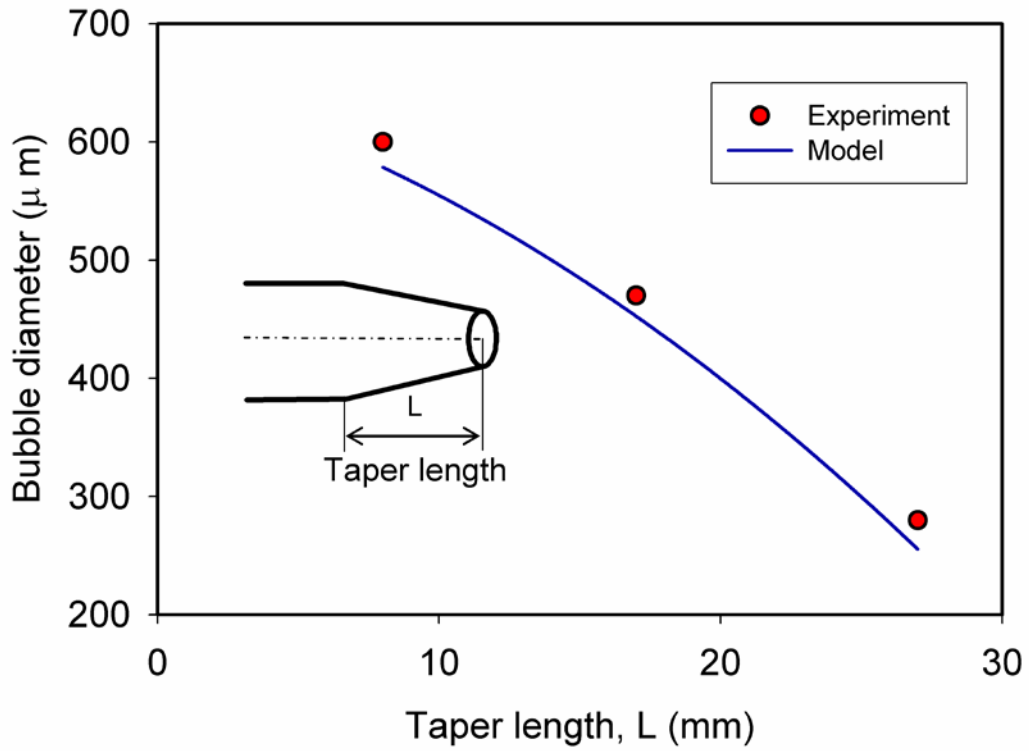


Figure 3.13 Effect of taper length on the size of air bubbles (micropipette I.D. = 5 μm, inclination angle = 150°).

3.5.4 Effect of micropipette inclination on bubble size

As mentioned in the theory section, one of the factors in controlling bubble generation is the micropipette inclination angle. In order to study this effect, the micropipette tip was held at the same depth in the water while the micropipette inclination axis was rotated from 0° to 180° . Bubble size was measured for each inclination angle and the results are shown in Figure 3.15.

At the inclination less than 60° , larger bubbles of $800\ \mu\text{m}$ are generated, with little dependence on the inclination angle. A sharp decrease in bubble size was observed with further increasing the inclination angle to 145° at which the bubble size reduced to $380\ \mu\text{m}$. A further increase in inclination above 150° showed no impact on the bubble size. At such large angles, the bubble stays on the micropipette and reaches a minimum front angle. Under such conditions the presence of the micropipettes physically hinders the release of the bubble, a situation not considered in the model. As a result, a constant bubble size in this interval of inclination (150° - 180°) was observed.

3.6 Conclusions

Single microbubble generation by the pressure pulse technique is demonstrated in this study. Reproducible bubbles of controlled sizes were obtained for a given micropipette geometry and gas type. The bubble size was much dependent on the micropipette tip size, taper length, inclination

angle and gas type. The bubble size predicted from the developed theoretical model was in fair agreement with the experimental results. The model allows us to select operating conditions for generating single bubbles of a desired size for a given micropipette geometry by changing inclination angles.

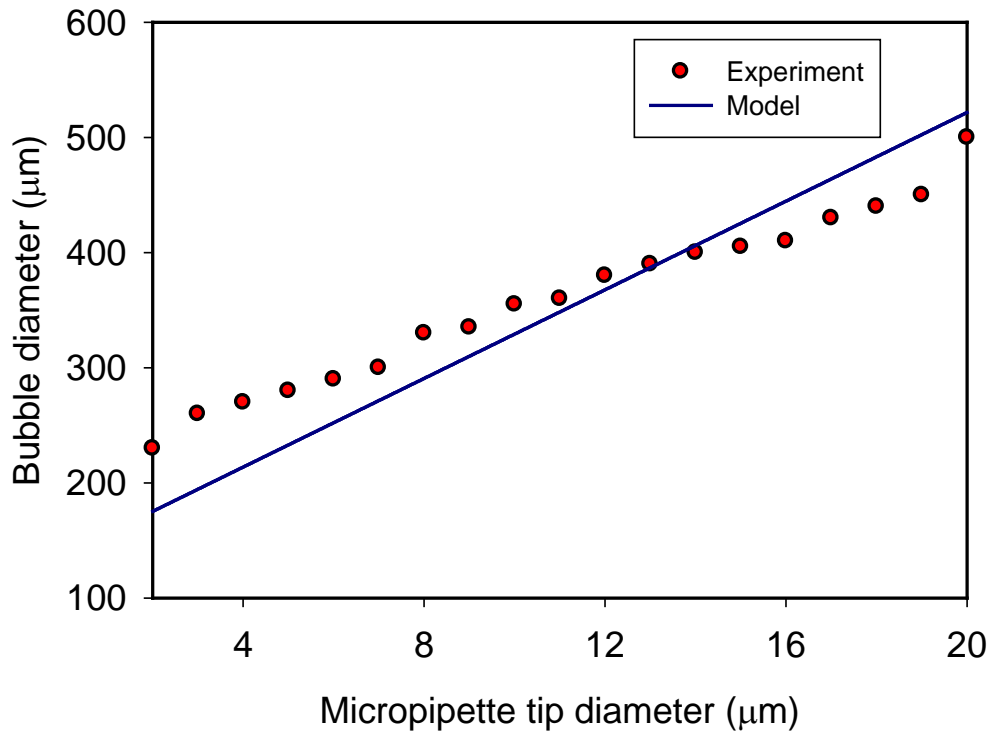


Figure 3.14 Effect of tip diameter on the diameter of generated air bubbles (micropipette inclination angle = 150° , taper length = 27 mm).

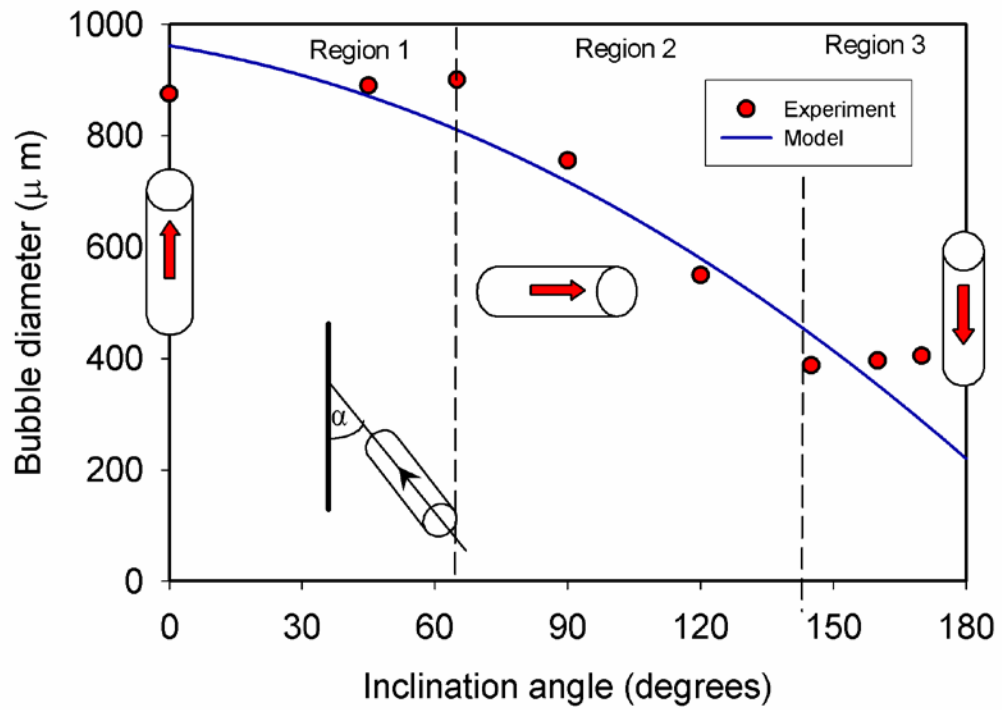


Figure 3.15 Effect of inclination angle on the diameter of generated bubbles (micropipette I.D. = 13 μm , taper length = 17 mm).

Chapter 4: Bubble Sliding Velocity and Induction Time²

4.1 Introduction

Bubble-solid interactions play a major role in oil sands extraction, mineral processing, chemical and environmental industries (Dai et al., 1988). For example, in the Canadian oil sands industry, flotation is a major process used to recover bitumen from a slurry. Since bitumen density is close to that of water, air bubble-bitumen attachment is essential for effective gravity separation of the aerated bitumen.

Improving air-bitumen attachment is an important step in obtaining higher efficiency in flotation (Dai et al., 1988, 1999). Flotation efficiency depends on bubble-particle collision and subsequent attachment efficiencies. Flotation efficiency is also strongly dependent on bubble size, bitumen or particle size, surface and physiochemical properties, process temperature and hydrodynamic conditions of flotation systems.

Bubble-particle collision is well studied and models proposed by Dai et al. (2000) and Ralston et al. (2002) are well established. Attachment efficiency, however, is a function of “induction time” largely dependent on interactions between bubble and solid surfaces, which is much complex to analyze (Dobby and Finch, 1986, 1987; Ralston et al., 1999; Yoon et al., 1989).

² A version of this chapter has been published. Seyyed Najafi A., Xu Z., and Masliyah J., 2008, Measurement of sliding velocity of a single micro bubble under an inclined collector surface, *Canadian Journal of Chemical Engineering*, 86 (6), 1001-1010.

There are four diverse definitions of induction time in the literature: 1) the time required for the intervening liquid film thinning to its critical thickness (Schulze and Birzer, 1987; Schulze, 1992); 2) the time required for the film depletion up to gas nucleation and formation of three phase contact line (tpcl) (Paulsen et al., 1996); 3) the time required for the film depletion to a minimum rim diameter (the rim diameter required to have stable attachment) (Peng, 1996; Gu et al., 2003); and 4) the time required for all three steps of film thinning, rupture and development of stable attachment (Gu et al., 2003, 2004). In this study, the last definition of induction time is used.

In the present study, I investigated several physical and chemical conditions to understand their impact on the sliding velocity and induction time of a micro-bubble sliding underneath an inclined solid surface.

4.2 Experimental procedure

In order to avoid bubble deformation and thereby the complexity in interpreting the data, experiments in this study were carried out using bubbles smaller than 0.4 mm. This is confirmed by calculating the Weber number, We , using Equation (4-1) below:

$$We = \frac{2\rho V^2 R_b}{\gamma} \quad (4-1)$$

where ρ is the liquid density, V - bubble rise velocity, R_b - bubble radius and γ surface tension of liquid. Based on the maximum terminal velocity

of the bubbles used in our study, We number was calculated to be in the range of 1.4×10^{-3} to 1.1×10^{-2} , indicating that the generated bubbles maintained fairly spherical shape during the rising and sliding (Masliyah et al. 1994).

Generation of micro bubbles of a given size is a challenging task. Two different methods were used to generate single micro bubbles: electrolysis for generation of H₂ and O₂ bubbles (Gu et al., 2004) and a pressure pulse technique for generation of CO₂, air and N₂ bubbles (Najafi et al., 2008). The electrolysis apparatus by Gu et al. (2004) was adopted to generate small H₂ or O₂ bubbles. In this apparatus, the smaller bubbles generated by electrolysis were collected and coalesced in a bubble collection chamber. Once the bubble reached a desired size, it was expelled out from the chamber and rose in the liquid medium toward the collector surface.

The pressure pulse technique was developed recently in our laboratories (Najafi et al., 2008). In this method, gas was injected through a submerged micropipette. The apparatus included a gas cylinder, precision needle valve and a pressure pulse generator as was schematically shown in Figure 3.1. Upon application of a pressure pulse, a single micro-sized bubble was released from the micropipette tip. This technique of bubble generation is reliable and reproducible. Bubbles of a very narrow size range can be produced using this method (Najafi et al., 2008). The distance between the micropipette tip and the collector surface was set

sufficiently large (3 mm) to allow the bubble to reach its terminal velocity prior to colliding with the inclined collector surface. Upon release, the bubble traveled through the temperature-controlled test liquid to contact the collector. The inclination angle is measured relative to the horizontal axis as indicated in Figure 4.1.

Experiments were conducted in a temperature-controlled chamber. All the experiments were video recorded with a high-speed digital imaging system (Motion Scope R 8000S, Red Lake Imaging, USA) at a capture speed of 500 frames per second (fps). The bubble travel time and velocity were measured by tracing the bubble motion for a series of consecutive frames. Dimensions of the view field were calibrated using a scale of known length and set to 2.5 x 2.5 mm.

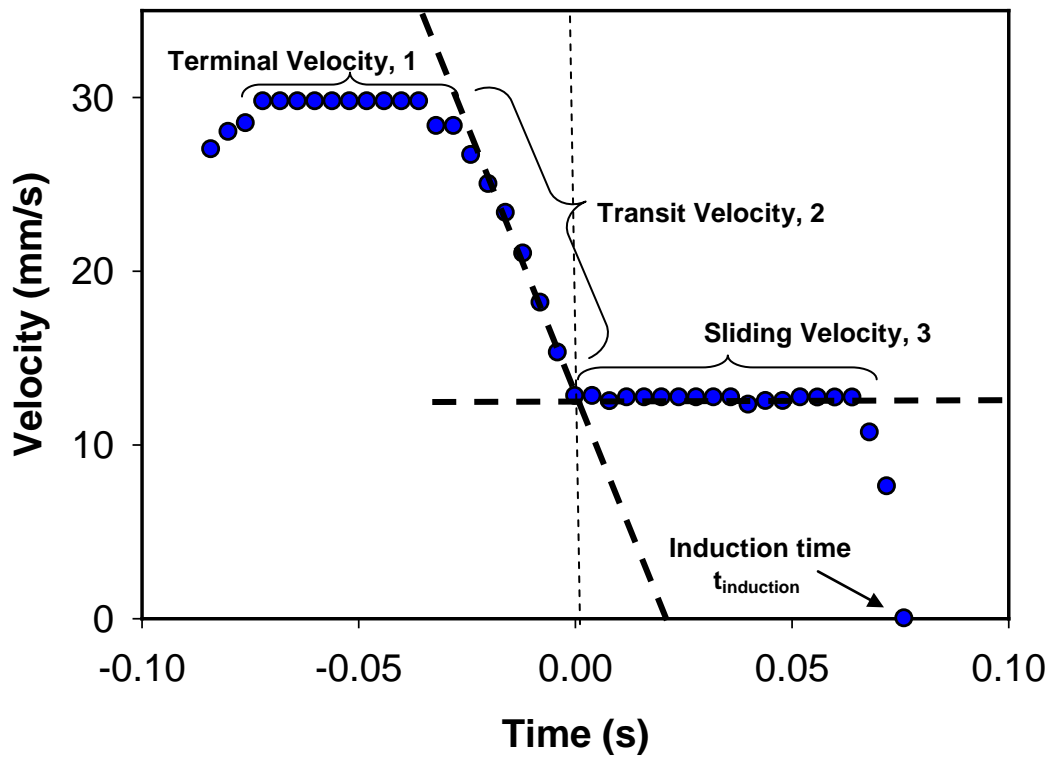
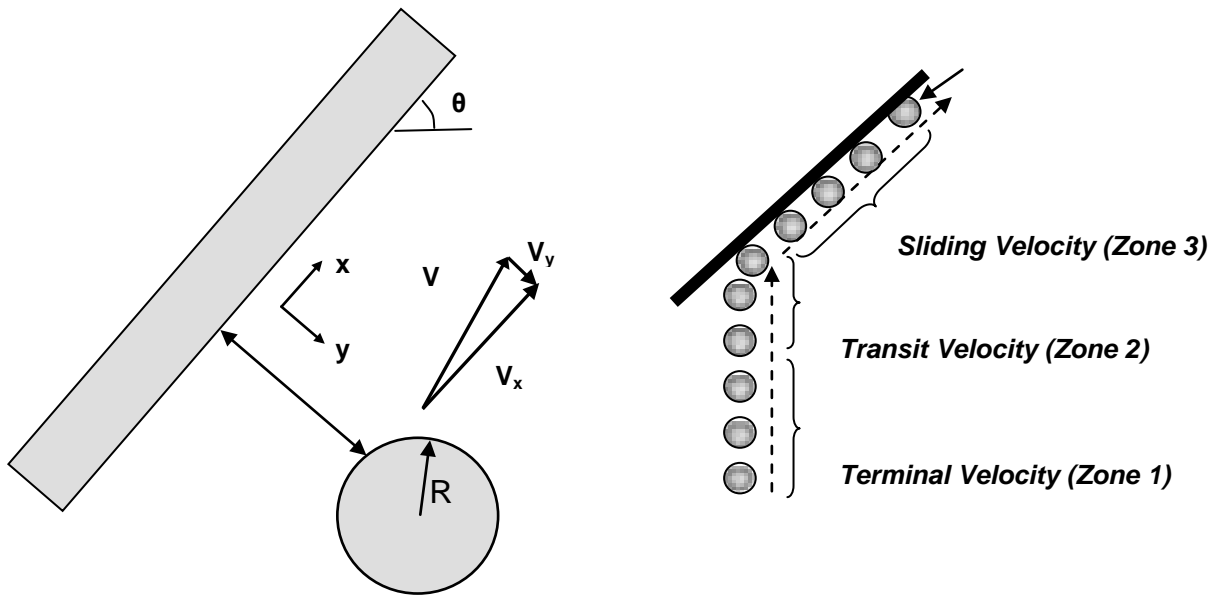


Figure 4.1 Bubble rising, transient and sliding velocity profiles. A crossing point of tangents of sliding velocity and transient velocity profiles is defined as the zero time point.

Preparation of solid surfaces

Four solid collector surfaces were used in this study: 1) hydrophilic silica wafer; 2) hydrophobized silica wafer; 3) teflon with uniform bitumen coating; and 4) teflon with non-uniform bitumen coating.

The hydrophobization of silica wafer was accomplished by soaking silica wafers in a 10% (v/v) solution of dichlorodimethylsilane (Aldrich, 99%) in toluene overnight. The wafers were then rinsed several times with toluene, dried in a fume hood through natural evaporation (Zhang et al., 2003) and stored in a sealed vial prior to the tests. The hydrophobized wafer had a water contact angle of $\sim 100^\circ$, measured with the captive bubble method using a drop shape analysis DSA10 system. In contact angle measurements, bubbles were introduced onto the solid surface using a micro syringe and the shape of the bubble was analyzed using the vendor-supplied software to obtain contact angle values.

A sample of bitumen feedstock, known as vacuum distillation feed bitumen obtained from Syncrude Canada, was used without any further treatment to prepare a bitumen-coated film on a teflon plate. The sample of feedstock bitumen was coated on a teflon plate using a spin coater (P6700, Specialty Coating Systems, USA) running at 6000 rpm for 15 min. As bitumen had a high viscosity, it resulted in a mirror-like thick and uniform bitumen surface coating. We named this surface as “uniform bitumen surface”.

To prepare a non-uniform bitumen surface, vacuum distillation feed bitumen (B), was diluted in toluene (T), at a (B:T) mass ratio of 1:5. The mixture was shaken for 30 minutes and then subjected to centrifugation to remove contained solids. The mixture was then coated on the teflon surface using a spin coater (P6700, Specialty Coating Systems, USA) running at 6000 rpm for 15 min. We named this surface as a “non-uniform bitumen surface”.

In this study, industrial recycle process water and simulated process water were used. The industrial recycle process water was obtained from the tailings pond of Syncrude Canada Aurora mine. As shown in Table 4.1, recycle process water has a fairly high electrolyte concentration. It also contains natural surfactants that were released during the oil sand extraction process (Schramm and Smith, 1985). The release of water-soluble natural surfactants was confirmed in our laboratory (Gu et al., 2002).

Table 4.1 Concentration of ions of interest in the industrial process water (pH = 8.3).

Ions	K ⁺	Na ⁺	Mg ²⁺	Ca ²⁺	Cl ⁻	SO ₄ ²⁻	HCO ₃ ⁻
Process water (mmol/L)	0.39	23.9	0.83	1.22	12.67	2.1	10.34

To study the role of natural surfactant contained in recycle process water, “simulated process water” was prepared using ultra pure (Millipore) water to contain the same level of inorganic electrolytes without including natural surfactant. The pH of the simulated process water was adjusted to 8.1. The amounts of salts added are given in Table 4.2. Use of the simulated process water allows investigations on the effect of surfactants present in the industrial process water on bubble sliding velocity and induction time.

Table 4.2 Recipe used for the preparation of the simulated process water (pH = 8.1).

Salt	KCl	NaCl	Na ₂ SO ₄	NaHCO ₃	CaCl ₂	MgCl ₂
(mmol/L)	0.39	8.16	2.1	10.34	1.22	0.83

In order to study the effect of dissolved gases on the bubble sliding velocity and the induction time, some tests were conducted using de-aerated process water. To de-aerate the process water, the process water sample was heated to and kept at 60°C for 4 hours. The heated water was then allowed to cool to the room temperature in a closed flask until used in the bubble-surface attachment tests.

Other methods of de-aeration such as by vacuum or heating at a higher temperature were not considered in this study. It was observed that heating the process water above 60°C resulted in the precipitation of salts on the collector surface and decomposition of natural surfactants, which

inevitably cause changes in chemical composition of industrial recycle process water. Due to the presence of natural surfactants in the process water, de-aeration under vacuum resulted in the continuous foaming and the formation of a stable layer of foam. Removal of this foam layer to obtain de-aerated process water would change the concentration of natural surfactants in the de-aerated process water as surfactants are known to be concentrated in the foam.

4.3 Results and discussion

A bubble velocity profile in Figure 4.1 exhibits three distinct zones:

Zone 1: the bubble attains its terminal velocity, which remains constant for almost 0.1s. This velocity depends on bubble geometry and the physicochemical properties of the medium and gas-liquid interfaces. The bubble surface, for example, can be mobile with a non-vanishing tangential velocity at the gas-liquid interface.

Zone 2: This is a transient velocity regime under the influence of a solid collector surface. The presence of solid collector decreases sharply the bubble rising velocity from its terminal velocity.

Zone 3: This is the bubble sliding regime, where the bubble moves along the inclined solid collector surface. Depending on the surface wettability two scenarios could occur. For a hydrophilic surface, the bubble continues to move with the same velocity until it leaves the surface, while for a hydrophobic surface the intervening liquid film between the bubble and

surface drains, leading to the rupture of the liquid and hence attachment of the bubble to the collector surface as a stationary bubble at the attachment point. To assist the discussion of our results we adopt the following terminology. A zero time was assumed to be the moment, when the bubble just made contact with the inclined surface and started its sliding motion. Graphically, a zero time point is shown in Figure 4.1 as the crossing point of tangents of sliding and transient velocity profiles.

4.3.1 Effect of temperature

One of the important factors to be considered in studies on the bubble rising and sliding velocities is the temperature of the liquid. Figures 4.2 and 4.3 show the results of the sliding velocity experiments, where either air (Figure 4.2) or CO₂ (Figure 4.3) bubbles interact with hydrophobized silica surfaces immersed in the industrial process water at three different temperatures. It is evident that the bubble terminal velocity increases with increasing process water temperature. A higher process water temperature caused a sharper decrease in bubble rising velocity over the transient velocity regime, but had a smaller effect on the final sliding velocity.

A striking feature revealed from these velocity profiles is a shorter induction time and easier attachment of sliding bubble to the solid collector surfaces at a higher process water temperature. Figure 4.3 shows similar observations for CO₂ bubbles sliding underneath the inclined solid

collector, although at a given temperature, the CO₂ bubbles exhibit a shorter induction time than air bubbles.

To have a better understanding of observed decrease in induction time with increasing process water temperature, the time required for depletion of liquid between bubble and planar surface was calculated using Equation (4-2) below:

$$t_{\text{induction}} = \frac{6\pi\mu R_b^2}{F} \ln\left(\frac{h_{\text{cr}}}{h_o}\right) \quad (4-2)$$

where μ is the liquid viscosity; h_o , initial distance between the bubble of radius R_b and collector surface; h_{cr} , a critical thickness; and F , the net driving force acting on bubble. The critical thickness is the thickness in which liquid film will rupture spontaneously. The detailed procedures for derivation of Equation (4-2) are given in Appendix A. In the derivation, a spherical bubble of radius R_b in relative motion of velocity V towards a planar surface was assumed. Equation (4-2) provides a direct relation between the induction time and the viscosity of liquid films intervening a bubble and a solid collector surface. As shown in Equation (4-2), a reduction in viscosity would cause a corresponding reduction in induction time.

Viscosity of water is a strong function of temperature. Viscosity variation with temperature was compared with the trend of changing induction time with the temperature as shown in Figure 4.4. Empirical model developed by Kampmeyer (1952) was used for water viscosity. Both induction time

and viscosity of process water showed similar temperature dependence, decreasing with increasing process water temperature. It is therefore natural to propose that a decrease in viscosity of process water with increasing temperature results in a higher terminal bubble rising velocity and shorter induction time, independent of the type of the gas bubbles used in this study.

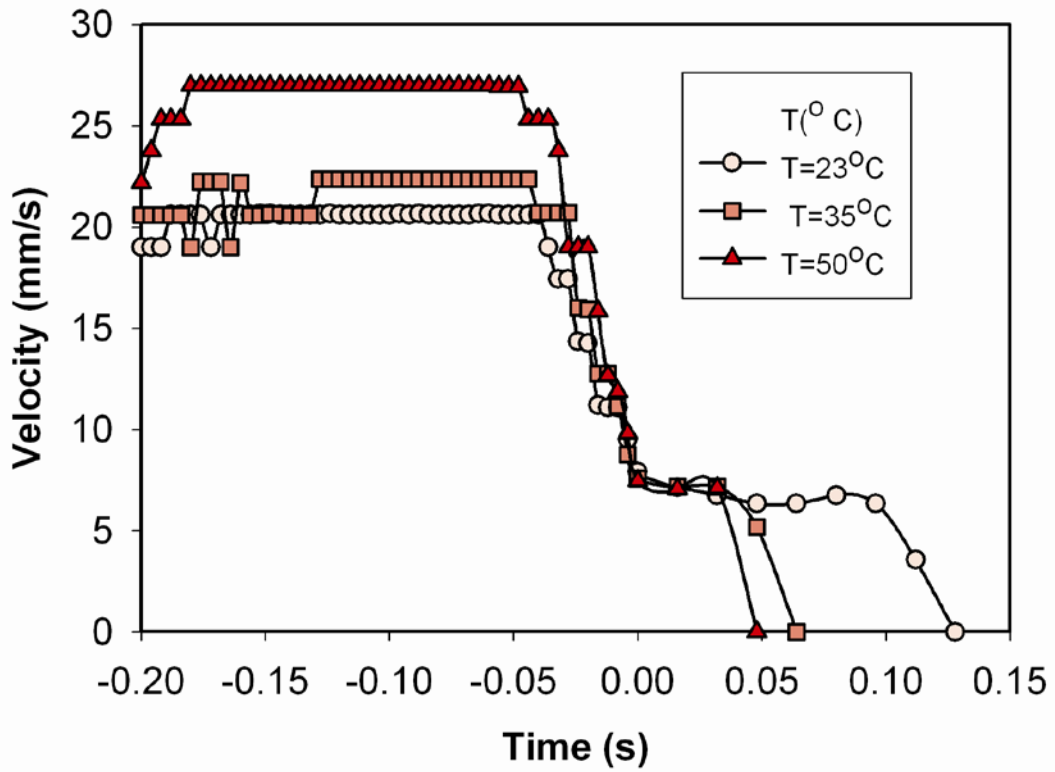


Figure 4.2 Effect of temperature on interaction of rising air bubbles (bubble diameter, $D = 0.22$ mm) with a hydrophobic silica surface immersed in process water (surface inclination = 60°).

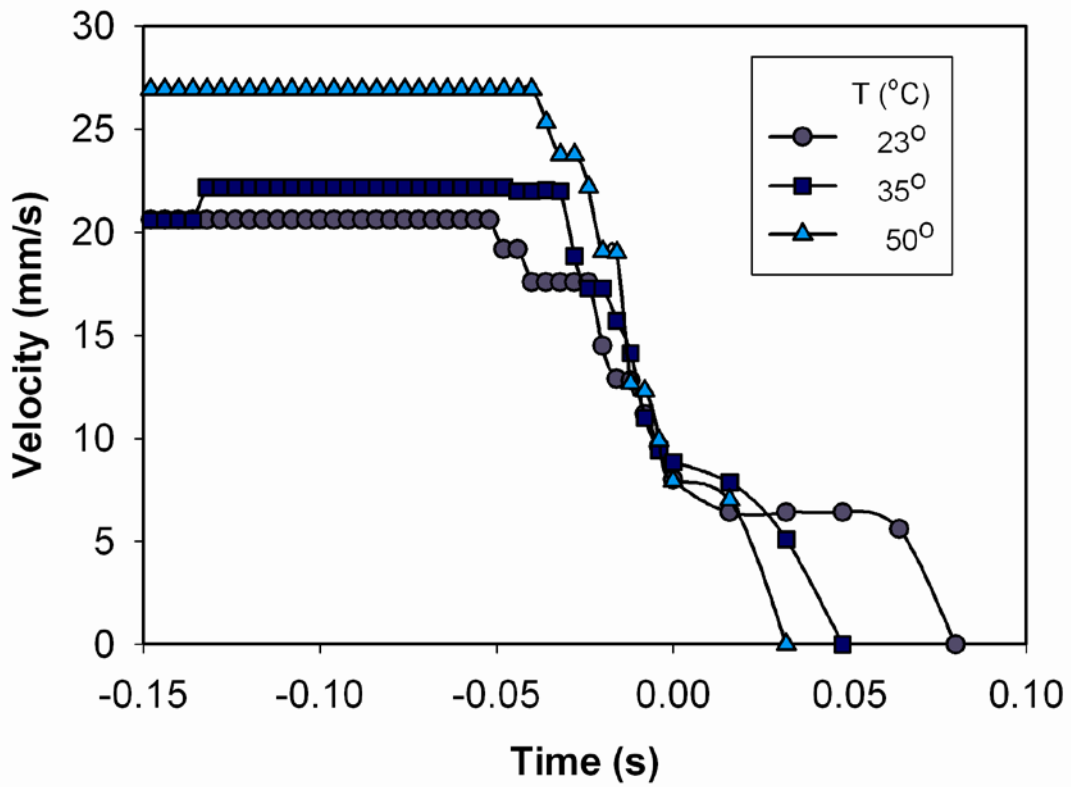


Figure 4.3 Effect of temperature on interaction of rising CO₂ bubbles (bubble diameter, D = 0.22 mm) with the hydrophobic silica surface in process water (surface inclination = 60°).

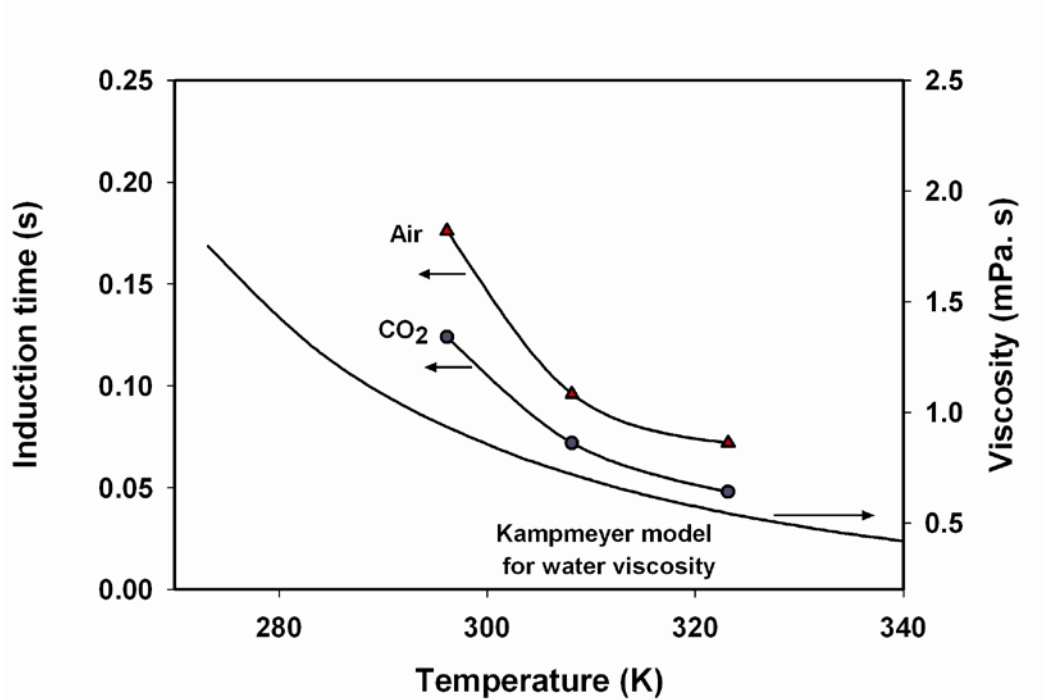


Figure 4.4 Effect of temperature on induction time and viscosity of water (bubble diameter, $D = 0.254$ mm).

4.3.2 Effect of bubble size

To investigate the effect of bubble size on bubble sliding velocity and induction time, tests were conducted for a given temperature with single air or CO₂ bubbles of two different sizes. As shown in Figure 4.5, the bubble size directly affects the terminal and sliding velocity. Regardless the type of gas bubbles, larger bubbles are of higher buoyancy and hence greater driving force, leading to a higher terminal and sliding velocity, with the effect being more pronounced for air bubbles.

Equation (4-2) shows that the induction time is proportional to the square of the bubble radius. For a given gas type, the results in Figure 4.5 show a longer induction time for larger size bubbles even though a higher buoyancy force exists to thin the intervening liquid film between sliding gas bubbles and inclined solid collector surface. These results are consistent with previously published work by Gu et al. (2004).

4.3.3 Effect of type of gas bubbles

To study the effect of gas type on the bubble sliding velocity and induction time, bubble rising and sliding velocities were determined using various types of gas bubbles (air, CO₂, H₂ and O₂) and a hydrophobized silica surface as the solid collector surface.

The results in Figure 4.6 show that for a given condition, bubbles of all gas types have the same bubble rising and sliding velocities. The induction time of CO₂ bubbles, however, is much shorter than that of the other gas

bubbles. It is known, that CO_2 has a much higher solubility in aqueous media than the other gases. Dissolution of CO_2 from rising and sliding CO_2 bubbles causes a fast shrinkage of bubble. The reduction in bubble size by CO_2 dissolution is detectable in Figure 4.6 from the step-wise reduction in rising and sliding velocity of CO_2 bubbles. The reduction in bubble size would contribute to a shorter induction time as observed in Figure 4.5. In addition to the effect of bubble size reduction due to higher dissolution rate of CO_2 bubbles, the dissolution of CO_2 during bubble rising and sliding motion may cause a CO_2 concentration gradient in the front and back of CO_2 bubbles, leading to a higher surface mobility which may contribute to a faster thinning kinetics of intervening liquid films.

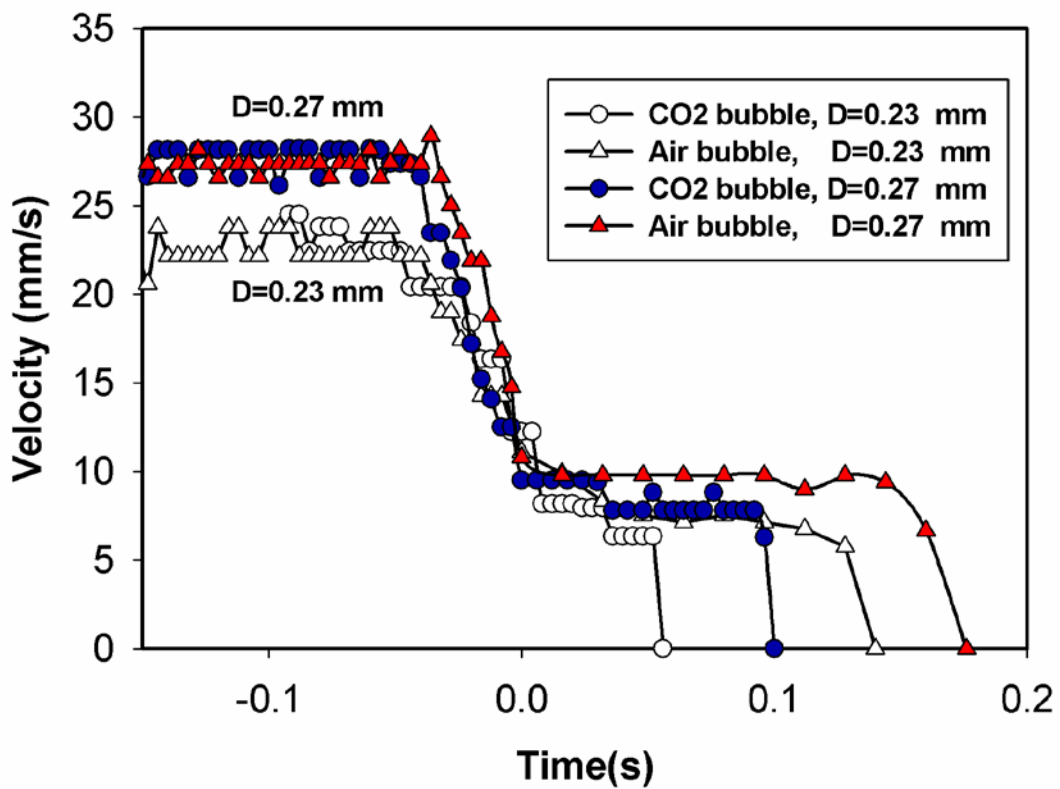


Figure 4.5 Velocity profile of air and CO₂ bubbles (open symbols for D = 0.23 mm and filled symbols for D = 0.275 mm) toward and along hydrophobized silica surface in process water (surface inclination = 60°, T = 23 °C).

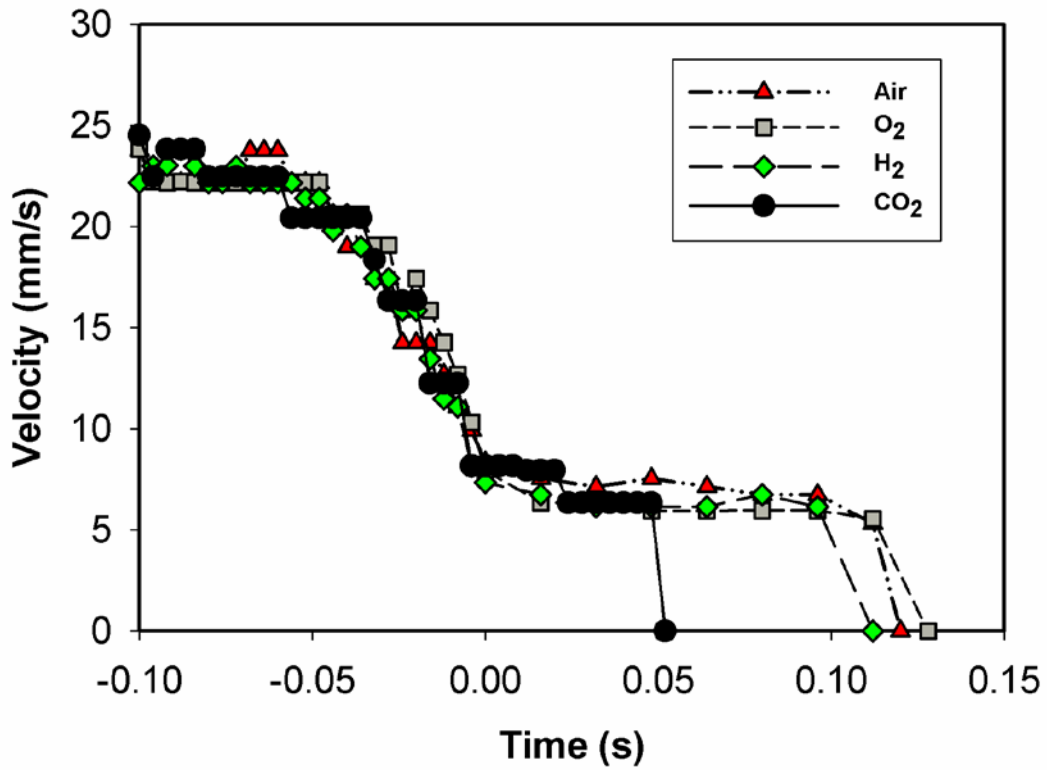


Figure 4.6 Effect of gas types on bubble rising and sliding velocities ($D=0.23$ mm) toward the hydrophobized silica surface in process water (surface inclination = 60° , $T = 23$ °C).

4.3.4 Effect of surface wettability

The effect of surface wettability on bubble sliding velocity and induction time was investigated using hydrophobized silica and teflon with uniform bitumen coatings. The results depicted in Figure 4.7 show a negligible impact of surface type on bubble rising terminal velocity. A strong impact of surface type on the induction time was, however, evident. Although the induction time of bubbles attaching to the solid collector surface is shorter for CO₂ bubbles than for air bubbles, the induction time on the hydrophobized silica surface is much shorter than on the uniform bitumen-coated teflon surface for bubbles of both gas types.

In order to better understand the observed impact of surface type on induction time, the dynamic contact angle of CO₂ and air bubbles on these two types of surfaces in the process water was measured through water phase as schematically shown in the insert of Figure 4.8. The results in Figure 4.8 show a significantly higher initial contact angle value for hydrophobized silica than for uniform bitumen-coated teflon. Also shown in this figure, there is a slightly higher contact angle value for CO₂ bubbles than for air bubbles. A slightly larger contact angle value for CO₂ bubble than air bubble indicates slightly stronger interactions of solids with CO₂ bubbles than with air bubbles and/or a slightly higher surface tension of CO₂-water interface than air-water interface. Clearly, higher contact angle values or poor wettability lead to a shorter induction time. For example, hydrophobized silica has a much higher contact angle value than uniform

bitumen coated-teflon, accounting for a much shorter induction time observed for bubbles attaching to hydrophobized silica than to uniform bitumen-coated teflon. It is also consistent that the use of CO₂ bubbles leads to a shorter induction time than the use of air bubbles, as the contact angle values measured using CO₂ bubbles are higher than that using air bubbles.

It is interesting to note that the contact angles measured using air and CO₂ bubbles on the hydrophobized silica or air bubbles on uniform bitumen-coated teflon do not change with time. However, a significant increase in contact angle with increasing the contact time of CO₂ bubbles on uniform bitumen-coated teflon was observed. After six seconds, the contact angle value measured with CO₂ bubbles on bitumen exceeded the value measured with CO₂ bubbles on hydrophobized silica. A few physicochemical processes could contribute to such an increase in contact angle with contact time. It is conceivable that high solubility of CO₂ gas would lead to a decrease in CO₂ bubble volume with time due to continuous CO₂ dissolution. As a result, one is measuring contact angle with bubbles of continuous reduction in gas bubble volume. This process is equivalent to approaching advancing contact angle of the system, therefore leading to a larger apparent contact angle value. On the other hand, bitumen appears to have a stronger physico-chemical interaction with CO₂ bubbles than with air bubbles in process water, leading to a much significant engulfment of bitumen on CO₂ bubbles than on air

bubbles upon the formation of the three phase contact. The bitumen engulfment on the bubbles would expand the three phase contact line as the engulfment proceeds, resulting in a higher contact angle value. The detailed study on mechanism of such dynamic behaviour is beyond the scope of this thesis. Nevertheless, our study clearly showed that the initial contact angle is the controlling parameter for induction time of bubble-bitumen attachment as it is measured before the intervening liquid film rupture. Should the final or pseudo equilibrium contact angle be a determining factor, one would expect a shorter induction time for CO₂ bubble attaching to uniform bitumen-coated teflon than attaching to hydrophobized silica, which is clearly in contradiction with our experimental results.

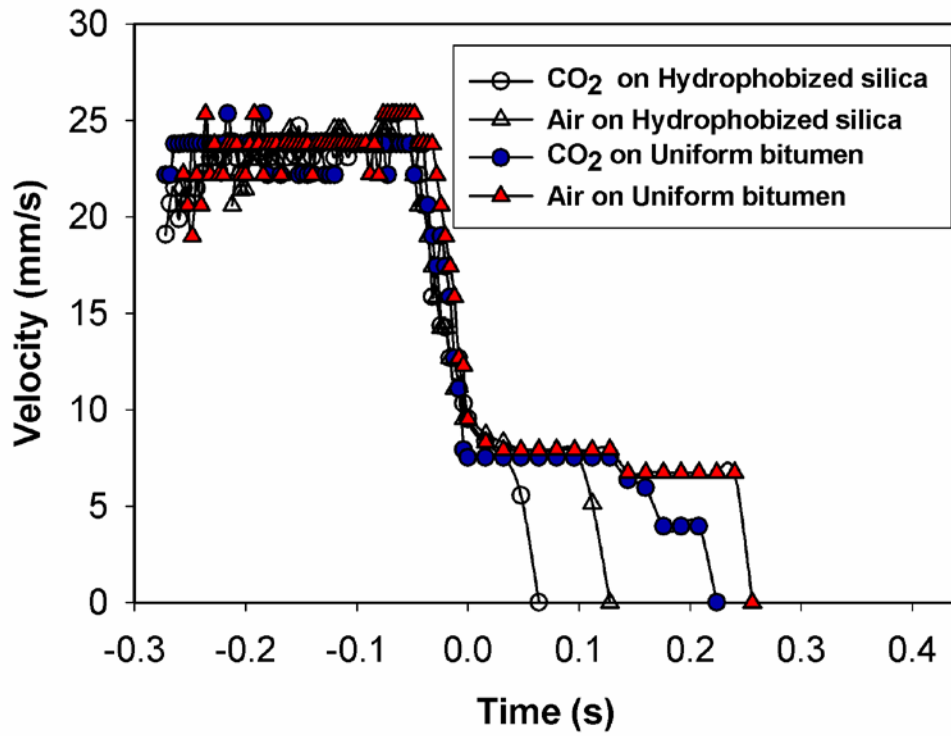


Figure 4.7 Effect of collector surface types on bubbles (bubble diameter, $D = 0.25$ mm) rising and sliding velocities in process water (surface inclination = 60° , $T = 23$ °C).

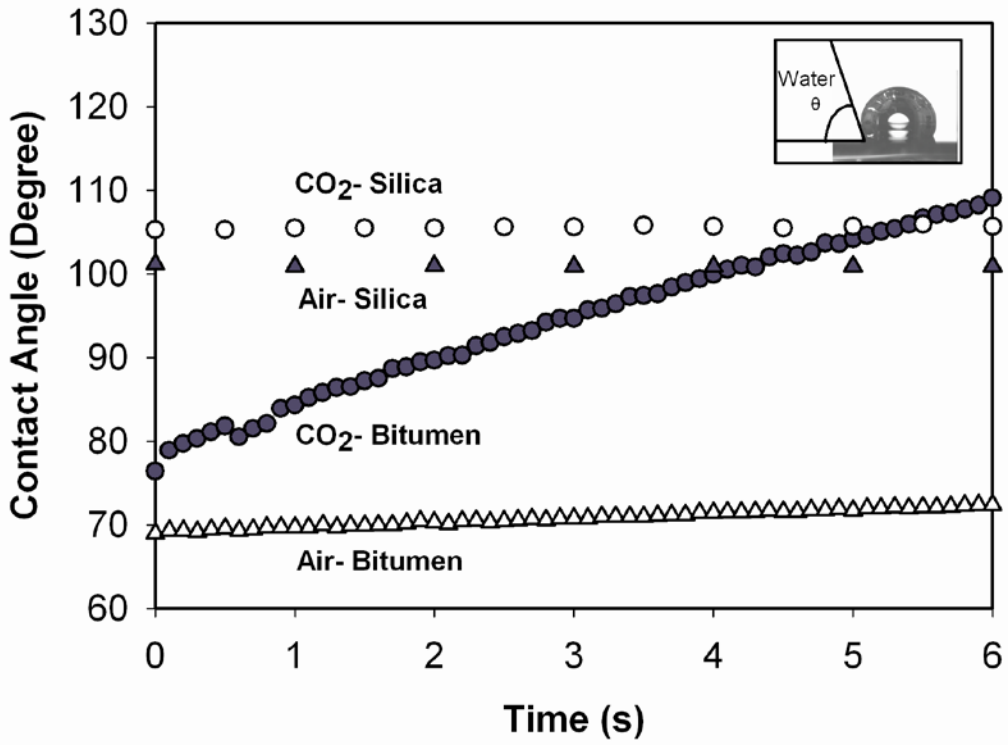


Figure 4.8 Effect of surface type (uniform bitumen surface and hydrophobic silica surface) and gas type (air and CO₂) on dynamic contact angle variation in process water.

4.3.5 Effect of dissolved air

It is well established that the structure of water near a water/ solid interface is significantly different from water structure in the bulk. The water structure near a solid surface could extend as much as 10 to thousands of water molecular diameters. The structure and density difference of water near various solids are strongly dependent on surface hydrophobicity. Strong dipole interaction and hydrogen bonding of a water molecule adjacent to a hydrophilic surface causes normal orientation of water dipole moment and a higher density than bulk water molecules. Minimized hydrogen bonding of water molecules near a hydrophobic surface on the other hand causes water molecules to orient parallel to the surface, leading to a lower packing density of water molecules (Drost-Hansen, 1969). This is one of the theories accounting for non-DLVO repulsive hydration and attractive hydrophobic forces (Yoon et al., 1997). A hydrophilic surface induces a stable water liquid film between a bubble and a solid surface. Additional forces are required to thin this stable film, leading to a longer induction time. The repulsion between water and a hydrophobic surface makes the intervening liquid film between a bubble and the solid surface unstable, leading to a faster film rupture and shorter induction time. This effect would be manifested by the presence of gas molecules in the liquid.

To understand the effect of dissolved gas on bubble sliding velocity and induction time, the process water and de-aerated process water were

used in bubble sliding experiments. The results in Figure 4.9 show a negligible effect of dissolved air or CO₂ on corresponding bubble rising terminal velocity and sliding velocity. However, a significant decrease in the induction time was observed when the process water was aerated as compared with the measurement used for de-aerated water. It is interesting to note that the degree of reduction in induction time by aeration for CO₂ and air was similar.

The difference in the measured induction time in the aerated and de-aerated process water arises from the spontaneous nucleation or entrapment of nano - size bubbles on the hydrophobic solid surface in water (Stockelhuber et al., 2003; Tyrrell and Attard, 2001, 2002; Ishida et al., 2002) due to hydrophobicity and/or surface roughness (Steitz et al., 2006; Zhang et al., 2007; Krasowskak et al., 2007). The presence of such nano bubbles was suggested by studies using IR spectroscopy and atomic force microscopy (Tyrrell and Attard, 2001, 2002). During the drainage of the intervening film between a hydrophobic surface and bubble, the presence of gas molecules near hydrophobic surfaces increases the mobility of liquid films on the solid and hence a faster drainage, leading to a shorter time to reach the critical thickness of the film for spontaneous rupture. After the rupture of the film, the presence of gas molecules facilitates the spontaneous formation of gas nuclei, leading to a quick expansion of three-phase contact to stop bubble sliding.

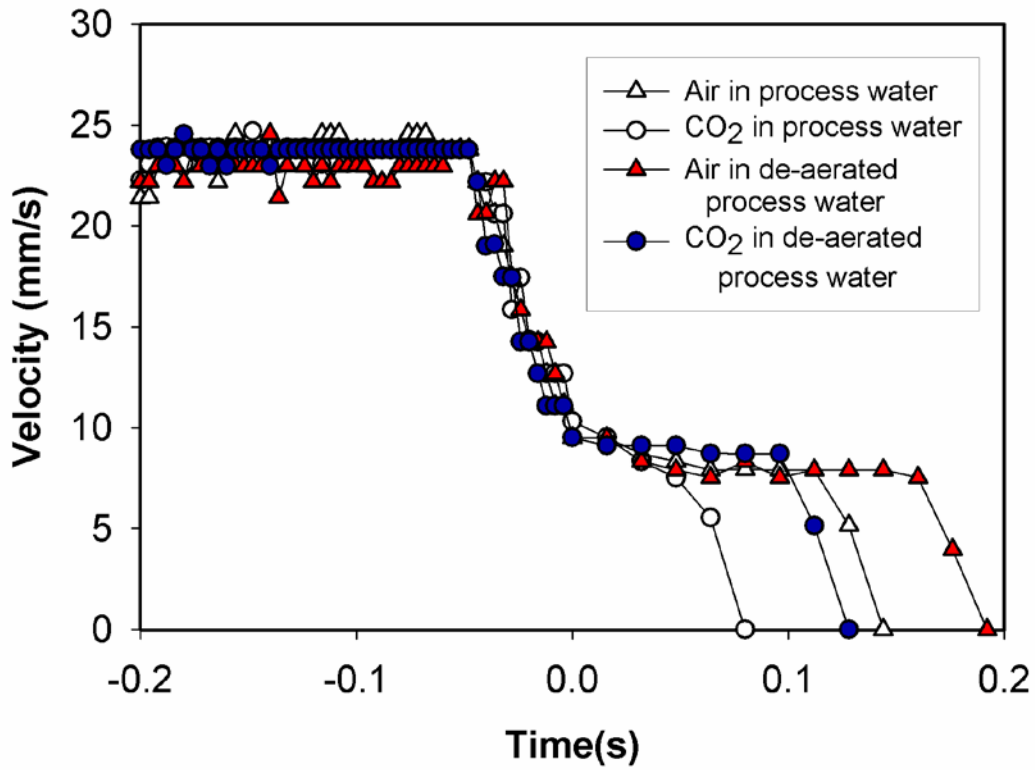


Figure 4.9 Effect of de-aeration of process water on bubble rising and sliding velocities ($D = 0.25 \text{ mm}$) with hydrophobized silica surface at surface inclination of 60° and $T = 23 \text{ }^\circ\text{C}$.

4.3.6 Effect of surface non-uniformity

Previous studies showed that physical and chemical heterogeneity at a solid -liquid interface has a significant impact on film rupture (Simmons and Chauhan, 2006). Film rupture and bubble attachment occur at a critical liquid film thickness at which the film becomes highly unstable.

The surface heterogeneities or non-uniformity creates non-uniform intervening liquid films, as schematically illustrated in Figure 4.10. Kargupta and Sharma (2002) showed that liquid film thinning rate is a function of local film thickness. Consequently for non-uniform surfaces, the rate of film thinning would be higher, leading to a shorter induction time. Optical images of four surfaces used in this study are shown in Figure 4.11. High non-uniformity of bitumen surface on teflon is shown in Figure 4.12C. The sliding velocity and induction time of air and CO₂ bubbles sliding underneath non-uniform and uniform bitumen-coated teflon surfaces in the process water are shown in Figure 4.12. Although the surface non-uniformity showed a negligible impact on bubble sliding velocity, the induction time of both air and CO₂ bubbles attaching to an inclined bitumen collector surface was much shorter for non-uniform bitumen surfaces than for uniform bitumen surface.

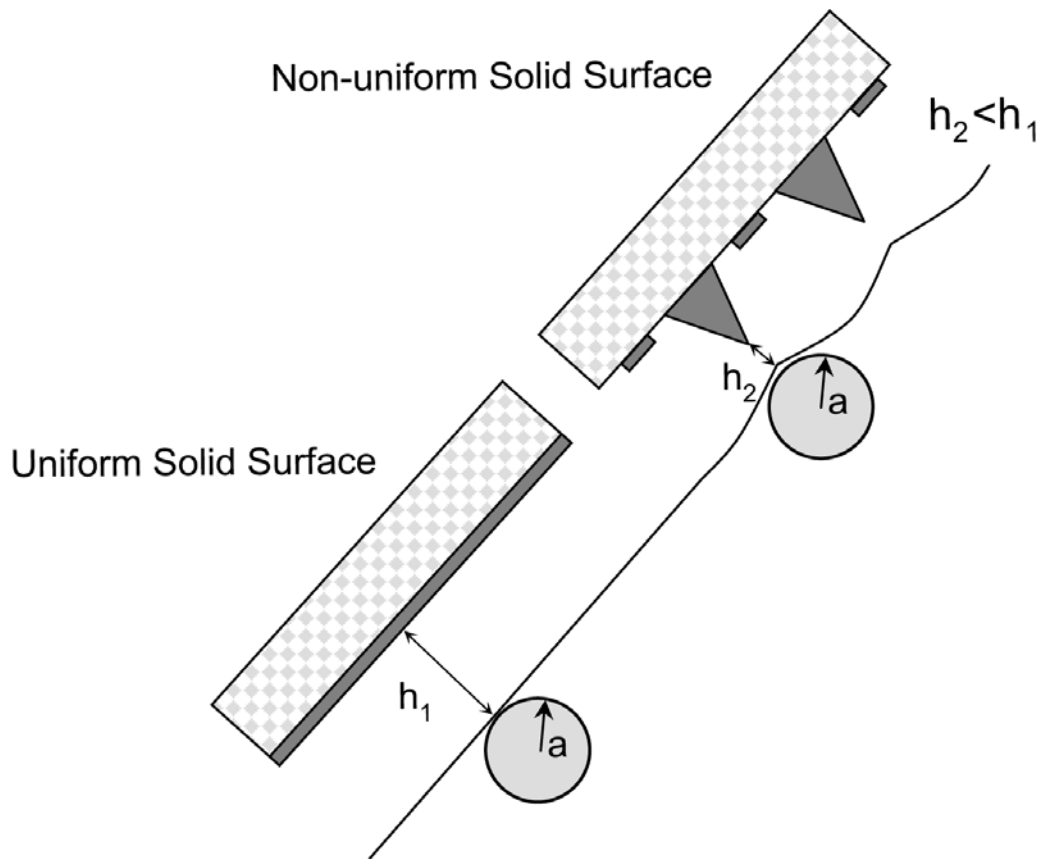


Figure 4.10 Schematic representation of a surface non-uniformity effect on bubble attachment.

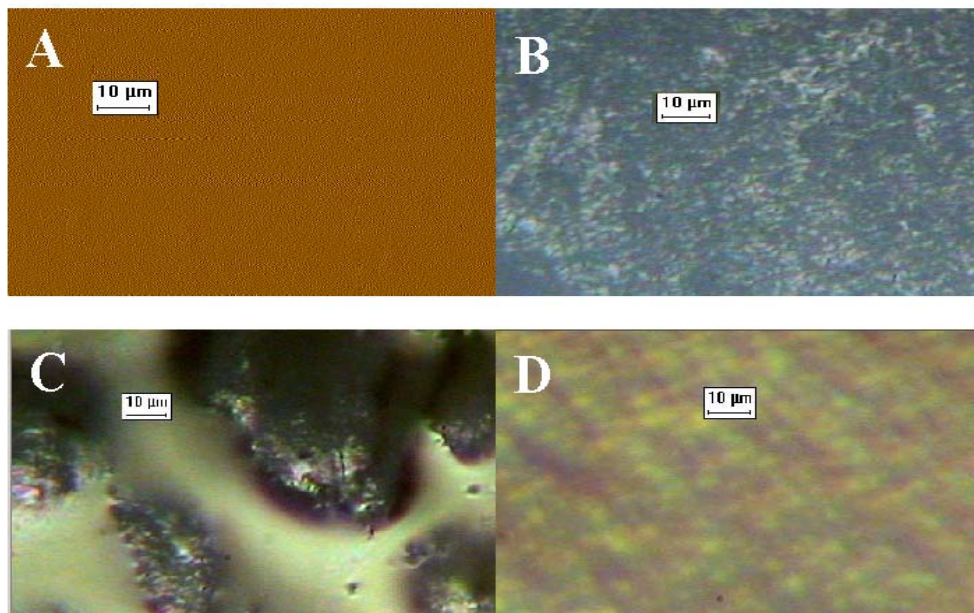


Figure 4.11 Micrograph of: (A) hydrophobized silica surface; (B) teflon plate; (C) non-uniform layer of bitumen on teflon surface; and (D) uniform bitumen layer on teflon surface.

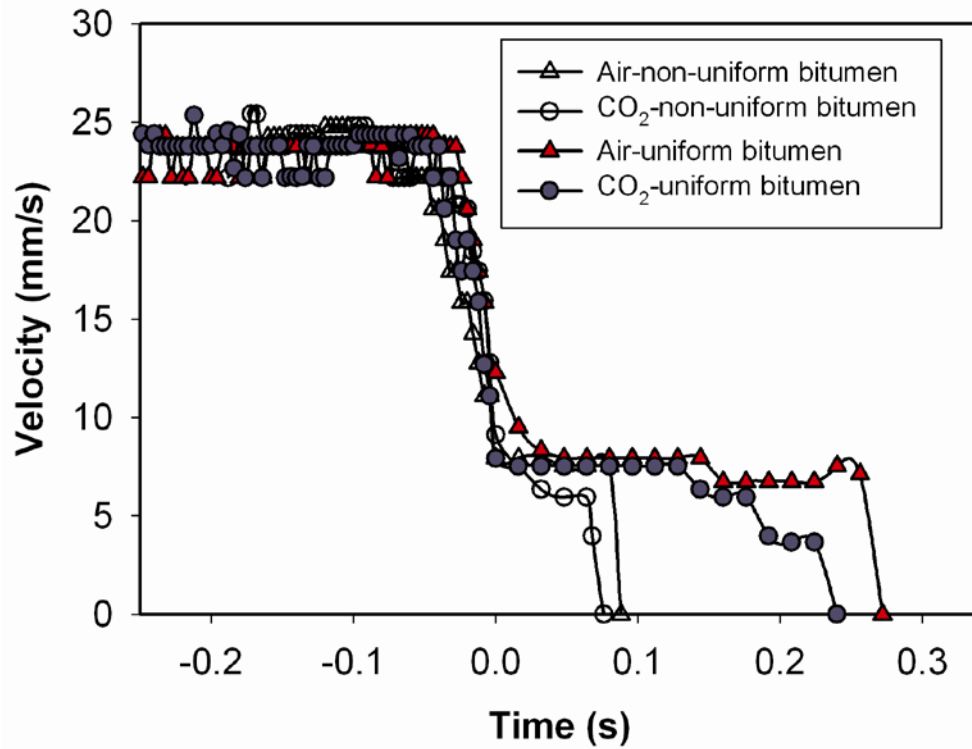


Figure 4.12 Effect of surface non-uniformity on bubble rising and sliding velocities ($D = 0.25$ mm) in process water with surface inclination 60° and $T = 23$ °C.

4.3.7 Effect of dissolved surfactants

To study the effect of dissolved natural surfactants on bubble sliding velocity and induction time, process water and simulated process water were used as the experimental medium. The results in Figure 4.13 show that the presence of surfactant in the process water reduces slightly the oxygen bubble rising terminal velocity, but has a negligible effect on the bubble sliding velocity. However a much longer induction time was observed when the oxygen bubble was in the process water rather than in the simulated process water without surfactant. The results clearly demonstrate a significant negative impact of natural surfactant in the process water on bubble-bitumen attachment. The finding is consistent with previous work by Gu et al. (2003, 2004).

The presence of natural surfactants in water affects oxygen-water interfacial viscosity due to the accumulation of hydrated polar groups of natural surfactant at the interface. The presence of surfactant at the bubble-liquid interface affects the bubble hydrodynamic (Levich, 1962). A direct consequence of surfactant adsorption at oxygen-water interface is that resistant forces due to increased rigidity of the interface and interactions of hydrophilic head groups of surfactant with surround water molecules become more dominant in the rising bubbles, hence reducing its terminal rising velocity for a given bubble size. The hydrated liquid film on oxygen bubble will also increase the drag force exerted on the bubble. Higher drag force causes a smaller terminal velocity. The presence of

surfactant at the oxygen-water interface also induces a hydrated layer of water around oxygen bubbles thereby stabilizing intervening liquid film, which, in turn, results in a lower thinning kinetics and, hence, longer induction time.

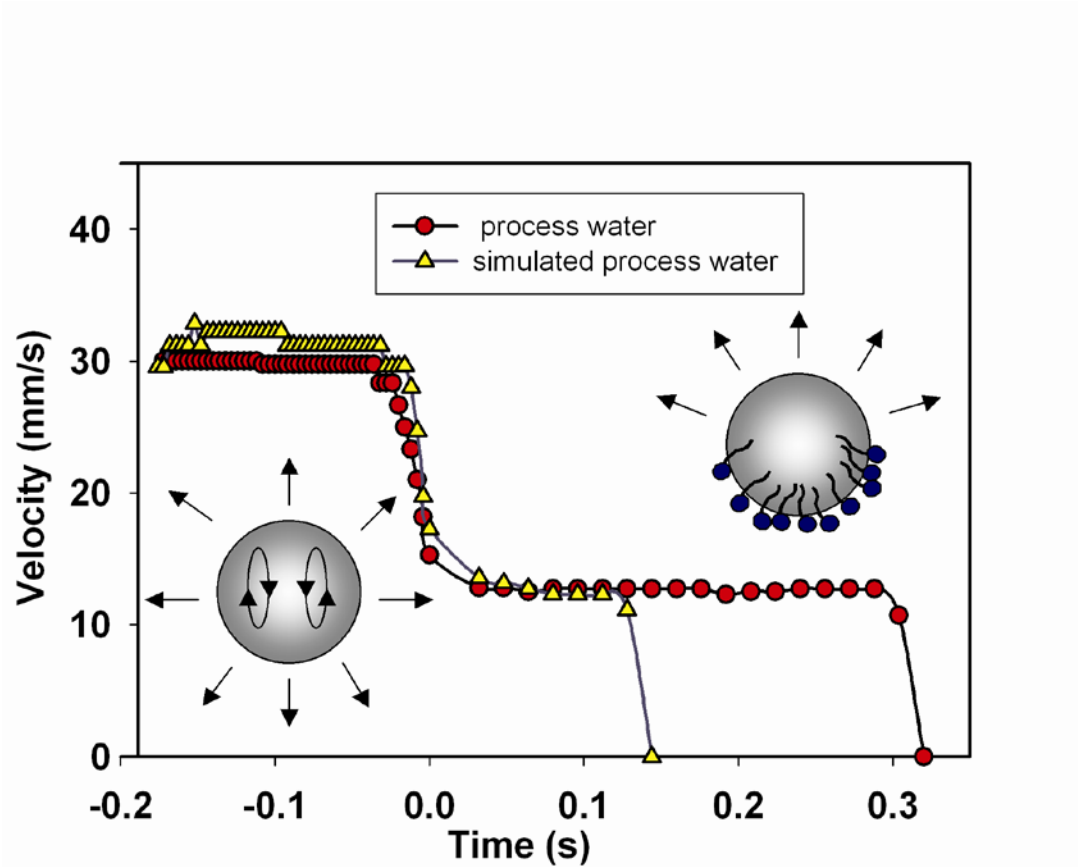


Figure 4.13 Effect of surfactants on oxygen bubble's rising and sliding velocities ($D = 0.25$ mm) with uniform layer bitumen surface in process water and simulated process water at surface inclination of 60° and $T = 50^\circ\text{C}$.

4.4 Conclusions

The present study on single micro-bubble sliding underneath and attaching to the inclined solid collector surface leads to the following conclusions:

- 1) Terminal and sliding velocities of bubbles are function of temperature and they increase with increasing liquid temperature.
- 2) Induction time used to quantify bubble-solid attachment was found to reduce significantly with increasing liquid temperature, reducing bubble size and presence of surface non-uniformity.
- 3) Induction time is reduced for surfaces of increasing hydrophobicity.
- 4) For a given solid surface, the induction time measured with CO₂ bubbles is shorter than that measured with air, oxygen and hydrogen bubbles, and it is, possibly, due to shrinkage of CO₂ bubbles.
- 5) The terminal and sliding velocities of bubbles are independent of gas content in the liquid. However, a much shorter induction time is obtained using aerated process water compared to using de-aerated process water.
- 6) The presence of natural surface active agents in the process water reduces bubble terminal rising velocity and increases the induction time of bubble-solid attachment.

CHAPTER 5: EXPERIMENTAL AND THEORETICAL STUDY OF A SINGLE SMALL BUBBLE SLIDING MOTION ALONG AN INCLINED SURFACE

5.1 Introduction

Studies on the dynamics of a sliding gas bubble along a collector surface are a milestone in understanding several industrial processes, such as bitumen recovery, froth flotation, soil remediation, de-inking of recycle paper and heat transfer in boiler (Crawford and Ralston, 1988; Hewitt et al. 1995; Dai et al., 1988, 1999, 2000; Dobby and Finch, 1987; Nguyen et al., 2004, 2005).

There is a considerable volume of literature on sliding bubble dynamics. Maxworthy (1991) studied bubbles with higher Reynolds number under an inclined plate. As Zukoski (1966), he also found that the bubble rising velocity increases with increasing bubble size and inclination angle. He also reported critical angle for maximal sliding velocity.

Masliyah et al. (1994) performed experiments of bubbles rising under plates at low Reynolds number. They reported increasing of sliding velocity with increasing inclination angle.

Masliyah et a. results were also confirmed by Tsao and Koch (1994, 1997) in their work on small size bubbles rising under inclined plates. In addition, they reported bouncing motion of sliding bubbles at higher inclination angles.

Bubble motion depends on the wettability of solid collectors. On a hydrophilic surface, the bubble continues to move with a constant sliding

velocity until it leaves the surface, while on a hydrophobic surface, the intervening liquid film between the bubble and surface drains, leading to the rupture of the liquid film and attachment of the bubble. In the case of hydrophilic collector surface, the intervening liquid film is stable and spontaneous film rupture does not occur during bubble sliding.

In this work, bubble sliding motion on the hydrophilic surface was theoretically modelled. Experimental data were collected and compared with developed analytical model.

5.2 Experimental procedure

In order to avoid bubble deformation and, thereby, the complexity in interpreting the data, experiments in this study were carried out using bubbles smaller than 0.4 mm. This is confirmed by calculating the Weber number, We , using Equation (5-1):

$$We = \frac{2\rho_L V^2 R_b}{\gamma} \quad (5-1)$$

where ρ_L is the liquid density, V - bubble velocity, R_b - bubble radius and γ surface tension of solution. Based on the maximum terminal velocity of the bubbles used in our study, We number was in the range of $1.4 \cdot 10^{-3}$ to $1.1 \cdot 10^{-2}$, indicating that these bubbles maintained fairly spherical shape during the rising and sliding (Masliyah et al. 1994).

As mentioned earlier, generation of micro-bubbles of a given size is a challenging task. Electrolysis was used for generation of H_2 and O_2 bubbles.

The electrolysis apparatus to generate small H₂ or O₂ bubbles was adopted from Gu et al. (2004), (Figure 5.1 A and B). Bubbles were generated by a DC power supply. The polarity of electrodes placed in bubble collector tube was used to generate bubbles of desired gas type. Hydrogen bubbles were generated at cathode (-) while oxygen bubbles were produced at anode (+). Electrodes were made from a platinum wire (OD = 25 μm). Small bubbles generated from the electrode was collected in a collector tube (Figure 5.1C), where they were coalesced to make a larger bubble. Once a bubble of a desired size was produced in the bubble collection tube, the bubble was pushed out from the tube by gentle flow of water through a syringe and it rose in the liquid medium toward the suspended collector surface. There should be sufficient distance between the bubble collector tube and the collector surface in order for a bubble to reach its terminal velocity prior to the point, when collector surface starts to affects bubble dynamics. In these experiments, the distance was set to 3 mm.

Experiments were conducted in a temperature-controlled chamber. All the experiments were recorded with a high-speed digital imaging system (Motion Scope R 8000S, Red Lake Imaging, USA) at a capture speed of 500 frames per second (fps). The bubble travel time and velocity were measured by tracing the bubble motion for a series of consecutive frames. Dimensions of the view field were calibrated using a scale of known length and set to 2.5 x 2.5 mm.

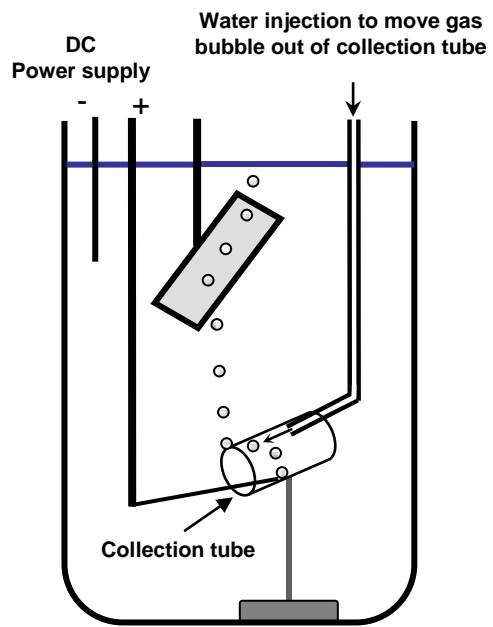
Preparation of solid surfaces:

Two solid collector surfaces were used in this study: 1) hydrophilic silica wafer; 2) bitumen coated on teflon.

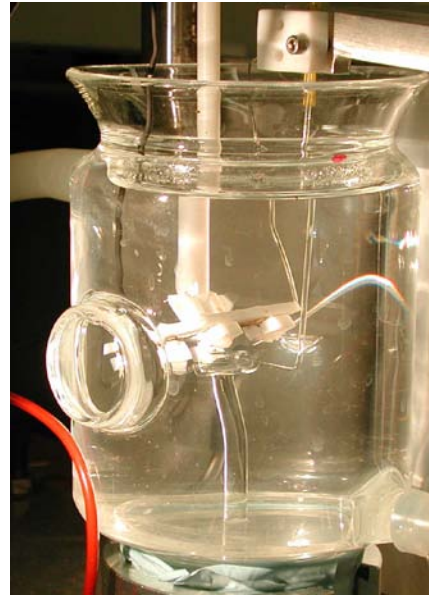
A sample of bitumen feedstock, known as vacuum distillation feed bitumen obtained from Syncrude Canada Ltd., was used without any further treatment to prepare a bitumen film on a teflon plate. The bitumen was coated on a teflon plate using a spin coater (P6700, Specialty Coating Systems, USA) running at 6000 rpm for 15 min. As bitumen had a high viscosity, it resulted in a mirror-like thick and uniform bitumen surface.

In this study, industrial recycle process water and simulated process water were used. The industrial recycle process water was obtained from the tailings pond of Syncrude Canada Aurora Mine. As shown in Table 3.1, recycle process water has a fairly high electrolyte concentration. It also contains natural surfactants that were released during the oil sands extraction process (Schramm and Smith, 1985). The release of water-soluble natural surfactants was confirmed in our laboratory (Gu et al. 2002).

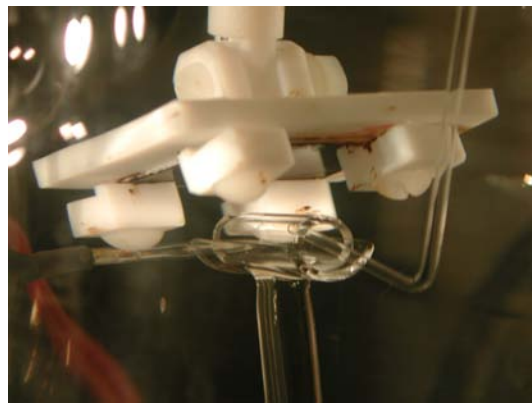
To study the role of natural surfactants contained in recycle process water, “simulated process water” was prepared using ultra pure (Millipore) water to contain the same level of inorganic electrolytes without including natural surfactant. The pH of the simulated process water was adjusted to 8.1. The amounts of salts added are given in Table 3.2. Use of the simulated process water allows investigating the effect of surfactants presented in the industrial process water on bubble terminal and sliding velocity.



A



B



C

Figure 5.1. Experimental apparatus for micro-bubble generation by electrolysis.

5.3 Equation of motion

To describe the motion of a bubble with density ρ_B and volume V , which rises initially at terminal velocity U in a quiescent aqueous medium toward an inclined wall, the following approach was adopted.

To analyse and classify bubble motion, four important dimensionless groups can be used (Clift et al., 1978):

Reynolds number:
$$Re = \rho_L d_e U / \mu_L \quad (5-2)$$

Eotvos number:
$$Eo = g \Delta \rho d_e^2 / \gamma \quad (5-3)$$

Morton number:
$$M = g \mu_L^4 \Delta \rho / \rho_L^2 \gamma^3 \quad (5-4)$$

Weber number:
$$We = \rho_L U^2 d_e / \gamma = Re^2 (M/Eo)^{1/2} \quad (5-5)$$

Here ρ_L and μ_L are the fluid density and viscosity, respectively, and γ is interfacial tension. U is the terminal rise velocity of the bubble in an infinite medium, g is the acceleration due to gravity and d_e is the equivalent bubble diameter. In our case, since there is no deformation and the bubbles are assumed to be spherical, d_e becomes the bubble diameter.

Reynolds number is a measure of the ratio of inertial to viscous forces, while Eotvos number is a measure of the ratio of the gravitational to the interfacial forces. The Morton number is a function of the fluid properties.

As bubble approaches a wall, the rising bubble interacts with the wall, and hence, the We number plays an important role.

As a bubble travels with terminal velocity and approaches the collector surface, the bubble velocity profile exhibits three distinct zones (Figure 4.2):

Zone 1: The bubble attains its terminal velocity, which remains constant for almost 0.1 s. This velocity depends on bubble geometry and the physicochemical properties of the medium and gas-liquid interfaces. The bubble surface, for example, can be mobile with non-vanishing tangential velocity at the gas-liquid interface.

Zone 2: This is a transient velocity regime under the influence of solid collector surface. The presence of a solid collector decreases sharply the bubble rising velocity from its terminal velocity.

Zone 3: This is the bubble sliding regime, where the bubble moves along the inclined solid collector surface. On a hydrophilic surface, the bubble continues to move with the same velocity until it leaves the surface. To assist in the discussion of our results we adopted the following terminology. A zero time was assumed to be the moment when the bubble just made contact with the inclined surface and started its sliding motion.

Graphically, a zero time point is shown as the crossing point of tangents of sliding and transient velocity profiles (Figure 4.1).

5.3.1 Bubble motion in zone 1

There are several models developed to describe motion of bubbles moving at their terminal velocity. Among these models the following relationship is valid for spherical gas bubble ($D < 1$ mm), (Dewsbury et al., 1999):

$$U = \left[\left(\frac{4g\mu(\rho_L - \rho_g)}{3\rho_L^2} \right) \left(\frac{\text{Re}_t}{C_D} \right) \right]^{1/3} \quad (5-5)$$

Here Reynolds number at terminal velocity is given by:

$$\text{Re}_t = \frac{\rho_L d_b U}{\mu}, \quad (5-6)$$

where μ is viscosity of the liquid phase, d_b , is gas bubble diameter and C_D , is the drag coefficient. To evaluate C_D , Dewsbury et al. (1999) used following correlation (Turton and Levenspiel, 1986):

$$C_D = \frac{16}{\text{Re}_t} (1 + 0.173 \text{Re}_t^{0.657}) + \frac{0.413}{1 + 16300 \text{Re}_t^{-1.09}} \quad (5-7)$$

for clean bubble, and

$$C_D = \frac{24}{\text{Re}_t} (1 + 0.173 \text{Re}_t^{0.657}) + \frac{0.413}{1 + 16300 \text{Re}_t^{-1.09}} \quad (5-8)$$

for a retarded or contaminated bubble.

As shown in the above equations, the properties of the gas/liquid interface of a bubble are one of the main factors determining the bubble motion. In the case of pure liquids, the bubble surface is fully mobile. As a result of this surface mobility the bubble velocity is higher than that of a solid sphere of identical diameter.

The presence of natural surfactants in water affects the bubble-water interfacial viscosity due to the accumulation of hydrated polar groups of natural surfactant at the interface. The presence of the surfactant at the bubble-liquid interface affects the bubble hydrodynamics (Levich, 1962). A direct consequence of surfactant adsorption at a bubble-water interface is increased drag force thereby reducing the bubble rising terminal velocity.

5.3.2 Bubble motion in zone 2

Hydrodynamic interaction between a rising bubble and non deformable planar solid surface in a quiescent fluid is a concern. Here we focus on the short range of hydrodynamic interactions, taking place between a spherical bubble and a planar solid surface at different inclination angles. When the separation distance asymptotically approaches zero, the framework of the lubrication approximation can be applied to solve the short range hydrodynamic interaction, which gives rise to the dependence of the drag force F , on the separation distance H .

$$F = -6\pi\mu RU f_1 \quad (5-9)$$

in which:

$$f_1 = \frac{R}{mh} \quad (5-10)$$

here U is the bubble velocity relative to the solid surface, R is the bubble radius, μ is the liquid viscosity, and f_1 describes the deviation of the drag force from the Stokes law and is referred to as the correction factor. f_1 also describes the dependence of the drag force on the separation distance h .

Parameter m accounts for the mobility of the bubble surface: $m = 4$ if the bubble surface is mobile and $m = 1$ if the bubble surface is immobile (Schulze, 1984). This equation is valid only at the limit $h \rightarrow 0$, the framework of the lubrication approximation. It does not reduce to the correct asymptotic value of 1 in the limit $h \rightarrow \infty$ when the bubble is far from the surface.

Models for zones 2 and 3 depend on the distance of a bubble from the surface. Therefore, experimental data from the measurements of the bubble velocity while approaching the flat surface were used to determine the boundaries between zones 1, 2 and 3. As observed, a bubble that travels with its terminal velocity would reduce the speed upon approaching the flat surface. The distance of a moment, on which bubble starts its impact velocity from the surface, is the starting point for zone 2. As the bubble approaches the surface with reduced speed, there is a deviation point in the trajectory of the bubble from upward to a parallel to the surface

movement. The distance between this deviation point and the surface is the end of the zone 2 and a beginning of the zone 3.

After determination of boundaries for the zone 2, the deviation factor from the Stokes equation is calculated using Equation (5-10), while Equation (5-9) is used to evaluate bubble velocity in the zone 2.

5.3.3 Bubble motion in zone 3

The equation of motion for a bubble centroid is obtained by estimating the different forces acting on the bubble:

$$V \frac{dU}{dt} = F_{\text{buoyancy}} + F_{\text{drag}} + F_{\text{added mass}} + F_{\text{Basset}} + F_{\text{wall}} \quad (5-11)$$

where the forces are buoyancy, drag, added mass, Basset and wall forces respectively. We can write:

$$F_{\text{buoyancy}} = (\rho_L - \rho_b) \frac{4}{3} \pi R_b^3 g \sin \theta \quad (5-12)$$

$$F_{\text{drag}} = -6 \pi \mu U f_3 R_b \quad (5-13)$$

$$F_{\text{added mass}} = -C_{vm} \rho_L \frac{dU}{dt} \quad (5-14)$$

In Equation (5-14) C_{vm} is the bubble added mass coefficient.

Klaseboer et al., (2000; 2001) established that Basset force did not have strong influence on the bubble dynamics. Therefore, we removed it from the force balance equation.

The F_{wall} force results from excess pressure exerted on the top of the bubble, which corresponds to a deformation of the interface.

$$F_{\text{wall}} = \iint (\Delta p) n_x dx dz \quad (5-15)$$

If P_B is considered to be the pressure inside the bubble and P_L be the pressure just outside the bubble interface, the pressure difference for the deformed interface will be:

$$P_L - P_B = -\gamma \left(\frac{1}{R_x} + \frac{1}{R_z} \right) \quad (5-16)$$

The effect of the wall can therefore be computed as the spatial integral of the pressure difference between the spherical and the deformed interfaces. Therefore the excess pressure ΔP can be written as:

$$\Delta P = \gamma \left(-\left(\frac{1}{R_x} + \frac{1}{R_z} \right) + \frac{2}{R} \right) \quad (5-17)$$

In the case of a spherical bubble $\Delta P = 0$ and subsequently $F_{\text{wall}} = 0$,

Equation (5-11) reduces to:

$$V \frac{dU}{dt} = F_{\text{buoyancy}} + F_{\text{drag}} + F_{\text{added mass}} \quad (5-18)$$

or

$$\frac{4}{3} \pi R^3 \left(C_{vm} + \frac{\rho_b}{\rho_l} \right) \frac{dU}{dt} = (\rho_l - \rho_b) \frac{4}{3} \pi R^3 g \sin \theta - 6 \pi \mu U f_{3(H)} R_b \quad (5-19)$$

Solution of the above differential equation is:

$$U_{\text{sliding (H)}} = \frac{\exp\left[\frac{-6\pi\mu f_{3(H)} R_b t}{\frac{4}{3}\pi R_b^3 (C_{vm} + \frac{\rho_b}{\rho_l})}\right] - \left[(\rho_l - \rho_b) \frac{4}{3}\pi R_b^3 g \sin\theta\right]}{6\pi\mu f_{3(H)} R_b} \quad (5-20)$$

In the above equation, $f_{3(H)}$ is the function of hydrodynamic resistance and can be calculated using (Nguyen and Schulze, 2004):

$$f_3 = \left\{ 1 + 0.498 \left\{ \ln \left[1.207 \left(\frac{R_b}{H} \right)^{0.986} \right] + 1 \right\}^{1.027} \right\}^{0.979} \quad (5-21)$$

As described in Section 5.3.2, after determination of boundaries for the zone 2 and 3, the hydrodynamic resistance is calculated using Equation (5-21), while Equation (5-20) is used to evaluate bubble velocity in the zone 2.

5.4 Results and discussion

5.4.1 Effect of plate inclination angle

Inclination of the solid surface determines the physical condition, at which a bubble contacts a surface. Physical orientation of the bubble with respect to the solid surface is an important factor in determination of the final force balance.

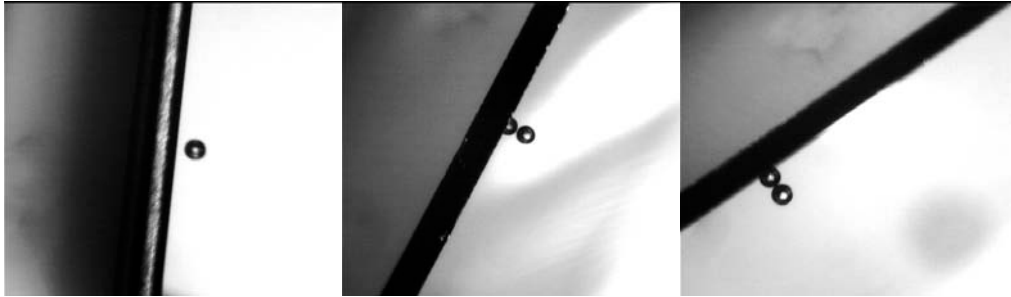
The buoyancy force reaches its maximum, when the bubble is far away from the wall. As the bubble approaches the solid surface, the buoyancy force results into two orthogonal components: a perpendicular component is applied to deplete the intervening liquid between the bubble and the

solid surface and a parallel component, which pushes bubble to slide along the solid surface. Increase in the inclination angle results in smaller perpendicular component. Smaller perpendicular component of the buoyancy force means weaker driving force, which results in a thicker intervening liquid film. The bubble travels at a larger distance from the solid surface with higher velocity (Figure 5.2).

As shown in Figure 5.3, higher inclination angle leads to higher sliding velocity regardless of gas type. Figure 5.4 shows a negligible impact of surface inclination angle on the bubble terminal velocity.

As bubble approaches to the solid surface, the approach velocity decreases. The rate of the velocity change depends on the solid surface inclination angle. Also, the position and specific distance, at which the bubble deviates from vertical motion, depend on the inclination angle. The bubble sliding velocity is a strong function of the solid surface inclination angle: higher inclination angle leads to higher sliding velocity (Figures 5.4 and 5.5). This observation is consistent with the previously published results of the Masliyah et al. (1994).

In our study, experimental results are in good agreement with the proposed model. However, our observation shows that as the solid surface inclination angle increases, the model prediction starts to deviate from experimental results.



Teta = 85

Teta = 60

Teta = 30

Figure 5.2 Sliding of a hydrogen bubble under a silica wafer surface, $D = 0.35 \text{ mm}$, $T = 23 \text{ }^\circ\text{C}$.

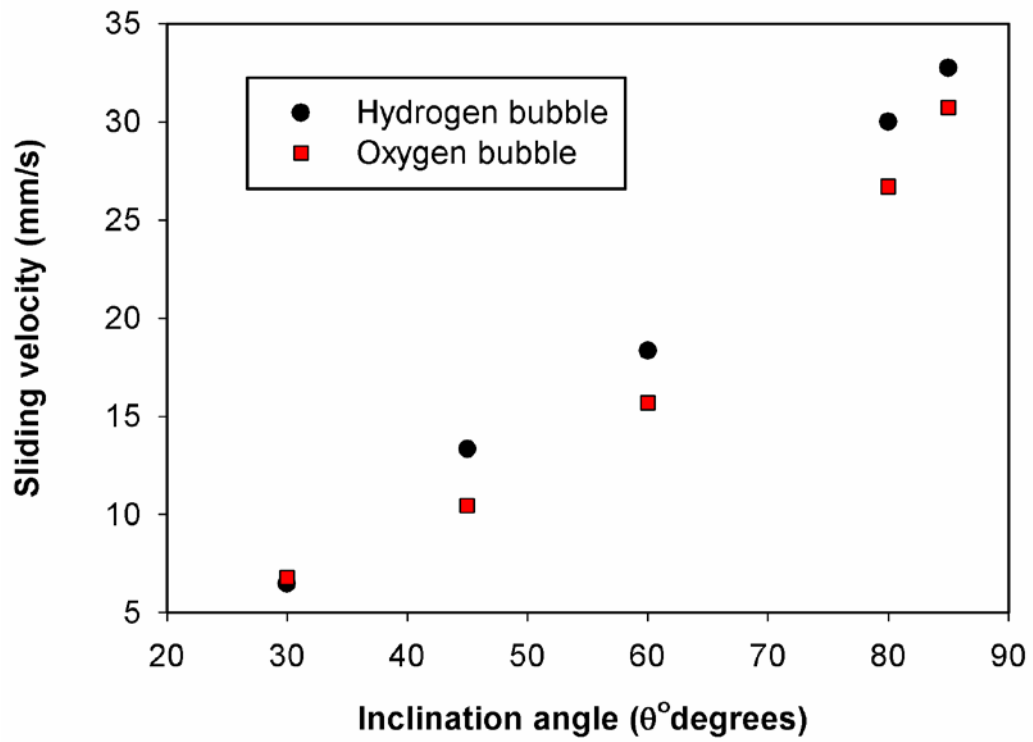


Figure 5.3 Effect of surface inclination on sliding velocity of hydrogen and oxygen bubbles under a hydrophilic silica wafer surface, $D = 0.35$ mm, $T = 23$ °C.

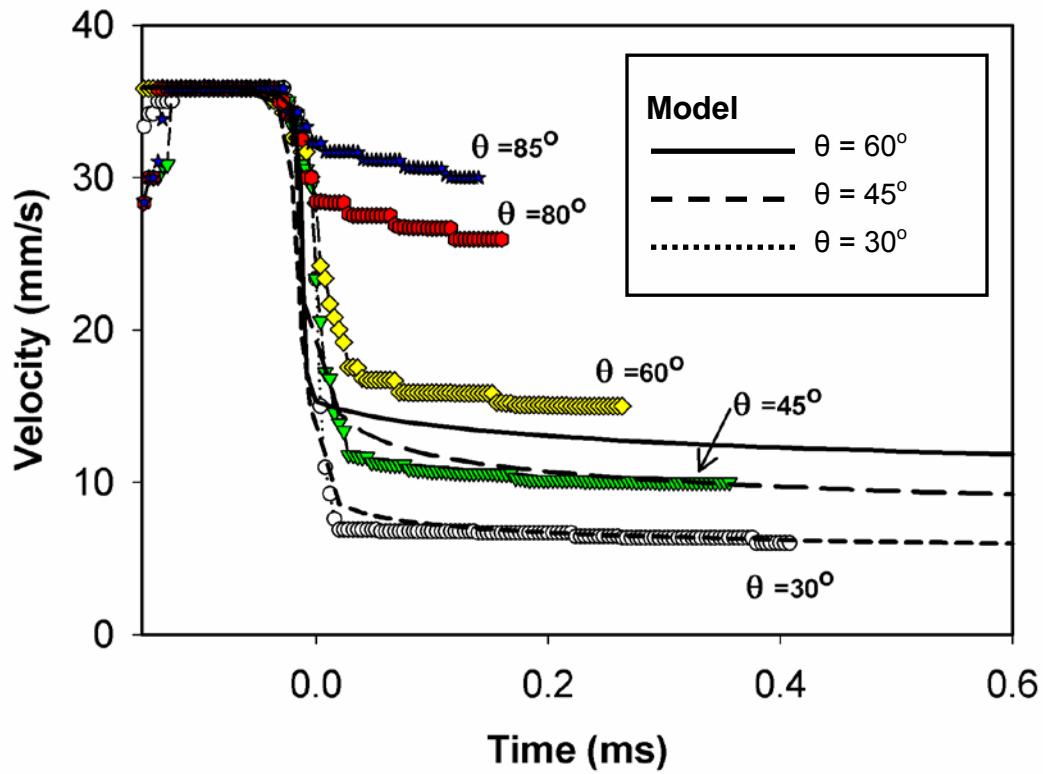


Figure 5.4 Effect of inclination on rising velocity of hydrogen bubbles ($D = 0.35$ mm) under a hydrophilic silica surface ($T = 23$ °C).

5.4.2 Effect of temperature

Temperature is an important factor in bubble velocity studies, as there is a reduction in viscosity with increasing temperature, which results in a significant changing terminal, impact, and sliding velocities.

The bubble terminal velocity increased with temperature, most probably, due to reduction in water viscosity with temperature (Figure 5.5). For comparison, variations of water viscosity with temperature are shown on the same graph. It is evident that the increasing bubble terminal velocity is corresponding well with a decrease in water viscosity.

Our results in Figure 5.6 show that an increase in water temperature results in an increase in terminal, transient and sliding velocities. As will be shown at a late stage, this finding is also in good agreement with the proposed mathematical model.

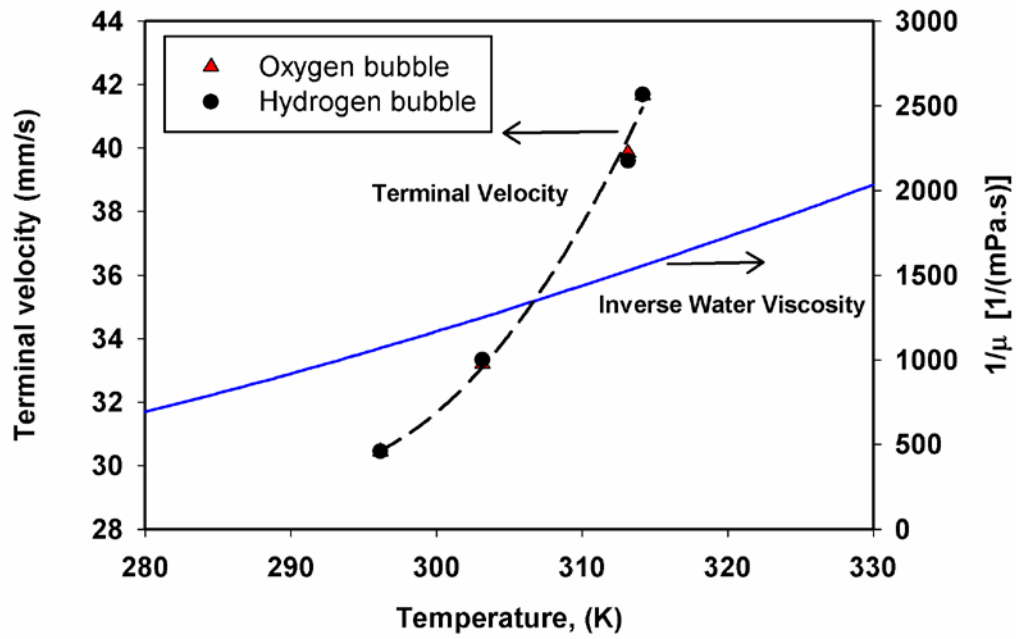


Figure 5.5 Effect of temperature on water viscosity and bubble ($D = 0.3$ mm) terminal velocity.

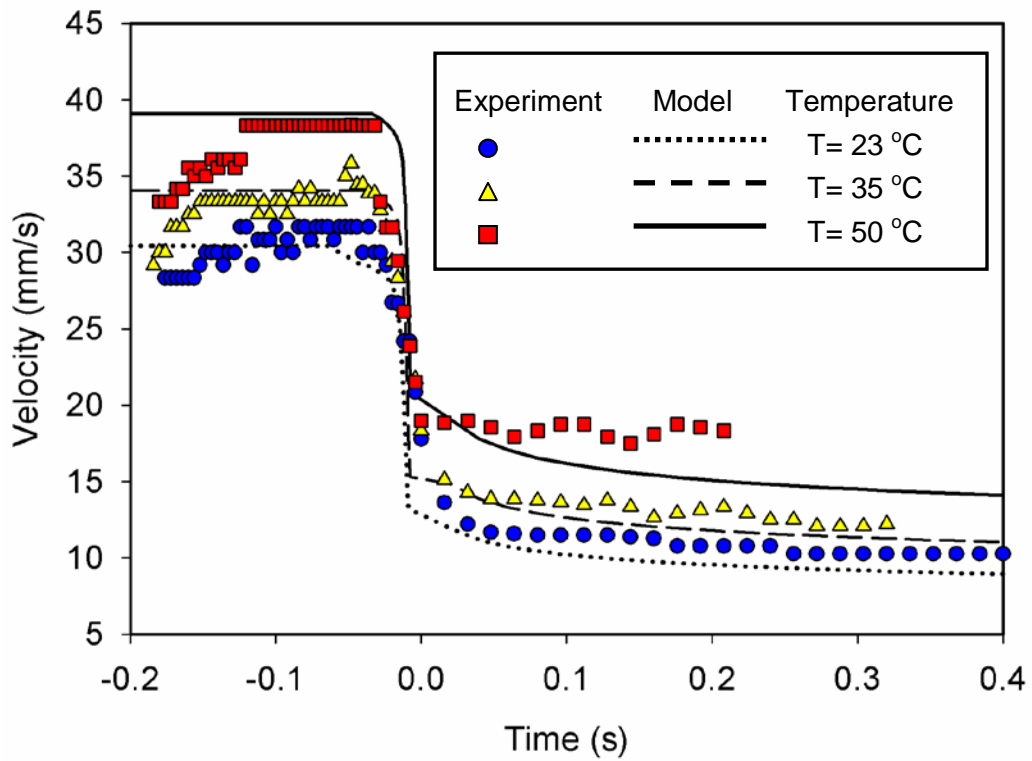


Figure 5.6 Effect of temperature on bubble velocity ($D = 0.3 \text{ mm}$) under an inclined hydrophilic silica wafer surface (surface inclination = 60°).

5.4.3 Effect of bubble size

A series of experiments were conducted using bubbles of different sizes, while the other conditions, such as temperature, inclination angle and chemical additives, were kept constant. Our results show that an increase in bubble size led to an increase in bubble velocities. Larger bubbles feature faster terminal, transient and sliding velocities (Figure 5.7).

Bubble size has a major impact on terminal and sliding velocity as shown in Equations (5-6) and (5-20). All the forces regardless whether they are driving or resistance forces depend on bubble size. Among these forces, the buoyancy force is of higher order of dependence on the bubble size. This phenomenon translates to increases in driving forces with bubbles of larger size.

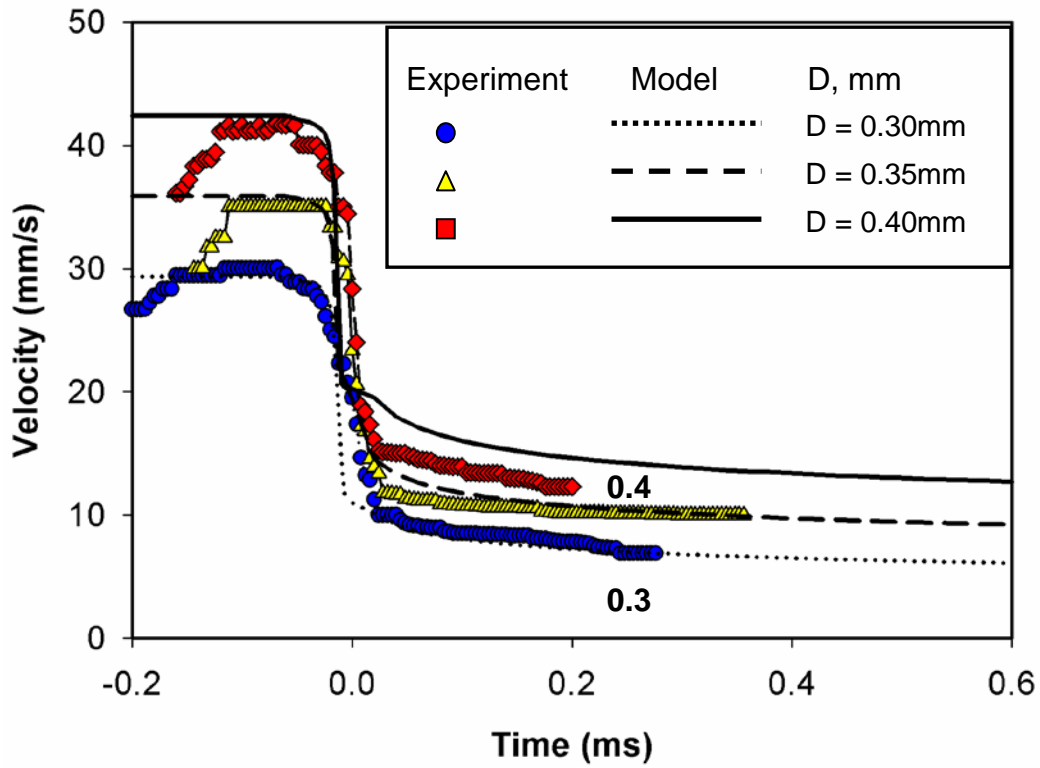


Figure 5.7 Effect of bubble size on hydrogen bubble velocities sliding under a silica wafer surface (surface inclination = 45°), T = 23 °C.

5.4.4 Effect of natural surfactants

To study whether dissolved natural surfactants have an effect on the bubble sliding velocity, process water and simulated process water were used as the experimental medium.

In process water, there are several different types of natural surfactants in addition of inorganic anions and cations. To understand the role of surfactant, simulated process water was also used. Simulated process water contains all species that the process water has, excluding natural surfactants (Table 4-2).

Our results show that the presence of surfactants in the process water causes a significant reduction in the terminal velocity of rising oxygen bubble, and at the same time has a negligible effect on the bubble sliding velocity (Figure 5.8 and 5.9).

The presence of natural surfactants in water affects oxygen-water interfacial viscosity due to accumulation of hydrated polar groups of natural surfactants at the interface. The presence of the surfactants on the bubble-liquid interface affects also the bubble hydrodynamic (Levich 1962). The bubble terminal velocity is reduced due to the formation of the adsorption layer, which retards the interface mobility. A direct consequence of the surfactant adsorption at the oxygen-water interface is a drastic increase in drag resistant forces on the rising bubbles, thereby reducing the terminal rising velocity for a given bubble size.

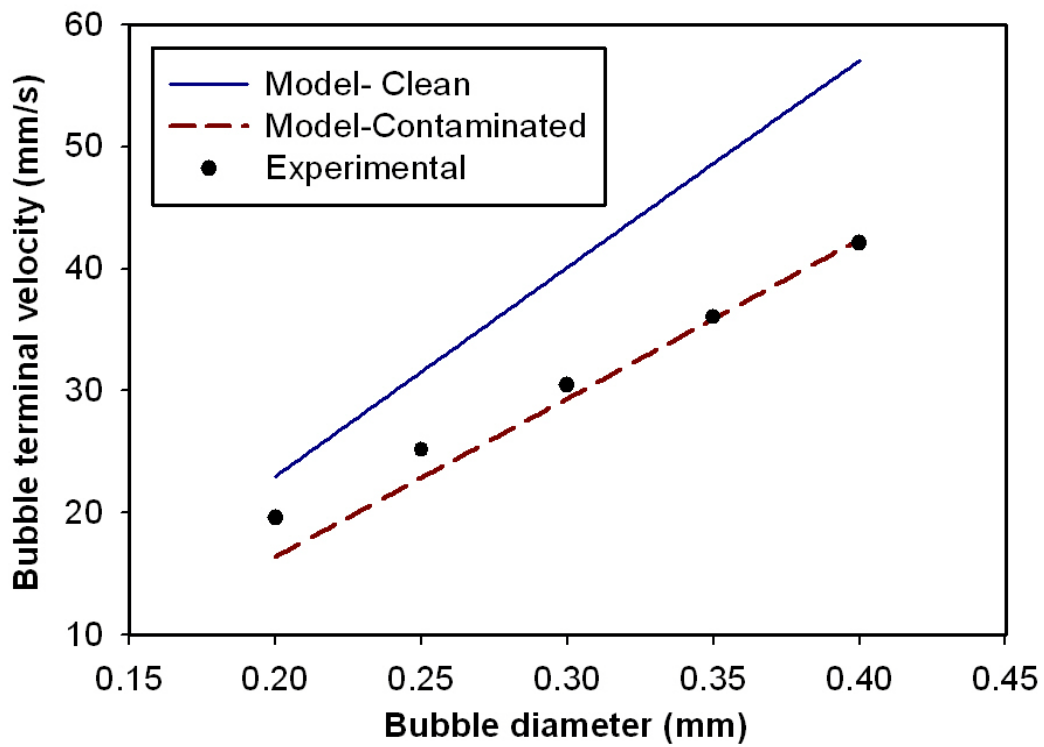


Figure 5.8 Comparative analysis of the effect of bubble size on its terminal velocity, calculated for clean or contaminated water environment and compared with the measured values for oxygen bubbles.

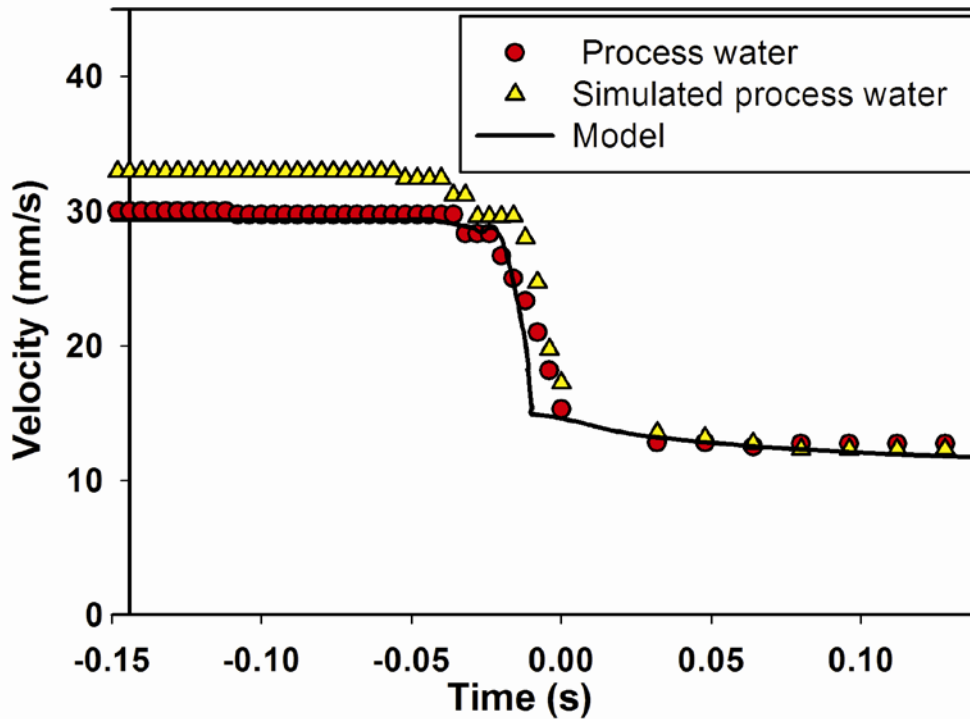


Figure 5.9 Effect of surfactants on oxygen bubble rising and sliding velocities ($D = 0.25$ mm) under a uniform layer of bitumen coated on a silica surface in process water and simulated process water (surface inclination = 60° and $T = 50^\circ$ C).

5.4.5 Effect of calcium

Calcium has special place in mineral processing research. Yang et al. (2001) showed that bubbles at moderate and high pH have negative zeta potential. Bitumen surface has also a negative zeta potential, leading to a repulsive force between bubbles and bitumen surfaces. Addition of calcium or any other metal ions, leads to a reduction of repulsive force. Reduction of resistant force causes attractive forces to overcome these repulsive forces. Double layer compression also leads to a reduction of the induction time, as confirmed in recent studies (Gu et al., 2003, 2004).

In this study, the effect of calcium on terminal and sliding velocity is investigated. The results in Figure 5.10 show a negligible effect of calcium addition on the terminal and the sliding velocities. This finding is in agreement with the proposed model.

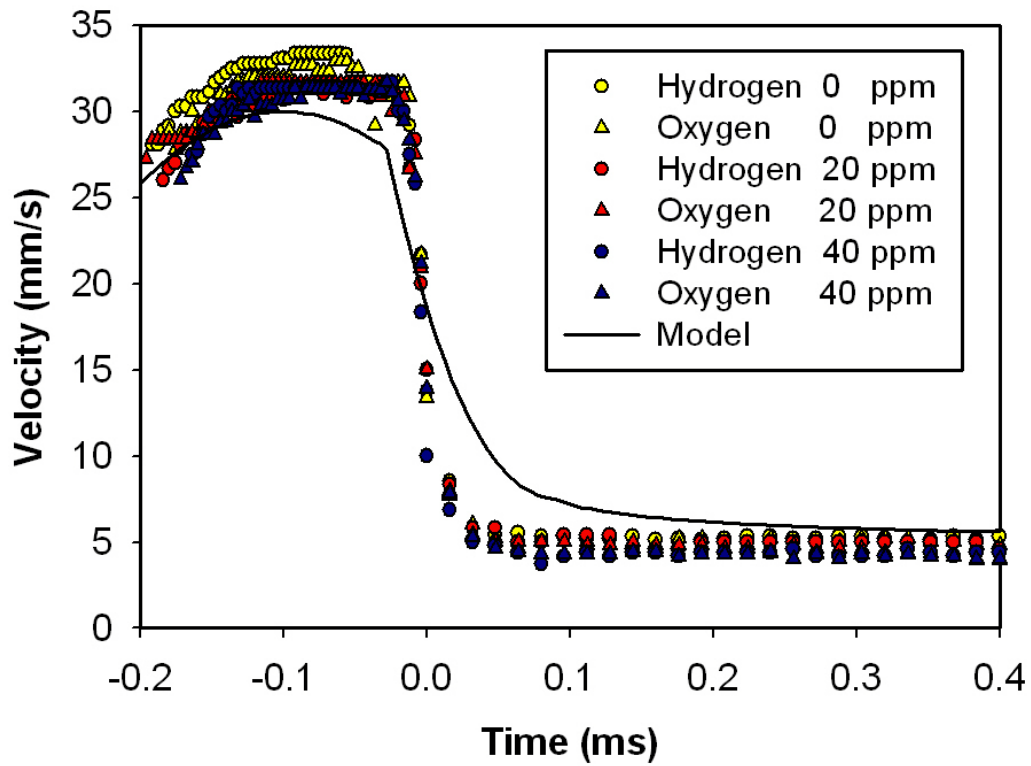


Figure 5.10 Effect of calcium addition on oxygen and hydrogen bubble rising and sliding velocities ($D = 0.25$ mm) against silica surface in process water and simulated process water with surface inclination = 30° and $T = 50^\circ\text{C}$.

5.4.6 Effect of surface wettability

Surface wettability is an important parameter in flotation studies. Surface forces are a determining factor in force balance and film stability before a film rupture.

Experiments were designed to investigate whether the sliding velocity is affected by the surface wettability. In this regard, two different surfaces, hydrophilic silica and hydrophobic bitumen were used. Sliding velocities of the bubble were compared for both surfaces. Our results show that, surface hydrophobicity has an impact on liquid film depletion and induction time as was discussed in Chapter 4. In Figure 5.11, the experimental results were compared with model prediction. In the proposed model surface forces were neglected, and it shows that there is no direct correlation between surface hydrophobicity and sliding velocity.

5.5 Conclusions

An analytical model was proposed to estimate sliding velocity of air bubble under an inclined surface. The results from the proposed model were compared with experimental data. As discussed in this chapter, there is agreement between model estimation and experimental results. There is potential to improve the proposed model in future, but it can be accepted as first step stone to develop an analytical model for sliding velocity estimation.

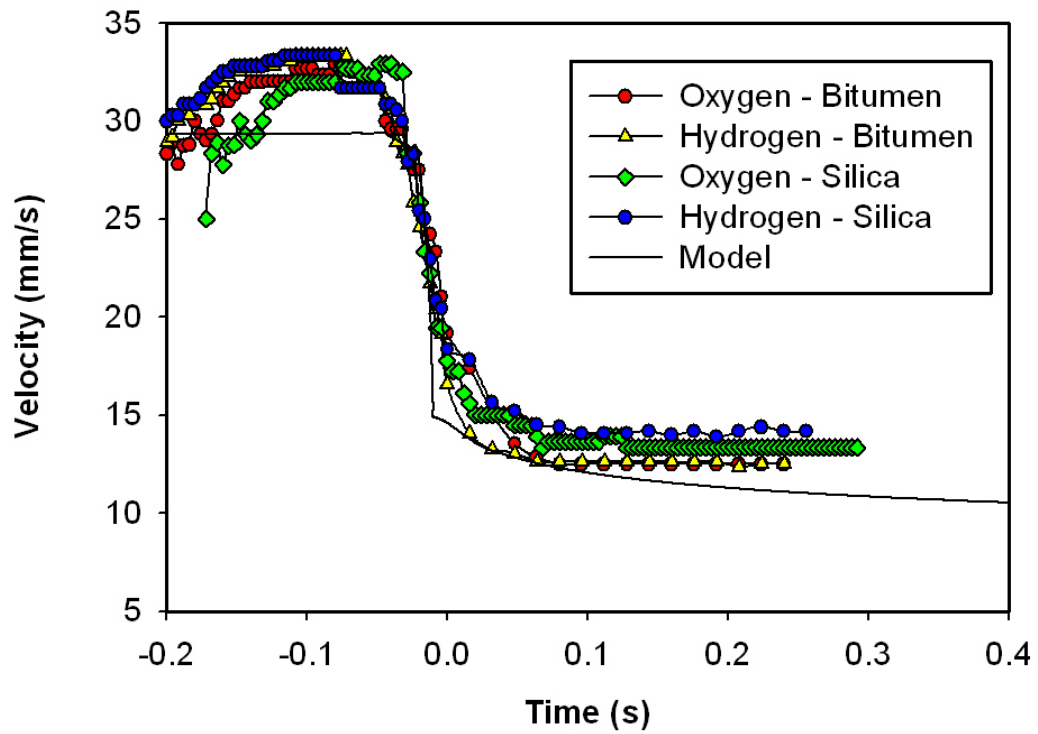


Figure 5.11 Effect of surface wettability on the bubble sliding velocity ($D = 0.25 \text{ mm}$) towards silica and bitumen layer surface in process water with surface inclination = 60° and $T = 50^\circ \text{C}$.

CHAPTER 6: A NOVEL METHOD OF MEASURING ELECTROPHORETIC MOBILITY OF GAS BUBBLES³

6.1 Introduction

Gas bubbles dispersed in aqueous media carry a surface charge, whose value depends on solution chemistry. The most common approach for determining a bubble surface charge is through electrophoretic mobility measurements, from which zeta potential values are calculated (Okada and Akagi, 1987; Saulinier et al., 1998; Graciaa et al., 1995; Li and Somasundaran, 1992; Sherwood, 1986; Kubota et al., 1983). The main source of error in electrophoretic mobility studies arises from the high rise velocities of the bubbles in a gravitational field. The problem is especially severe for large (i.e. microns-sized) bubbles as the bubble rise velocities are much higher than velocities due to electrophoresis. Researchers have attempted to devise techniques to either generate smaller bubbles to reduce the rising velocity of bubbles or to somehow minimize the effects of buoyancy during electrophoretic mobility measurements. For example, Sherwood (1986) used a rotating cell to counteract buoyancy effects with centrifugal forces. In this approach, the bubble was kept in the center of a cylindrical rotating cell and was free to move along the cell axis in response to an applied electric field. The measured electrophoretic mobility of the bubble was corrected for the Taylor column effect

³ A version of this chapter has been published. Seyyed Najafi A., Drelich J., Yeung A., Xu Z., and Masliyah J., 2007, A novel method of measuring electrophoretic mobility of gas bubbles, *Journal of Colloid and Interface Science*, 308, 2, 344-350.

(centrifugal force effect). Li and Somasundaran (1992) used a Buchner funnel connected to a glass frit with pores 2–2.5 μm in diameter to generate small bubbles. A peristaltic pump was used to keep the bubble-in-water dispersion in circulation and thus prevent bubble from rise and coalescence. Periodically, a sample of the dispersion was drawn into an observation cell for electrophoretic mobility measurement. Yang et al. (2003) moved the camera at the same speed as the velocity of rising bubbles to trace the bubbles vertically. The horizontal velocity of the bubble, which is due to an applied electric field, was used to calculate the zeta potential with high precision. Despite the remarkable accuracy of the above-mentioned methods, those experiments are very difficult to carry out and often require much practice and experimental skills.

Kubota et al. (1983) and Okada and Akagi (1987) used an interesting approach to generate small bubbles in surfactant solutions and measured their electrophoretic mobility. In their case, air was dissolved in three aqueous solutions, each containing a different type of surfactant (sodium dodecylbenzenesulfonate, sodium dodecylsulfate, and cetylpyridium chloride) under high pressure (~ 5 atm). When the air-saturated solution was exposed to atmospheric pressure, air bubbles nucleated in the solution. Larger bubbles were allowed to float to the top while the small bubbles (micron size) formed a dispersion that remained stable for several hours. The dispersion formed as such was introduced into a conventional electrophoresis cell and the velocities of the bubbles were measured at

the stationary plane. Zeta potentials were calculated from electrophoretic mobilities using the Smoluchowski equation (see Subchapter 6.4, p. 131) and trends for zeta potential versus concentration and type of surfactants were determined. Takahashi (2005) introduced another method for zeta potential measurements. This method for bubble generation was similar to the one used by Li and Sumasundaran (1992) except that the vertically positioned electrophoresis cell and graphic data processing method were used to obtain zeta potential values. The effect of neutral alcohol on bubble zeta potential is one of the interesting aspects of Takahashi's study (2005). More recently, Kim et al. (2005) used an ultrasonic dismemberator and palladium electrode to generate nano-sized bubbles. The authors reported that bubble dispersion produced in their study was of sufficient stability to conduct electrophoretic mobility measurements.

In this study, we follow the concept of nucleating nano-bubbles in solutions saturated with gas to produce bubble dispersions. Our approach is different from those proposed in the past (Okada and Akagi, 1987; Saulinier et al., 1998; Graciaa et al., 1995; Li and Somasundaran, 1992; Sherwood, 1986; Kubota et al., 1983) as it relies on changes in temperature, rather than changes in pressure, to initiate bubble nucleation. Generating bubbles by temperature control allows us to generate sufficient number of bubbles for the measurements. The nano-bubbles generated in the aqueous phase can remain dispersed for sufficient duration (several minutes) to allow for reproducible zeta potential measurements.

6.2 Novel approach for generation of small air bubbles

In this study, a simple and reliable method is proposed to generate dispersions of gas nano-bubbles, for which electrophoretic mobility can be measured using conventional means. Preparation of dispersion is based on the concept of bubble nucleation in a gas-supersaturated solution. The method is similar to the approach by Kubota et al. (1983) and Okada and Akagi (1987) in the sense that gas bubbles are nucleated in gas-saturated aqueous solutions. The nucleation of bubbles, however, is controlled here by temperature rather than pressure. Without the need for high pressure equipment, this method of preparing gas bubble dispersions is much easier to adopt in the laboratory and has better control for desired number of bubbles.

Gas Dissolution in Liquid

The effects of temperature on the dissolution of gases in liquids have been studied for many years. Several empirical equations are available for determination of gas concentration in liquids (Hamme and Emerson, 2004; Garcia and Gordon, 1992; Eaton and Franson, 2005). As an example, I analyze here the dissolution of air in water.

Air is composed of several different gases, including nitrogen, oxygen, argon, carbon dioxide and others. The relative amount of gases in air is shown in Table 6.1. Because oxygen and nitrogen are the dominant components of air, their dissolution in liquids is more often analyzed than for other gases.

Table 6.1 Composition of air (Eaton and Franson, 2005).

Component	Symbol	Volume (%)
Nitrogen	N ₂	78.08%
Oxygen	O ₂	20.95%
Argon	Ar	0.94%
Other Gases		0.03%

The dissolution of oxygen in water obeys Henry's law with the dissolved amount roughly proportional to the partial pressure of oxygen in air; i.e:

$$p_{O_2} = K_{O_2} \cdot x_{O_2} \quad (6-1),$$

where p_{O_2} is the partial pressure of oxygen in air, x_{O_2} is the mole fraction of O₂ in oxygen-saturated water, and K_{O_2} (T) is the Henry's constant for oxygen in water.

Although Henry's law is important in the analysis of gas solubility in liquids, it does not describe the effect of temperature on solubility of gas molecules, at least not directly. Many empirical equations are now available in the literature to estimate the solubility of oxygen in liquids as a function of temperature, pressure, and humidity (Hamme and Emerson, 2004; Garcia and Gordon, 1992; Eaton and Franson, 2005). Here, I present only a few of such equations.

The concentration of oxygen in air-saturated water can be determined from the following empirical equations (Garcia and Gordon, 1992):

i) for $0^{\circ}\text{C} < T < 30^{\circ}\text{C}$

$$C_{O_2} = \frac{0.678(P - p)}{35 + T} \quad (6-2)$$

ii) for $30^{\circ}\text{C} < T < 50^{\circ}\text{C}$

$$C_{O_2} = \frac{0.827(P - p)}{49 + T} \quad (6-3),$$

where C_{O_2} is the concentration of oxygen in water (mg O_2/L), P is the barometric pressure (Torr, 1Torr=133.32 Pa), p is the vapour pressure of water (Torr), and T is the temperature ($^{\circ}\text{C}$).

The concentration of nitrogen, neon and argon in aqueous salt solutions under atmospheric pressure can be calculated from the empirical correlation introduced by Garcia and Gordon (1992):

$$\ln(C) = A_0 + A_1T_s + A_2T_s^2 + A_3T_s^3 + S(B_0 + B_1T_s + B_2T_s^2) \quad (6-4),$$

where $T_s = \ln\left(\frac{298.15 - T}{273.15 + T}\right)$

In the above expression, C is the gas concentration in the water at atmospheric pressure (nmol/kg for Ne and $\mu\text{mol/kg}$ for N_2 and Ar), T is the temperature ($^{\circ}\text{C}$). All coefficients are listed in Table 6.2 and definition of salinity S (PSS, Practical Salinity Scale) is provided in Garcia and Gordon (1992).

Table 6.2 Coefficients for the calculation of Ne, N₂ and Ar solubility from Equation (6-4) (Garcia and Gordon, 1992).

Coefficient	Ne (nmol/kg)	N ₂ (μmol/kg)	Ar (μmol/kg)
A ₀	2.18156	6.42931	2.79150
A ₁	1.29108	2.92704	3.17609
A ₂	2.12504	4.32531	4.13116
A ₃	0	4.69149	4.90379
B ₀	-5.95737×10 ⁻³	-7.44129×10 ⁻³	-6.96233×10 ⁻³
B ₁	-5.13896×10 ⁻³	-8.02566×10 ⁻³	-7.66670×10 ⁻³
B ₂	0	-1.46775×10 ⁻²	-1.16888×10 ⁻²

Figure 6.1 shows the concentrations of oxygen, nitrogen and air in gas-saturated water at temperatures ranging from 0 to 50 °C calculated using Equations (6-2) to (6-4). As shown, the dissolution of all three gases increases with reducing the temperature of water.

Generation of nano-bubbles

A liquid can easily be saturated with a gas by bubbling the gas through the liquid for a prolonged period at a given temperature. To generate nano-bubbles, the temperature of the gas-saturated liquid can be rapidly increased. A sudden increase in temperature disturbs the solubility equilibrium and results in nucleation of gas nano-bubbles, forming a gas

dispersion. The volume of gas released for a temperature rise of 15°C is indicated in Figure 6.1.

Rapid increase in the temperature of the gas-saturated liquid facilitates the formation of gas bubbles. Spontaneous formation of nucleus (bubble embryo) begins with creation of cavities in the liquid due to thermal fluctuations of water molecules (Neimark and Vishnyakov, 2005; McGraw and Wu, 2003). Thermal fluctuation causes not only cavity creation, but also provides sufficient energy for developing a gas-liquid interface (Neimark and Vishnyakov, 2005; McGraw and Wu, 2003).

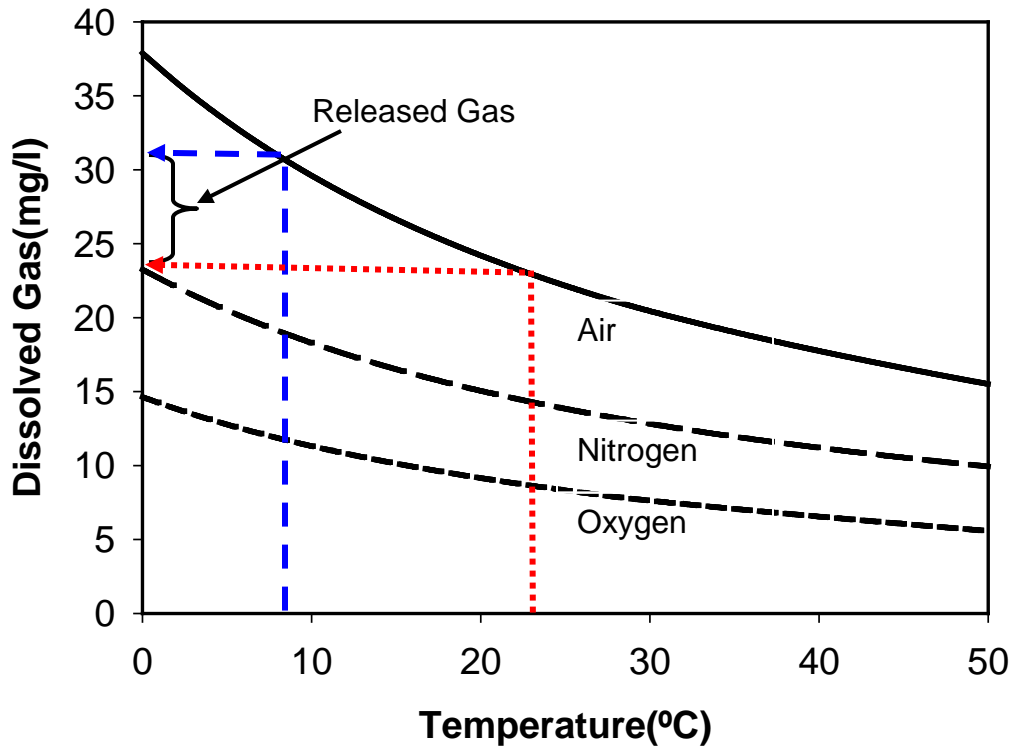


Figure 6.1 Effect of temperature on concentration of dissolved oxygen, nitrogen, and air in water. An increase in temperature of gas-saturated water disturbs the equilibrium of dissolved gas molecules, which can cause release of the gas. The lines marked on the graph show the amount of air that can be released from water if its temperature increases abruptly from 8 °C to 23 °C.

6.3 Experimental procedure

Liquids Used

All experiments are performed with two different liquids: a well - controlled laboratory aqueous solution is used to reproduce and compare the results of this study with previously published data, while measurement using industrial process water from oil sands industry allows us to study the effect of natural surfactant in process water on bubble charges.

The laboratory solution is prepared using ultra pure water (Millipore, 0.2 $\mu\text{S/cm}$) with added electrolytes and surfactants. NaCl, $\text{Al}_2(\text{SO}_4)_3$, and CaCl_2 , all of 99% purity from Fisher Scientific, were used as the electrolytes. Sodium dodecyl sulfate (ACROS organic; MW = 288.38) and dodecyl amine hydrochloride (Fisher scientific; MW = 221.81) were used to prepare surfactant solutions. NaOH and HCl were added to adjust pH of the aqueous solutions.

Industrial process water was obtained from Syncrude Canada's Aurora plant (April 2006 batch). This water was used in the extraction of bitumen (an extra heavy crude oil) from the Athabasca oil sands (Masliyah et al., 2004). Composition of the industrial process water is shown in Table 4.1.

To mimic industrial process water, "simulated process water" was prepared from ultra pure (Millipore) water. The added salts are listed in Table 4.2 and the resulting ionic concentrations are close to those in the industrial process water. pH of the simulated process water was adjusted

to 8.1. In order to evaluate the effect of calcium present in the industrial process water, further addition of calcium chloride was made. The pH of the resulting solution was adjusted to 8.15 by bubbling CO₂ through the solution. The simulated process water was used in this study as a reference to the industrial plant process water to illustrate the role of surface active species normally present in the industrial process water. One should note that the industrial process water contains dissolved natural surfactants, originally extracted from the bitumen during oil sands processing. These surfactants would not be present in the simulated process water. Use of simulated water allowed controlled investigations on the effect of surfactants present in the industrial process water on bubble zeta potential.

In another series of experiments, the industrial process water was fractionated into “foam” and “residual” components. During the fractionation process, nitrogen was sparged through the process water. This causes the natural surfactants to adsorb onto the nitrogen bubbles and be transported to the foam, leaving the residual water at the bottom of the column containing less surfactants.

A schematic of the fractionation column is shown in Figure 6.2. It consists of the following major parts: (i) gas distributor made of porous fritted glass having pores of 2 - 2.5 μm in diameter at the bottom of the column, (ii) outlet valves located over the entire height of the column to collect samples of fractionated foam (only valves used in this study are shown in

the schematic), (iii) inlet for the process water, and (iv) gas inlet at the bottom of the column.

A volume of 1.3 L filtered industrial process water was poured into the column and fractionated for 30 min by bubbling nitrogen at a flow rate of roughly 64 L/min. This yielded approximately 450 mL of foam, 650 mL of residual water, and 200 mL of an intermediate fraction. In this study, the intermediate fraction was not used for zeta potential measurements.

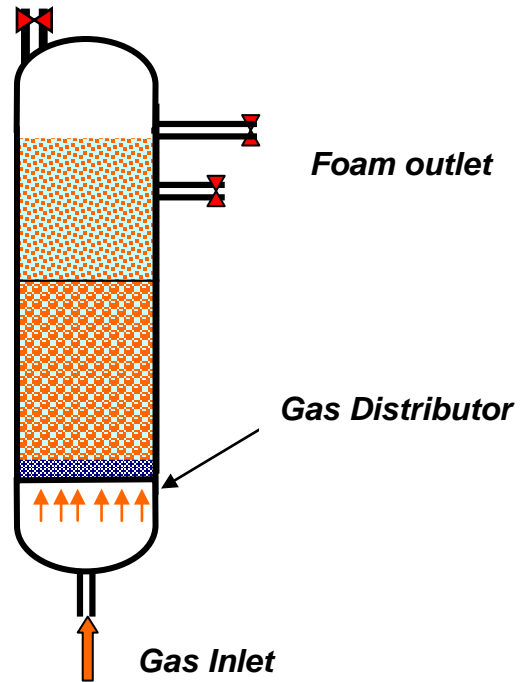


Figure 6.2 Schematic of the column used in fractionation of the industrial process water.

Preparation of nano-bubble dispersions

The aqueous solutions were gas saturated at low temperature by purging a gas of interest from a cylinder into the solution for 24 hours at 8°C. To prevent contamination with micro organisms and bacteria, both the gas and the aqueous solutions were filtered through Millipore bacterial filter (pore size 0.1 µm).

Air-saturated solutions having a temperature of 8°C were rapidly heated to 23°C using the temperature control circuit installed inside the Brookhaven ZetaPALS instrument (Figure 6.3). As shown in Figure 6.1, a fifteen-degree rise in temperature causes an imbalance in the two-phase system. Less gas is dissolved in the liquid at the higher temperature. As a result, nano-bubbles are nucleated in the heated aqueous phase. The bubbles grow to a larger size over time. Formation of bubbles in the liquid is easy to detect through the Tyndall effect. Figure 6.4 shows a laser beam passing through the cuvette filled with air-saturated water before (a) and after (b) an increase in the temperature. The path of the laser beam is clearly observed in the warmer water as a result of light scattered from the bubbles.

The size of nano-bubbles was measured by a dynamic light scattering method based on the particle size option in the ZetaPALS instrument. The scattered intensity was set at a scattering angle of 90° and the temperature of 296.15 K. The average size of nano-bubbles was measured as 290 nm.

6.4 Zeta potential measurements

Electrophoretic mobilities (U/E) of bubbles were measured using ZetaPALS instrument (Brookhaven Instruments) equipped with Uzgiris Brookhaven electrodes coated with palladium and He-Ne laser as a light source. A gas-saturated liquid was poured into the cell of the instrument. As is shown by the schematic in Figure 6.3, the temperature of the sample was adjusted inside the instrument using an internal temperature-controlling system. Soon after the increase in the liquid temperature, an electric field was applied to the cell and the electrophoretic mobility of the generated nano-bubbles was measured by phase analysis of light scattering technique. A modified Smoluchowski equation was assumed to apply to the bubbles and was used to calculate zeta potential (ζ) from experimental mobility:

$$\mu = \frac{U}{E} = \frac{\varepsilon_o \varepsilon_w \zeta}{\eta} G(\kappa a, \alpha_b) \quad (6-5)$$

where μ is the electrophoretic mobility, U is the electrophoretic velocity of the bubbles, E is the electric field strength, ε_o is the permittivity of free space (8.854×10^{-12} J/(V²m)), ε_w is the relative permittivity of the electrolyte solution, and η is the liquid viscosity (0.948×10^{-3} Pa.s at 23 °C). $G(\kappa a, \alpha_b)$ is a function accounting for the concentration of dispersed phases. Here α_b , is the volume fraction of the gas dispersion, κ^{-1} is the Debye length and a is the gas bubble radius (Masliyah and Bhattacharjee,

2006). Function G is nearly unity for $\kappa a > 100$ and α_b as high as 0.3. In our case, the lowest value of κa was 1.6. However, with small bubble volume, fraction of $\alpha_b = 0.006$, giving rise to a G value of nearly unity. Consequently, no correction is required to Smoluchowski equation, which is written as:

$$\mu = \frac{U}{E} = \frac{\varepsilon_o \varepsilon_w \zeta}{\eta} \quad (6-6)$$

Each zeta potential value reported in this chapter is the mean value calculated from 100 measurements; ten measurements for ten different samples. The mean and standard deviation of zeta potential were calculated by assuming a log-normal distribution of the generated data.

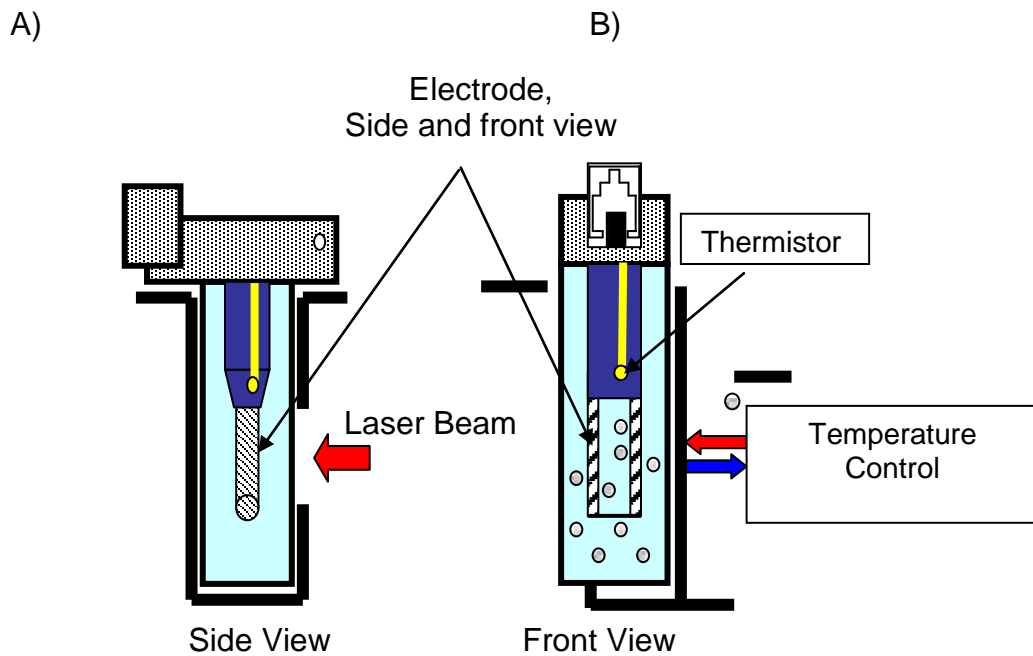


Figure 6.3 Schematic of a cell with the Uzgiris electrode of the Brookhaven ZetaPALS instrument equipped with a temperature control system. A) before heating (no nano-bubble) and B) after heating, (with nano-bubbles nucleated in the form of a dispersion).

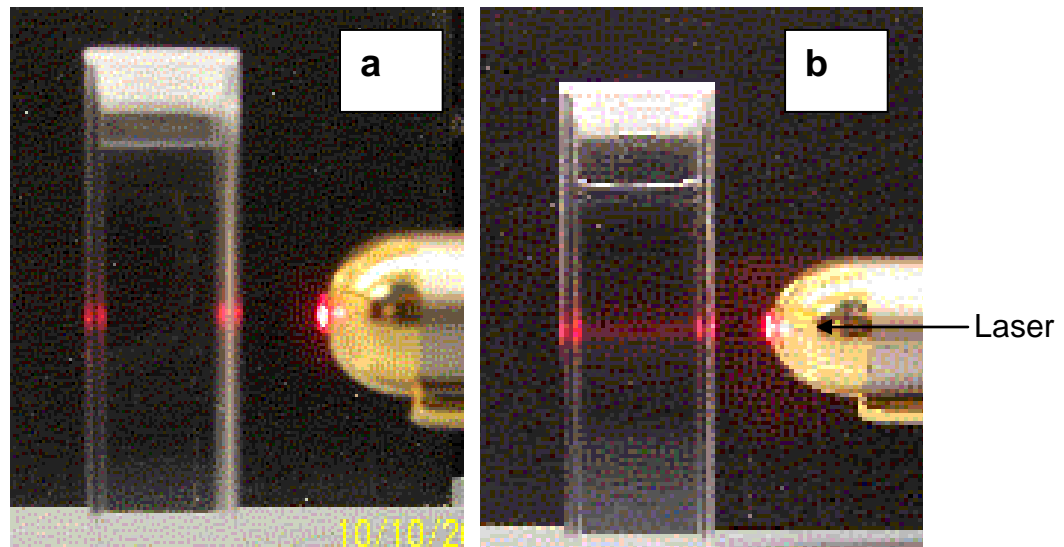


Figure 6.4 Two photographs with a laser beam passing through the cuvette filled with the air-saturated water: a) temperature of water as saturated at 8 °C, b) temperature of air-saturated water raised to 23 °C. A scattered beam is observed on photograph (b) due to Tyndall effect caused by nucleated bubbles dispersed in water.

6.5 Results and discussions

6.5.1 Effect of pH on zeta potential of air bubbles

For studying the effect of pH, a solution of 0.01 M NaCl was used and the pH was adjusted with either NaOH or HCl. A similar solution was used by Li and Somasundaran (1992) and Yang et al. (2003), allowing for a comparison of air bubbles zeta potential values measured with three different techniques.

Results of zeta potentials for air bubbles are shown in Figure 6.5. The bubbles generated in a 0.01 M NaCl solution were negatively charged over a wide pH range with an isoelectric point located at pH 2.2 to 2.4. The negative charge on the air bubble surface is believed to be due to preferential adsorption of OH^- ions. According to the data by Conway (1975), the enthalpy of hydration (ΔH_h°) of H^+ and OH^- ions is -1104 and -446.8 kJ/mol, respectively. As a result, the H^+ ions preferentially remain in the bulk aqueous phase, leaving space at the gas-water interface for the OH^- ions. This effect is called “negative adsorption” or “exclusion” of protons from the interface. However, at low pH values, when the concentration of H^+ ions increases exponentially, H^+ ions adsorb at the gas-water interface due to increased chemical potential. The adsorption of the H^+ ions causes a reduction in the absolute value of the bubble zeta potential.

The absolute value of zeta potential increased with increasing pH, reaching a plateau of about 22 – 25 mV at pH ~ 8 (Figure 6.5). Our results show negligible increase in zeta potential value of air bubbles in alkaline solutions with pH > 8. The results obtained in this study closely overlap with those reported by Yang et al. (2003). Our zeta potential versus pH relationship is also very similar to that reported by Li and Somasundaran (1992), although the absolute zeta potential values from their study are higher by 5 – 10 mV at pH < 6 and more than 20 mV at pH > 6 (compared to our results and those reported in (Yang et al. 2003), as shown in Figure 6.5. This discrepancy could be due to differences in experimental techniques used.

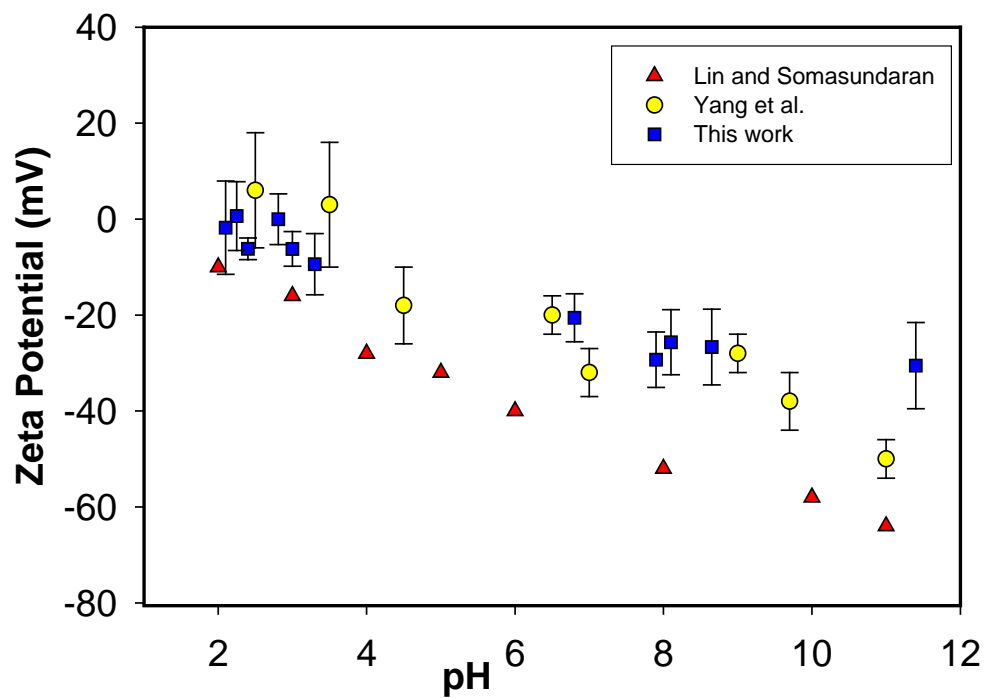


Figure 6.5 Variation with pH of zeta potential of air bubbles in 0.01 M NaCl solution.

6.5.2 Effect of electrolyte concentration

The effect of salt addition on air bubble zeta potential is evaluated in this section. Zeta potential of bubbles was measured in 0.0001 M sodium dodecyl sulfate (SDS) solution with different salt concentrations at pH 6.5. SDS was chosen to allow the comparison of the results with those reported in Okada and Akagi (1987). SDS solutions were first saturated with air. The salt was then dissolved in the SDS solution at concentrations ranging from 0.0007 M to 0.01 M NaCl, 0.0001 M to 0.01 M CaCl₂, and 0.00001 M to 0.01 M Al₂(SO₄)₃. The measured zeta potential values are shown in Figure 6.6 and they are compared with the data reported by Okada and Akagi (1987).

Comparison of the cases with and without SDS shows that the zeta potential of air bubbles is much more negative due to the adsorption of ionized SDS surfactant at the gas-water interface. Depending on the valency of cations and their concentrations in the solution, the dissolved cations of the inorganic salts reduce, neutralize, or even reverse the charge of the sulphate groups (Yoon and Yordan, 1986).

As shown in Figure 6.6, the magnitude of the bubble zeta potential decreases in solutions with increasing valency of added cations. For example, in the presence of 0.0001 M SDS, the zeta potential of air bubbles increases from about -80 mV in 0.001 M NaCl to -40 mV in 0.001 M CaCl₂, and reverses to +10 mV in 0.001 M Al₂(SO₄)₃ solutions.

Our results show the same trend for air bubble zeta potential in response to NaCl and CaCl₂ addition as reported by Okada and Akagi (1987), although the measured values in our case are smaller by 10 – 20 mV. In contrast to the results by Okada and Akagi, we observed negative surface charges for bubbles in 0.00001 to 0.001 M Al₂(SO₄)₃ solutions, which are neutralized to a zero value in ~0.001 M Al₂(SO₄)₃ solution and then change to positive surface charges at higher Al₂(SO₄)₃ concentrations.

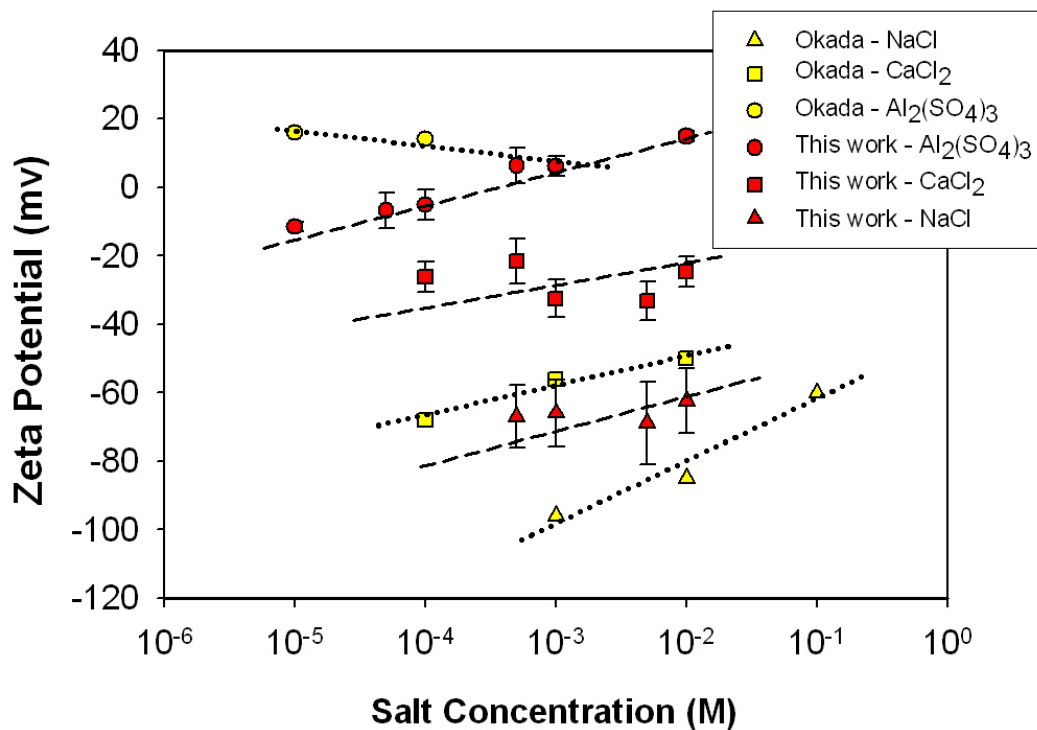


Figure 6.6 Zeta potential of air bubbles dispersed in 0.0001 M SDS solution of (pH = 6.5) with dissolved salts of varying concentrations.

6.5.3 Effect of Surfactant Concentration

To further illustrate the feasibility of our technique to study the effect of surfactant addition on zeta potential of air bubbles, SDS and DAH (Dodecylamine hydrochloride) were used as the surfactants of interest in our test. The results are shown in Figures 6.7 to 6.9.

The surface charge of air bubbles in surfactant solutions is strongly dependent on the type of surfactant and its ionization properties. It is negative in solutions of anionic surfactants and positive in cationic surfactant solutions, as long as the dissolved surfactants form ionic species.

As discussed, air bubbles in pure water are negatively charged due to excess OH^- groups at the interface. Because SDS is an anionic surfactant which adsorbs also at the interface (Eaton and Franson, 2005; Usui and sasaki, 1970), the bubbles can only be more negatively charged in SDS solutions. As noted in Figure 6.7, the zeta potential of bubbles decreased from about -40 mV in 10^{-5} M SDS solution to -84 mV in 7×10^{-3} M SDS solution. As the concentration of surfactant increases, the slope of the zeta potential charge decreases with increasing SDS concentration. This effect is expected and can be explained by progressive adsorption of SDS molecules at the air-water interface and saturation of surfactant adsorption, forming a monolayer. The SDS monolayer reaches a maximum surface concentration at the critical micelle concentration

(0.0083 M for SDS) and any further increase in the SDS bulk concentration will not affect the number of surfactant molecules adsorbed at the gas bubble surface. The correlation between zeta potential of the bubbles and SDS concentration observed in this study is in good agreement with the results reported by Okada and Akagi (1987), and Yoon and Yordan (1986), further confirming that our technique is suitable for bubble generation and subsequent zeta potential measurement.

Since ionic surfactants ionize at only certain pH values, the zeta potential of air bubbles depends on the solution pH. The effect of pH on the zeta potential of air bubbles in 0.001 M solutions of SDS and DAH is shown in Figures 6.8 and 6.9, respectively. The two surfactants used in the experiments, SDS and DAH, behaved differently in alkaline and acidic solutions. As shown in Figure 6.8, the zeta potential of air bubbles remained practically constant at -55 mV in 1 mM SDS solution at pH ranging from 4 to 10. The air bubble zeta potential is noted to become less negative at $\text{pH} < 3$. This increase is attributed to hydrolysis of SDS. According to Leja (1982), alkylsulfates are hydrolyzed to produce alcohol and bisulfate at pH below 3. Alkylalcohol also adsorbs at the gas-water interface but because of its non-ionic nature, it does not bring any charges to the gas bubble surface. As a result, the negative charge of the air bubble with adsorbed alcohol is less negative than that with adsorbed alkylsulfate.

In contrast to SDS, DAH hydrolyzes at a higher pH (Yoon and Yordan, 1986; Ananthapadmanabhan and Somasundaran, 1980) and precipitates. As a result, the zeta potential of bubbles decreases and reverses to become more negative with increasing pH above 9 as shown in Figure 6.9.

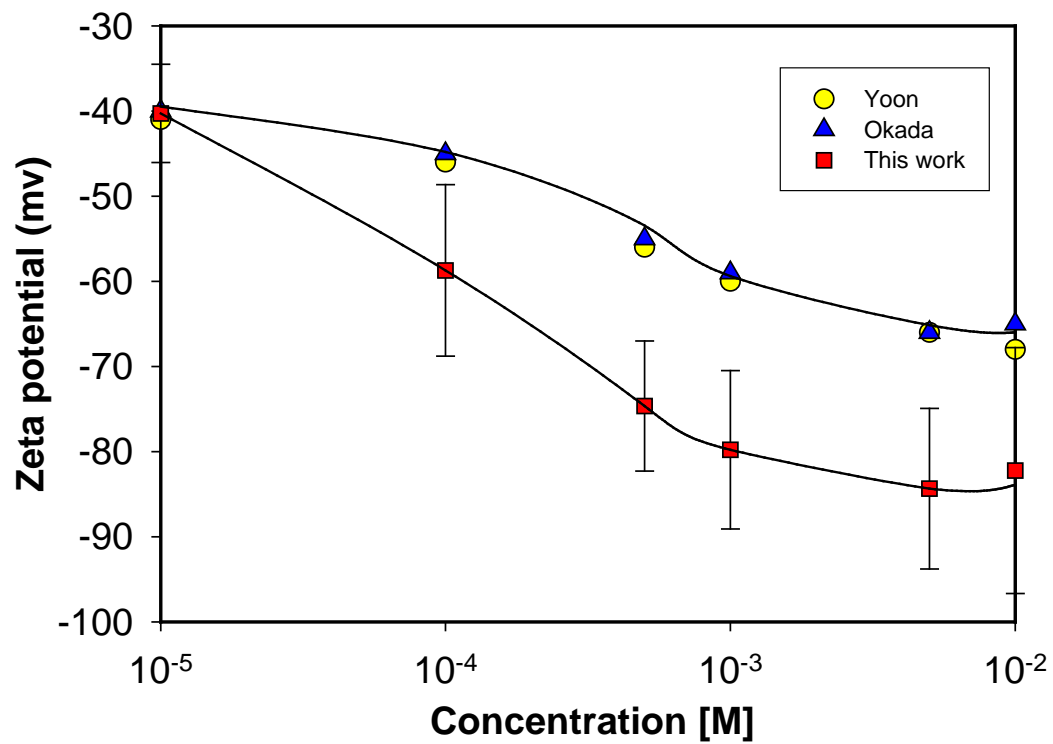


Figure 6.7 Zeta potential of air bubbles in SDS at pH = 7.0.

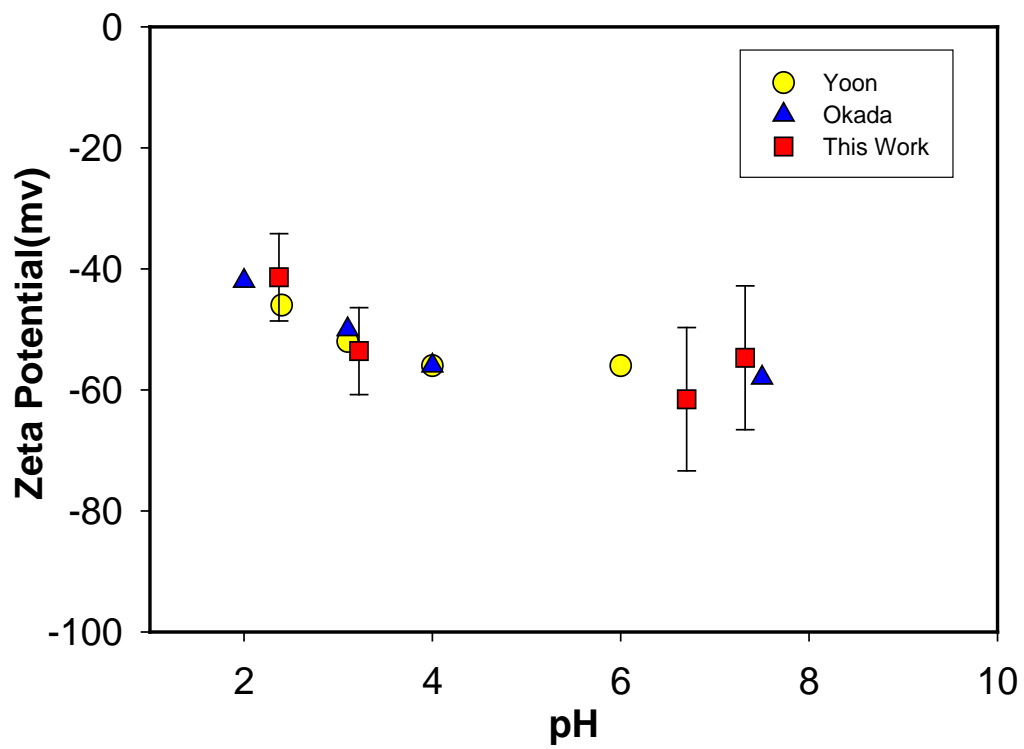


Figure 6.8 Effect of pH on zeta potential of air bubbles in 0.001 M solutions of SDS.

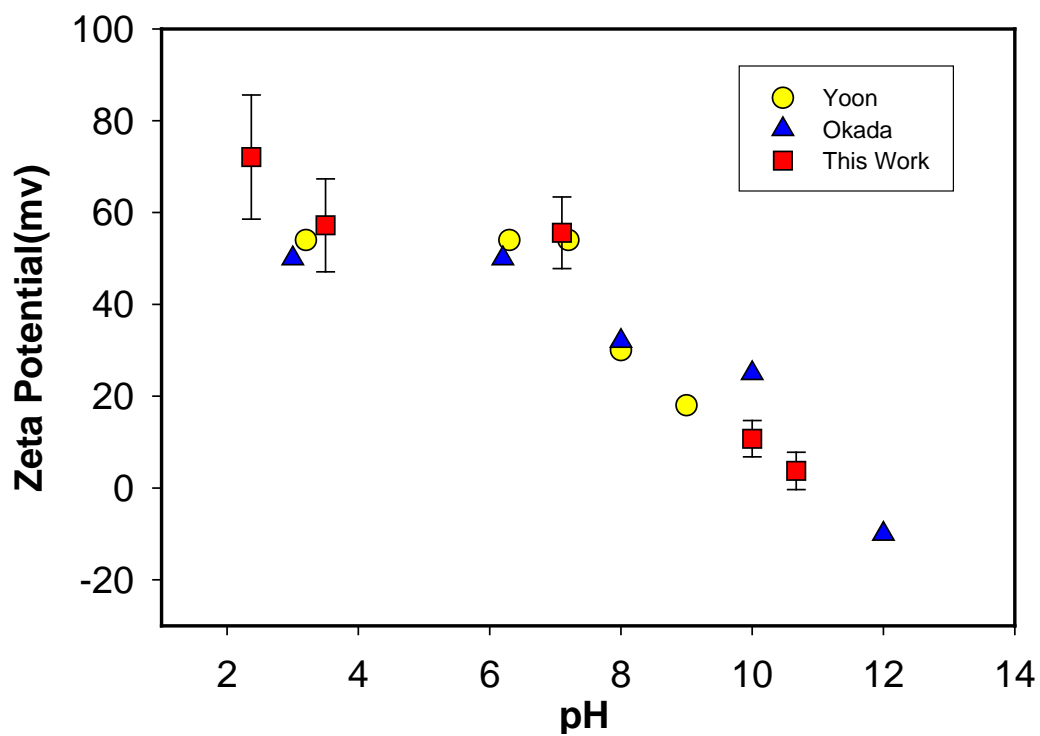


Figure 6.9 The effect of pH on zeta potential of air bubbles in 0.001 M DAH solutions.

6.5.4 Zeta potential of bubbles in industrial process water

As an example of applications, this part of the study relates to our interest in the surface charge of air bubbles dispersed in an industrial process water. The water is used in extraction of bitumen from the Athabasca oil sands (Masliyah et al., 2004). The electric charge of air bubbles is known to influence the kinetics and efficiency of bitumen flotation. The surface charge of air bubbles can be affected by both the dissolved ions and natural surfactants in the process water.

In this study, I measured the zeta potential of air bubbles nucleated in industrial process water, as well as in the simulated process water, which contains electrolytes similar to those found in the industrial process water — but without the natural surfactants. In studying the effect of natural surfactants on zeta potential of air bubbles, I also performed a series of measurements of bubble zeta potential in foam and residual water, fractionated from the industrial process water. Foam is rich in natural surfactants, whereas the residual solution, by and large, has depleted amounts of natural surfactants, as compared with both, the process water and its foam fraction. As discussed by Gu et al. (2002), there are three major types of water soluble anionic surfactants extracted from bitumen under alkaline condition. They are carboxylates, sulphates, and sulphonates.

As gypsum and calcium-based salts are part of the mineralogical components of oil sands, and calcium ions are frequently added to tailings to flocculate fine solids, the effect of added calcium in industrial process water on the process was investigated (Masliyah et al., 2004; Basu et al., 2004; Liu et al., 2005; Kasango et al., 2000). In this study, we also added calcium ions to the solutions to explore the effect of calcium chloride on zeta potential of air bubbles in the process water.

Figure 6.10 shows the results of zeta potential measurements for air bubbles nucleated and dispersed in industrial and simulated process waters, as well as in the two fractions of the process water. The pH in all cases was between 8.0 and 8.3. The effect of added calcium chloride to a given solution is negligible. The zeta potential of the bubbles in the foam water is of the most negative value, followed by the industrial process water. Both, the fractionated residual water and simulated water, gave similar zeta potential values. These findings suggest the presence of anionic surfactants in process water. Their effect on the charge of air bubbles and hence on bitumen–air bubble attachment should not be overlooked while investigating the effect of water chemistry on bitumen extraction.

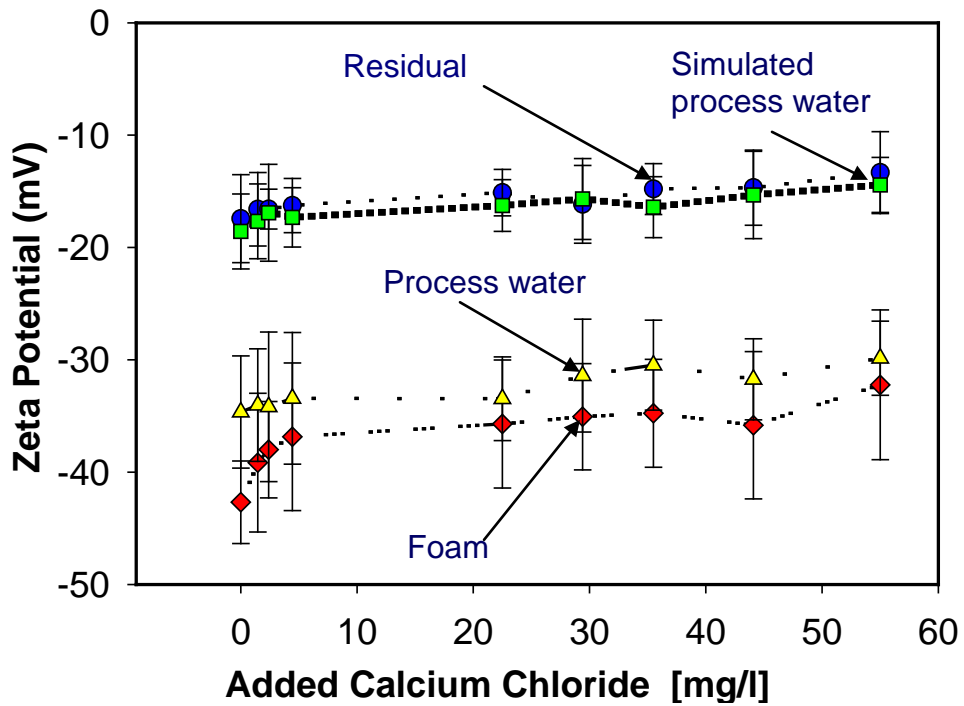


Figure 6.10 Zeta potential of air bubbles in industrial process water, its foam and residual fractions, and simulated process water with increasing concentration of CaCl_2 . pH of solution was adjusted by CO_2 gas to $\text{pH } 8.15 \pm 0.10$.

6.6 Conclusions

A simple and reliable method of generating stable dispersions of nano-bubbles was reported in this study. Preparation of gas-in-water dispersions relies on nano-bubble nucleation in gas-supersaturated solutions by manipulating the temperature and hence gas saturation. Bubbles generated by this convenient method are suitable for study of bubble electrokinetics.

Electrophoretic mobilities of air bubbles determined in this study agree with reported values. It is confirmed that the electrokinetics of air bubbles affected by the presence of electrolytes, solution pH and surfactants. The natural surfactants in the process water had a pronounced effect on electrokinetic of air bubbles. Bubbles are highly negatively charged in industry process water of oil sands extraction.

CHAPTER 7: EFFECT OF COLLOIDAL FORCES ON BUBBLE AND SOLID INTERACTIONS

7.1 Colloidal surface forces

An intervening liquid film forms as a bubble approaches to a solid collector surface. Stability of this liquid film is a vital factor for flotation process. It is a determining factor for bubble-particle attachment. It is known that liquid film between a hydrophilic particle and an air bubble is stable. The instability of a liquid film between a hydrophobic particle and an air bubble leads to rupture of the thin film and attachment of the air bubble to particle. The film stability is quantified by determining disjoining pressure and surface forces which change with film thickness.

The cumulative interactions between atoms, ions or molecules of two interacting bodies result in disjoining pressure and force between two bodies. This force is strongly dependent on the separation distance. In addition to separation distance this force is dependent on shape and geometry of the bodies.

This net force is believed to include components with different origins, which are independent. The most known components are:

- Electrodynamic or van der Waals interactions
- Electrostatic double layer interaction
- Non-DLVO interactions

The first two components are well established and known as DLVO forces. The major non-DLVO forces considered between a bubble-particle pair are hydration forces, hydrophobic forces, structural forces and steric forces.

7.1.1 van der Waals interaction

The universal attractive force between atoms and molecules, known as van der Waals forces, also operates between macroscopic objects. The van der Waals dispersion forces are usually studied in a quantum mechanics frame work and there are many theories to describe them. The displacement of electrons around nuclei generates an instantaneous dipole, from which the resultant electric field affects neighbouring atoms and molecules, and polarizes them. The interaction between two dipoles results in an attractive force between two atoms. In an integral form the same principle applies to surfaces and particles of macro scales. van der Waals force is an important force, which plays a role in bubble-solid interactions (Usui and Barouch, 1990).

There are two approaches to calculate van der Waals forces, The first approach is based on Hamaker (Israelachvili, 1985) who developed the theory of van der Waals forces between two macroscopic bodies. This method is based on the assumption of pairwise additivity of all individual intermolecular interactions. The second method is the Lifshitz approach (Israelichivili, 1985), on the basis of continuum mechanics.

In principle, the complex Lifshitz approach enables van der Waals forces between any system of interest to be calculated. However, Lifshitz approach requires detailed knowledge of the dielectric constants and refractive indices of media over a wide range of frequency, which normally are not available.

Usually Hamaker constant, which is a material dependent, is determined by Lifshitz theory. In this way the two approaches are combined and it is the best approach to determine van der Waals interactions for a heterogeneous system.

For an undeformed bubble of radius R_b within a small separation gap h ($h \ll R_b$), from a flat surface, van der Waals interaction potential can be formulated as (Mahanty and Ninham 1976):

$$V_{VDW} = -\frac{A_{123} R_b}{6h} \quad (7-1)$$

where A_{123} is the Hamaker constant for the van der Waals interaction between phase 1 (spherical bubble) and phase 2 (flat plate) separated by medium 3 (liquid solution).

Equation (7-1) was derived by assuming infinite speed for the electromagnetic wave propagation. This is not a valid assumption for real system, where the electromagnetic field propagation is limited, which causes a reduced correlation between dipolar oscillations in the interacting bodies and hence a smaller van der Waals interaction. Such a reduction is

called retardation effect. It is easy to modify the simple Hamaker approach to take into account the retardation effect by introducing a “characteristic wave length” λ for the interaction that usually takes on a value of 100 nm (Gregory, 1981; Israelachvili, 1985). Therefore, the modification of van der Waals interaction between a sphere and a flat plate, with consideration of the retardation effect, is given by Suzuki et al. (1969):

$$V_{VDW} = -\frac{A_{123} R_b}{6h} \frac{\lambda}{(\lambda + 11.116h)} \quad (7-2)$$

or

$$F_{VDW} = -\frac{dV_{VDW}}{dh} = -\frac{A_{123} R_b}{6h^2} \frac{\lambda(\lambda + 22.232h)}{(\lambda + 11.116h)^2} \quad (7-3)$$

7.1.2 Electrostatic double layer (EDL) interaction

In addition to van der Waals interaction forces, the other type of colloidal forces included in the DLVO theory is due to electrostatic double layer (EDL), an interaction between two charged interfaces. Charged particles, depending on the type of charge they carry, can attract or repel each other according to Coulomb’s electrostatic interaction. However, whenever two charged particles placed in an aqueous medium, due to diffuse layer, calculation of forces interaction is complicated.

7.1.2.1 Electrical double layer force

When two particles approach each other in an aqueous medium, their electrical double layers overlap and consequently they exert forces to

each other. This force is known as electrical double layer force. This force is Coulombic interaction in nature. This force has important role in particle-bubble interaction in flotation.

The electrical double layer force is dependent on charging mechanism at the surface. In theory, three cases are considered: i) the surface potentials remain constant, ii) the surface charge density remains constant, or iii) surface charge density and potential change by charge regulation.

For bubble-particle interaction in flotation, the constant surface charge density assumption is more appropriate than others (Nguyen and Schulze, 2004).

The Poisson-Boltzmann equation is used for determining charge distribution around a particle. Because of its complex nature usually numerical methods are used to solve the equation. To simplify the discussion, analytical solutions are provided by some scientists for specific systems. For example, Debye-Huckel approximation is used for weakly charged surfaces. Derjaguin approximation is used when the distance between the particles is smaller than the size of the particles. The superposition approximation is used when particles are far apart. These approximations are used solely or in combination. The linear Debye-Huckel approximation is more convenient for modeling bubble particle interactions (Nguyen and Schulze, 2004).

7.1.2.2 Derjaguin approximation

Previous equations were derived for two parallel flat surfaces. For the case of forces between two particles with different geometry, Derjaguin approximation has been often used. Derjaguin (Israelachvili, 1991) and later White (1983) used a set of equations to evaluate interaction force F between different geometries based on interaction energy between two parallel flat surfaces and Derjaguin approximation.

The electric surface potential necessary for calculation of double layer interaction is substituted by zeta potential. Zeta potential of particles is measured by electrophoretic methods. Measuring the zeta potential of gas bubbles is more difficult and a novel technique for its evaluation was discussed in Chapter 6 (p. 124). Zeta potential of gas bubbles changes with changing solution properties, such as pH, surfactants or/and electrolyte concentrations. Consequently, electrical double layer force changes with system properties. For our case, we used HHF approximation (Hogg, Healy and Fuerstenau):

$$F_{EDL} = Dl\tau \left[\frac{\exp(-\kappa H)}{1 + \exp(-\kappa H)} - Da \frac{\exp(-2\kappa H)}{1 - \exp(-2\kappa H)} \right] \quad (7-4)$$

$$Dl = \frac{\varepsilon_0 \varepsilon_r a_p \zeta_c \zeta_p}{kT} \quad (Dl, \text{ double layer parameter}) \quad (7-5)$$

$$Da = \frac{(\zeta_c - \zeta_p)^2}{2\zeta_c \zeta_p} \quad (Da, \text{ double layer asymmetry parameter}) \quad (7-6)$$

7.2 Non- DLVO forces

DLVO (Derjaguin – Landau - Verwey - Overbeek) theory does not explain such observations as attachment of bubble to negatively charged (e.g. bitumen) surface. Existence of other forces was therefore suggested based on experimental data. Among these forces are: repulsive hydration force (Pashley, 1981a, b), attractive hydrophobic force (Israelachvili and Pashley, 1982), repulsive steric force and attractive bridge force (Ingersent et al., 1990). While nature of some of these forces remains to be elucidated, a combination of experimental data and empirical equations is used to calculate them.

7.2.1 Hydrophobic force

Classical DLVO theory does not elucidate the process of attachment of air bubble to hydrophobic solid particles. An extra attractive force is therefore necessary for bubble attachment. This force is classified as a long range attractive force between hydrophobic surfaces (Ben-Nain, 1980; Ralston, 2001).

Hydrophobic force F_{HB} is expressed in the form of van der Waal force:

$$\frac{F_{HB}}{R} = -\frac{K}{h^2} \quad (7-7),$$

where K is evaluated based on curve fitting of experimentally measured force profiles.

7.2.2 Hydration force

Hydration force is a repulsive force between hydrophilic surfaces. It was first reported by Israelachvili and Adams (1978).

7.2.3 Steric force

This force represents the effect of surface heterogeneity and roughness. Theories and experimental data were used collectively to evaluate this force (Israelachvili, 1991).

7.3 Classical DLVO and extended DLVO theory

The classical DLVO theory was used to describe colloidal interactions and includes van der Waals force F_{VDW} and electrostatic double layer force (Israelachvili, 1991). The DLVO theory can be expressed as:

$$F_{total} = F_{VDW} + F_{EDL} \quad (7-8)$$

When use of classical DLVO was not enough to describe phenomena like bubble-particle attachment, other forces were included in calculation, which is known now as “extended DLVO theory”:

$$F_{total} = F_{EDL} + F_{VDW} + F_{HB} + F_S + F_{HD} \dots \quad (7-9),$$

where F_{EDL} is electrostatic double layer force, F_{VDW} is van der Waals force, F_{HB} is hydrophobic force, F_S is steric force, and F_{HD} is hydration force.

The sign of the resultant surface force, F_{total} , determines whether a bubble is going to attach to a solid surface.

7.4 Induction time measurement and calculation

In present research, Equation (4-2) was used to calculate induction time. In order to have accurate induction time values, surface forces were added to the calculation in addition to gravitational forces. Calculated values were then compared to those measured. As it is difficult to report a unique experimental value for the induction time, an average of twenty experimental runs was reported as the measured induction time (Figure 7.1).

The numerical modeling of induction time by considering surface forces without experimental results in hand is a challenging task. In ordinary way of thinking, as bubble approaches to a solid surface, the surface force becomes more dominated compared to the gravitational driving force. DLVO forces are repulsive and are not in favor of bubble attachment to the solid surface. Therefore only hydrophobic force determines whether the liquid film ruptures and bubble attaches to the surface. The hydrophobic force coefficient K , should be determined experimentally. It is not possible to predict whether the bubble attaches to a surface or not without having prior experimental results.

In this part, we borrowed critical film thickness concept from Nguyen and Schulze (2004). The calculated time is the time necessary for liquid depletion from the initial thickness to the critical thickness. We assumed that after critical thickness the film rupture happens spontaneously and the time for film rupture is not included in the calculation. The calculation was

carried to study the effect of temperature on induction time. The calculated induction time is closer to the predicted values at higher temperatures than at lower temperatures. There are deviation between model and experimental measurement as temperature increases. It can be concluded that critical thickness is a function of temperature. In order to improve the model, it is necessary to develop and add a correlation between critical thickness and temperature to the model, which is a subject to the future proposed work (Chapter 8, p. 165).

In the calculations below, hydration and steric forces are ignored and following equation was used to calculate F at Equation (4-2):

$$F = F_{\text{Buoyancy}} + F_{\text{EDL}} + F_{\text{VDW}} + F_{\text{HB}} \quad (7-10).$$

For calculation of induction time, many of constants were borrowed from the literature. For this experiment, the methylated silica was used. Here, it is important to note, that the Hamaker constant and the surface potentials are not changed significantly by the methylation reaction for hydrophobization of silica surface (Laskowski and Kitchenere, 1969).

A_{132} is the Hamaker constant for the interactions with silica plate (1), air bubble (2), and water (3). This value can be obtained using the combining rule:

$$A_{132} = (\sqrt{A_{11}} - \sqrt{A_{33}})(\sqrt{A_{22}} - \sqrt{A_{33}}) \quad (7-11),$$

where A_{11} , A_{22} and A_{33} refer to the Hamaker constants of the silica, air bubble and water. $A_{11} = 5.04 \times 10^{-20}$ J, $A_{22} = 0$ J, and $A_{33} = 4.38 \times 10^{-20}$ J (Yordan, 1989), which gives $A_{132} = -3.12 \times 10^{-21}$.

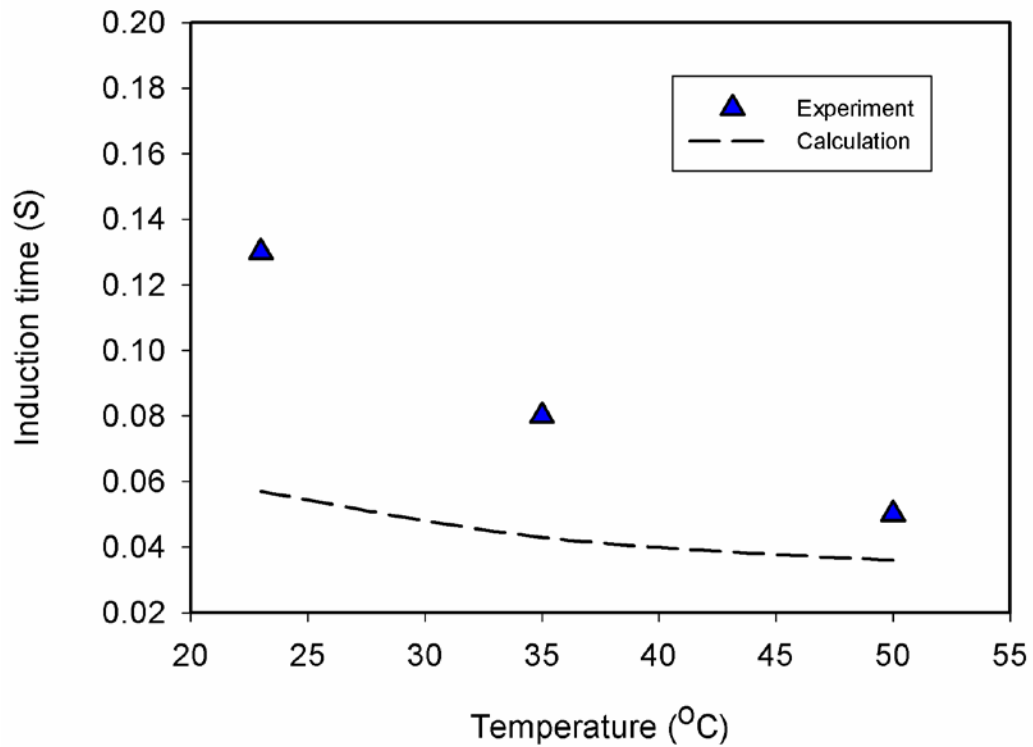


Figure 7.1 Experimental and calculated induction time values for rising air bubbles ($D = 0.22$ mm) towards a hydrophobic silica surface in water (surface inclination = 60°), $\psi_{\text{Silica}} = -20$ mV (Yordan, 1989), $\psi_{\text{Bubble}} = -45$ mV, $H_{\text{cr}} = 110$ nm (Yordan, 1989), $K_{123} = 6.13 \times 10^{-19}$ (Yoon and Aksoy, 1999), $A_{132} = -3.12 \times 10^{-21}$.

CHAPTER 8: SUMMARY AND FUTURE WORK

8.1 Research contributions

8.1.1 Single micro bubble generation

A method of making single gas bubbles has been successfully developed in this study. It was found that the reduction in the micropipette tip size is the most effective way to decrease the bubble size. The size of generated gas bubbles can be predicted by Raleigh Plesset model. Several other factors such as gas type, micropipette inclination, and taper length were also studied.

8.1.2 Sliding velocity and induction time

In this study, gas bubble-flat surface interactions were investigated by determining two dynamic parameters, bubble sliding velocity and induction time of a gas bubble moving underneath an inclined flat surface. A single micro-bubble released from a micropipette was allowed to move towards an inclined solid collector surface. After reaching its terminal velocity, the bubble approached and contacted the collector surface, changing from a free rising bubble to a sliding bubble against the collector surface above the bubble. A complete trajectory of bubble movement was monitored and recorded by a high speed CCD video imaging system. Redlake software was used to analyze the recorded videos and convert all observations to numerical values of sliding velocity and induction time.

Various types of gas bubbles (CO_2 , Air, H_2 , and O_2) and collector surfaces (bitumen, treated hydrophobic and hydrophilic silica) were used in sliding velocity and induction time measurements. The effect of physical and chemical factors, such as separation between bubbles and collector surfaces and water chemistry (process water, de-ionized water, and simulated process water) on bubble sliding velocity and induction time was investigated. Our study demonstrated that the sliding velocity of gas bubbles under an inclined collector surface is a strong function of water chemistry, gas type, temperature, and hydrophobicity of the collector surface. A major role of the surface forces in bubble-solid attachment was established. These studies provide excellent information on gas-bitumen interaction that would assist in the understanding of gas-bitumen attachment under diverse conditions.

8.1.3 Sliding velocity modeling

In this part of research an analytical model proposed for predicting bubble sliding velocity. Investigation of dynamic forces affecting the sliding velocity was carried out. Previously developed models were used as basis for modeling purposes. The final model equation was solved by analytical methods. The model was compared with experimental results and a good agreement between the experimental results and model calculations was obtained.

8.1.4 Bubble zeta potential measurements

In this part of the research, a new method for bubble zeta potential measurements was developed. The measurements were carried out for several systems including systems reported in literature. The effect of cationic and anionic surfactants on bubble zeta potential was also studied. The surfactants were selected based on the previous work by Yoon (1979). SDS (sodium dodecyl sulphate) was used as anionic surfactant and DAH (dodecylamine hydrochloride) as cationic surfactant. Zeta potential of air bubbles in simulated and Aurora Plant process water was also measured. Simulated process water was deionized water with dissolved CaCl_2 . We also separated foam and residual from Aurora plant water. The foam fraction has higher concentration of natural surfactants as compared to residual fraction.

8.2 Prospect of future work

The following is suggested for future work:

1. Study more in depth the interaction forces between air bubble and solid surfaces.
2. Investigate the critical film thickness between air bubble and bitumen droplet, and physic-chemical conditions, which can improve the process.
3. Understand the mechanism of selectivity to improve the process in a desired direction. In oil sands extraction, in a flotation process there

are air bubbles and bitumen droplets and sand particles and the selectivity of air bubble is one of the important factors to increase recovery and improve froth quality.

4. Study the slime coating of fine solids on both bitumen and air bubbles. A systematic study on bitumen/bubble interaction should be carried out in the presence of fine solids to provide more information on bitumen extraction from oil sands.

BIBLIOGRAPHY

Adamson, A. W., 1982, Physical chemistry of surfaces. John Wiley and Sons, New York.

Alexander, K.L., Li, D., 1996, Effects of bitumen films over air bubble surfaces on bitumen drop-air bubble attachment, Colloids and Surfaces A: Physicochemical and Engineering Aspects 106, 191-202.

Apfel, R. E., 1970, The role of impurities in cavitation-threshold determination, The Journal of the Acoustical Society of America, 48 (5).

Attard, P., 1989, Long range attraction between hydrophobic surfaces. Journal of Physical Chemistry, 93(17), 6441-6444.

Attard, P., 1996, Bridging bubbles between hydrophobic surfaces. Langmuir, 12 (6), 1693-1695.

Basu, S., Nandakumar, K., Lawrence, S., Masliyah, J.H., 2004, Effect of calcium ion and montmorillonite clay on bitumen displacement by water on a glass surface, Fuel 83 (17).

Bichard, J. A., 1987, Oil sands composition and behavior research. The research papers of John A. Bichard ,1957-1965. AOSTRA, Edmonton, AB.

Bird, R. B., Armstrong, R. C., Hassager, O., 1987, Dynamics of polymeric liquids, John Wiley and Sons.

Blanchard, D. C., Syzdek, L. D., 1977, Production of air bubbles of a specified size, Chemical Engineering Science 32, 1109-1111.

Bowman, C. W., 1968, Molecular and interfacial properties of Athabasca tar sands, in "Proceedings of the 7th World Petroleum Congress", Elsevier, Mexico City, Mexico, 583-604.

Cameron, A., 1966, The principles of Lubrication, Longmans, London.

Camp, F.W., 1977, Processing Athabasca Tar Sands – Tailing Disposal, Canadian Journal of Chemical Engineering, 55, 581-591.

Cho, S.H., Kim, J.Y., Chun, J.H., Kim, J. D., 2005, Ultrasonic formation of nano-bubbles and their zeta-potentials in aqueous electrolyte and surfactant solutions, Colloids and Surfaces A: Physicochemical and Engineering Aspects, 269 (1-3) 28-34.

Christenson, H.K., Claesson, P.M., 1988, Cavitation and interaction between macroscopic hydrophobic surfaces, Science (Washington, D. C.), 239 (4838), 390-392.

Claesson, P.M, Blom, C.E., Herder, P.C., Ninham, B.W., 1986, Interactions between water-stable hydrophobic Langmuir-Blodgett monolayer's on mica. Journal of Colloid Interface Science, 114(1), 234-42.

Claesson, P.M., Christenson, H.K., 1988, Very long range attractive forces between uncharged hydrocarbon and fluorocarbon surfaces in water, Journal of Physical Chemistry, 92(6),1650-5.

Clark, K. A., 1923, The bituminous sands of Northern Alberta. Their separation and their utilization in road construction. Alberta Research Council, Edmonton Research Council of Alberta Annual Report, 1922.

Clark, K.A. 1929, The separation of the bitumen from Alberta bituminous sands. Canadian Institute of Mining and Metallurgy Bulletin 20, 1385-1395.

Clift, R., Grace, J. R., Weber, M. E., 1978, Bubbles, drops, and particles, New York : Academic Press.

Conway, B. E., 1975, Ion hydration near air/water interfaces and the structure of liquid surfaces, Journal of Electro analytical Chemistry, 65 (2), 491-504.

Conybeare, C.E.B., 1966, Origin of Athabasca oil sands: a review, *Bulletin of Canadian Petroleum Geology*, v. 14, 145-163.

Crawford, R., Ralston, J., 1988, The influence of particle size and contact angle in mineral flotation, *International Journal of Mineral processing*, 23, 1–24.

Dabros, T., Hamza, H.A., Dai, Q., Czaenecki, J., 2002, Attachment of gas bubbles to solid surface from an impinging jet in “Emulsions, Foams, and Thin Films”, Mittal, K. L. and Kumar, P. (eds.), Marcel Dekker, New York, 411-431.

Dai, Z., Dukhin, S., Fornasiero, D., Ralston, J., 1988, The inertial hydrodynamic interaction of particle and rising bubble with mobile surface, *Journal of Colloid Interface Science*, 197, 275-292.

Dai, Z., Fornasiero, D., Ralston, J., 1999, Particle bubble attachment in mineral flotation, *Journal of Colloid Interface Science*, 217, 70-76.

Dai, Z., Fornasiero, D., Ralston, J., 2000, Particle bubble collision model a review, *Advances in colloid and interface science*, 85, 231-256.

DeBisschop, K., Miksis, Michael, Eckman, D., 2002, Bubble rising in an inclined channel, *Journal of Physics of Fluids*, 14 (1), 93-104.

Dewsbury, K., Karamanev, D., Margaritis, A., 1999, Hydrodynamic characteristics of free rise of light solid particles and gas bubbles in non-Newtonian liquids, *Chemical Engineering Science* 54, 4825 –4830.

Dobby, G.S., Finch, J. A., 1987. Particle size dependence in flotation derived from a fundamental model of the capture process. *International Journal of Mineral Processing* 21, 241–260.

Dobby, G. S., Finch, J. A., 1986, A model of particle sliding time for flotation size bubbles, *Journal of Colloid Interface Science*, 109 (2), 493-498.

Drelich, J. and Miller, J. D. 1994, Surface and interfacial tension of the Whiterocks bitumen and its relationship to bitumen release from tar sands during hot water processing. *Fuel* 73, 1504-1510.

Drelich, J., Lelinski, D., Hupka, J., Miller, J.D., 1995, The role of gas bubbles in bitumen release during oil sand digestion. *Fuel* 74, 1150-1155.

Drelich, J., Lelinski, D., Miller, J.D., 1996, Bitumen spreading and formation of thin films at a water surface. *Colloids and Surfaces A: Physicochem. And Engineer. Aspects* 116, 211-223.

Drost-Hansen, W., 1969, Structure of water near solid interfaces, *Industrial and Engineering Chemistry Research*. 61(11), 10-47.

Eaton, A.D., Franson, M.H., 2005, Standard methods for the examination of water and wastewater, 21st ed. Centennial ed. / prepared and published jointly by American Public Health Association.

Eriksson, J.C., Lijuggren, S. Claesson, P.M., 1989, A phenomenological theory of long-range hydrophobic attraction forces based on a square-gradient variational approach. *Journal of Chemical Society, Faraday Trans.* 85 (3), 163-167.

Fletcher, N. H., 1993, van der Waal's equation and nucleation theory, the *European Physical Society*, 14, 29-35.

Garcia, H.E., Gordon, L.I., 1992, Oxygen solubility in seawater :Better fitting equations. *Limnology and Oceanography*, 37(6), 1307-1312.

Graciaa, A., Morel, G., Saulner, P., Lachaise, J., Schechter, R.S., 1995, The zeta potential of gas bubbles, *Journal of Colloid and Interface Science*. 172 (1), 131-137.

Gu, G., Xu, Z., Nandakumar, K., Masliyah, J., 2002, Influence of water-soluble and water –insoluble natural surface active components on the stability of water-in-toluene diluted bitumen emulsion, *Fuel* 81, 1859–1869.

Gu, G., Xu, Z., Nandakumar, K., Masliyah, J., 2003, Effects of physical environment on induction time of air – bitumen attachment, *International Journal of Mineral Processing* 69, 235–250.

Gu, G., Sanders.R.S, Xu, Z., Nandakumar, K., Masliyah, J., 2004, A novel experimental technique to study single bubble-bitumen attachment in flotation, *International Journal of Mineral Processing*, 69, 235–250.

Hallowell, C., Hirt, D., 1994, Unusual characteristics of the maximum bubble pressure method using a teflon capillary, *Journal of Colloid and Interface Science* 168, 281-288.

Hamme, R.C., Emerson, S.R., 2004, The solubility of Neon, Nitrogen and Argon in distilled water and seawater, *Deep-Sea Research Part I- Oceanographic Research Papers*, 51 (11), 1517-1528.

Hepler, L.G., Hsi, C., 1989, AOSTRA Technical Handbook on Oil Sands, Bitumen and Heavy Oils, AOSTRA technical publication series #6, Alberta Oil Sands Technology and Research Authority: Edmonton, AB.

Hepler, L.G., Smith, R.G., 1994, The Alberta Oil Sands: industrial procedures for extraction and some recent fundamental research, AOSTRA technical publication series #14, Alberta Oil Sands Technology and Research Authority: Edmonton, AB.

Hewitt, D., Fornasiero, D., Ralston, J., 1995, Bubble–particle attachment, *Journal of Chemical Society, Faraday Trans.*, 91 (13), 1997–2001.

Ishida, N., Sakamoto, M., Miyahara, M., Higashitani, K., 2002, Optical observation of gas bridging between hydrophobic surfaces in Water, *Journal of Colloid Interface Science*, 253, 112-116.

Israelachvili, J.N., Pashely, R.M., 1984, Measurement of the hydrophobic interaction between two hydrophobic surfaces in aqueous electrolyte solutions. *Journal of Colloid Interface Science*, 98 (2), 500-514.

Kameda, M., Matsumoto, Y., 1999, Nonlinear oscillation of a spherical gas bubble in acoustic fields, *The Journal of the Acoustical Society of America* 106, 3156.

Kampmeyer, P.M., 1952, The temperature dependence of viscosity for water and mercury, *Journal of Applied Science* 23-1, 99-102.

Kargupta, K., Sharma, A., 2002, Creation of ordered pattern by dewetting of thin films on homogeneous and heterogeneous substrates, *Journal of Colloid Interface Science*, 245, 99-115.

Kasongo, T., Zhou, Z., Xu, Z., Masliyah, J.H., 2000, Effect of clays and calcium ions on bitumen extraction from Athabasca oil sands using flotation, *Canadian Journal of Chemical Engineering* 78, 674.

Khurana, A. K., Kumar, R., 1969, Studies in bubble formation, *Chemical Engineering Science*, 24, 1711-1723.

Klaseboer, E., Chevalier, J.Ph., Gourdon, C., Masbernat, O., 2000, Film drainage between colliding drops at constant approach velocity: Experiments and Modeling, *Journal of Colloid and Interface Science* 229, 274-285.

Klaseboer, E., Chevalier, J. Ph., Mate, A., Masbernat, O. Gourdon, C., 2001, Model and experiments of a drop impinging on an immersed wall, *Physics of Fluids* 13 (1), 45-57.

Kovalchuk, V. L., Fainerman, V. B., Miller, R., Dukhin, S. S., 1998. Bubble formation in maximum bubble pressure measuring systems employing a gas reservoir of limited volume, *Colloids Surfaces, (Physicochemical Engineering Aspects)* 143, 381-393.

Krasowskak, M., Krastev, R., Rogalski, M., Malysa, K., 2007, Air-facilitated three-phase contact formation at hydrophobic solid surfaces under dynamic Conditions, *Langmuir* 23 (2), 549 -557.

Kubota, K., Hayashi, S., Inaoka, M., 1983, A convenient experimental method for measurement of zeta-potentials generating on the bubble suspended in aqueous surfactant solutions, *Journal of Colloid and Interface science.* 95 (2), 362-369.

Laskowski, J., Kitchener, J.A., 1969. The hydrophilic–hydrophobic transition on silica, *Journal of Colloid Interface Science*, 29, 670–679.

Leja, J, 1982, *Surface chemistry of froth flotation*, Plenum, New York.

Leja, J. and Bowman, C.W. 1968, Application of thermodynamics to the Athabasca tar sands. *Canadian Journal of Chemical Engineering*, 46, 479-481.

Levich, V. G., 1962, *Physicochemical Hydrodynamics*, Prentice-Hall, Englewood Cliffs, NJ, 409-429.

Li, C., Somasundaran, P., 1992, Reversal of bubble charge in multivalent inorganic salt solutions effect of aluminium, *Journal of Colloid and interface Science*, 148 (2).

Lighthill, J., 1986, *An informal introduction to theoretical fluid mechanics*, Oxford Scientific Publication.

Liow, J. L., 2000, Quasi equilibrium bubble formation during top submerged gas injection. *Chemical Engineering Science* 55, 4515- 4524.

Liu, J., Zhou, Z., Xu, Z., 2002, Electrokinetic study of Hexane droplets in surfactant solutions and process water of bitumen extraction systems, *Industrial and Engineering Chemistry Research*, 41, 52-57.

Longuet-Higgins, M. S., Kerman, B., Lunde, K., 1991, The release of air bubbles from an underwater nozzle, *Journal of Fluid Mechanics*, 230, 365-390.

Marmur, A., Rubin, E., 1973, Equilibrium shapes and quasi-static formation of bubbles at submerged orifice, *Chemical Engineering Science*, 28, 1455-1464.

Martanto, W., Baisch, S.M., Costner, E.A., Prausnitz, M.R., 2005, Fluid dynamics in conically tapered microneedles, *AIChE Journal* 51 (6), 1599-1607.

Masliyah, J. H., Jauhari, R., Gray, M., 1994, Drag coefficient for air bubbles rising along an inclined surface, *Journal of Chemical Engineering Science*, 49 (12), 1905-1911.

Masliyah, J., 2003, Intensive Short Course: Extraction of Oilsands Bitumen, University of Alberta, Edmonton, AB, Canada.

Masliyah, J. H., Bhattacharjee, S., 2006, *Electrokinetic and Colloid Transport Phenomena*, published by John Wiley and Sons Inc.

Maxworthy, T., 1991, Bubble rise under an inclined plate, *Journal of Fluid Mechanics*, 229, 659.

McGraw, R., Wu, D.T., 2003, Kinetic extensions of the nucleation theorem, *The Journal of Chemical Physics*, 118 (20).

Moran, K., Yeung, A., Masliyah, J., 2000, Factors affecting the aeration of small bitumen droplets, *Canadian Journal of Chemical Engineering*, 78, 625-634.

Moran, K., Yeung, A., Masliyah, J., 1999, Measuring interfacial tensions of micrometer-sized droplets: A novel micromechanical technique, *Langmuir* 15, 8497-8504.

Neimark, A.V., Vishnyakov, A., 2005, The birth of a bubble: a molecular simulation study, *The Journal of Chemical Physics*, 122, 54707.

Nguyen, A.V., Ralston, J., Schulze, H.J., 1998, On modelling of bubble – particle attachment probability in flotation. *Int. J. Miner. Process.* 53, 225–249.

Nguyen, A.V., G.M. Evans, Nalaskowski, J., D.Miller, J., 2004, Hydrodynamic interaction between an air bubble and a particle: atomic force microscopy measurements” *Journal of experimental thermal and fluid science*, 28, 387-394.

Nguyen, A.V., Schulze, H.J., 2004, *Colloidal Science of Flotation, Surfactant Science Series, Volume 18*, Marcel Dekker, Inc. New York.

Oguz, H.N., Prosperetti, A., 1993, Bubble growth and detachment from a needle, *Journal of Fluid Mechanics*, 257, 111-144.

Okada, K., Akagi, Y., Kogure, M., Yoshioka, N., 1990, Effect of surface charges of bubbles and fine particles on air flotation process, *Canadian Journal of Chemical engineering*, 68, 393-399.

Okada, K., Akagi, Y., 1987, Method and apparatus to measure the ξ -potential of bubbles. *Journal of Chemical Engineering of Japan*, 20 (1).

Parker, J.L., Claesson, P.M., Attard, P., 1994, Bubbles, cavities, and the long ranged attraction between hydrophobic surfaces. *Journal of Physical Chemistry*, 98 (34), 8468-8480.

Paulsen, F. G., Pan, R., Bousfield, D. W., Thompson, E. V., 1996, The dynamics of bubble/particle attachment and the application of two

disjoining film rupture models to flotation: I. Nondraining model, *Journal of Colloid Interface Science*, 178, 400-410.

Peng, F. F., 1996, Surface energy and induction time of fine coals treated with various levels of dispersed collector and their correlation to flotation responses," *Energy and Fuels* 10, 1202-1207.

Phianmongkhon, A., Varley, J., 2003, Zeta potential ξ measurement for air bubbles in protein solutions, *Journal of Colloid and Interface Science*, 260, 332-338.

Podgornik, R., Parsegian, V.A., 1995, Forces between CTAB-covered glass surfaces interpreted as an interaction driven surface instability, *Journal of Physical Chemistry*, 99 (23), 9491-9496.

Portisky, H., 1952, The collapse or growth of a spherical bubble or cavity in a viscous liquid, *Proceedings of the First U.S. National Congress on Applied Mechanics*, New York.

Rabinovich, Y. I., Guzonas, D.A., Yoon, R. H., 1993, Role of chain order in the long range attractive force between hydrophobic surfaces, *Langmuir*, 9 (5), 1168-70.

Rabinovich, Y.I., Deryagin, B.V., 1988, Interaction of hydrophobized filaments in aqueous electrolyte solutions, *Colloids and Surfaces*, 30 (3-4), 243-251.

Ralston, J., Fornasiero, D., Hayes, R., 1999, Bubble-particle attachment and detachment in flotation, *International Journal of Mineral Processing*, 56, 133-164.

Ralston, J., Fornasiero, D., Mishchuk, N., 2001, The hydrophobic force in flotation a critique, *Colloid and Surfaces, Physicochemical and Engineering Aspects*, 192, 39-51.

Ralston, J., Dukhin S. S., Mishchuck, N. A., 2002, Wetting film stability and flotation kinetics, *Advanced Colloid Interface Science*, 95, 145-236.

Ramakrishnan, S., Kumar, R., Kuloor, N., 1969. Studies in bubble formation under constant flow conditions, *Chemical Engineering Science* 24, 731.

Ruckenstein, E., Churaev, N.V., 1991, A possible hydrodynamic origin of the forces of hydrophobic attraction, *Journal of Colloid Interface Science*, 147 (2), 535-538.

Saulnier, P., Bouriat, P., Morel, G., Lachaise, J., Graciaa, A., 1998, Zeta potential of air bubbles in solution of binary mixtures of surfactants. *Journal of Colloid and Interface science*, 200 (1), 81-85.

Schnorf, M., Potrykus, I., Neuhaus, G., 1994, Microinjection technique: routine system for characterization of microcapillaries by bubble pressure measurement, *Experimental Cell Research*, 210, 260- 267.

Schramm, L.L., Smith, R.G., 1985, Influence of natural surfactants on interfacial charges in the hot water process for recovering bitumen from the Athabasca oil sands, *Colloids and Surfaces*, 14, 67–85.

Schulze, H.J., Gottschalk, G., 1981, Investigations of the hydrodynamic interaction between a gas bubble and mineral particles in flotation. In: Laskowski, J. (Ed.), *Proc.13th Int. Min. Process. Congress Warsaw*, June 1979. Elsevier, New York, NY, 63–84.

Schulze, H.J., 1984, *Physico-chemical elementary process in flotation*, Elsevier Publication, Amsterdam, 124-129.

Schulze, H. J. and J. O. Birzer, 1987, Stability of thin liquid-film on Langmuir Blodgett layers on silica," *Colloids and Surfaces*, 24 (2-3), 209-224.

Schulze, H. J., 1992, Probability of particle attachment on gas-bubble by sliding, *Advances in Colloid and Interface Science*, 40, 283-305.

Sherwood, J.D., 1986, Electrophoresis of gas bubbles in a rotating fluid, *Journal of Fluid Mechanics*, 162, 129-137.

Shirota, M., Kameda, M., 2001. The bubble generator to produce 0.1 mm diameter gas bubble. 4th International conference on multiphase flow, #451.

Seyyed Najafi A., Drelich J., Yeung A., Xu Z., and Masliyah J., 2007, A novel method of measuring electrophoretic mobility of gas bubbles, *Journal of Colloid and Interface Science*, 308, 2, 344-350.

Seyyed Najafi A., Xu Z., and Masliyah J., 2008, Single micro bubble generation by pressure pulse technique, *Journal of Chemical Engineering Science*, 63 (7), 1779-1787.

Seyyed Najafi A., Xu Z., and Masliyah J., 2008, Measurement of sliding velocity of a single micro bubble under an inclined collector surface, *Canadian Journal of Chemical Engineering*, 86 (6), 1001-1010.

Simmons, D., A. Chauhan, 2006, Influence of physical and chemical heterogeneity shape on thin film rupture, *Journal of Colloid Interface Science*, 295, 472-481.

Steitz, R., T. Gutberlet, T. Hauss, B. Klosgen, R. Krastev, S. Schemmel, A. C. Simonsen and G. H. Findenegg, 2006, Nanobubbles and their precursor layer at the interface of water against a hydrophobic substrate, *Langmuir*, 22 (11), 5025 -5035.

Stockelhuber, K. W., Radoev, B., Wenger, A., Schulze, H. J., 2003, Rupture of wetting films caused by nano-bubbles, *Langmuir*, 20,164-168.

Sury, K.N., 1990, Low Temperature Bitumen Recovery Process, US patent 4 946 597.

Sury, K.N., 1992, Low Temperature Bitumen Recovery Process, Canadian Patent 1 302 327.

Takahashi, M., 2005, Zeta potential of micro-bubbles in aqueous solutions: electrical properties of the gas-water interface, *Journal of Physical Chemistry B*, 109, 21858.

Takamura, K., Chow, R.S., 1985, The electrical properties of the bitumen/water interface. Part II. Application of the ionisable surface-group model. *Colloids and Surfaces*, 15, 35-48.

Takamura, K., Wallace, D., 1988, The physical chemistry of the hot water process, *Journal of Canadian Petroleum Technology*, 27, 98-1068.

Takamura, F., Matsumoto, Y., 2000, Dissolution rate of spherical carbon dioxide bubbles in strong alkaline solutions, *Chemical Engineering Science* 55, 3907- 3917.

Thiriet, M., Ribreau, C., 2000, Computational flow in a collapsed tube with wall contact, *Mécanique and Industries*, 1, 349- 364.

Tyrrell, J. W. and P. Attard, 2001, Images of nano-bubbles on hydrophobic surfaces and their interactions, *Physics Review Letter*, 87, 176104.

Tyrrell, J. W. and P. Attard, 2002, Atomic force microscope images of nano-bubbles on a hydrophobic surface and corresponding force-separation data, *Langmuir*, 18, 160-167.

Tsao H. K., Koch D., 1994, Collisions of slightly deformable high Reynolds number bubbles with short – range repulsive forces, *Physics of Fluids* 6 (8), 2591-2605.

- Tsao H. K., Koch D., 1997, Observations of high Reynolds number bubbles interaction with a rigid wall, *Physics of Fluids*, 9 (1), 44-56.
- Turton, R., Levenspiel, O., 1986, A short note on the drag correlation for spheres *Powder Technology*, 47 (1), 83–86.
- Usui, S., Sasaki, H., 1970, Zeta potential measurement of bubbles in aqueous surfactant solutions, *Journal of Colloid and Interface Science*, 65 (1).
- Vigrass, L.W., 1968, Geology of Canadian heavy oil sands: *AAPG Bulletin*, 52, 10, 1984-1999.
- Vinogradova, O. I, 1995, Drainage of a thin liquid film confined between hydrophobic surfaces, *Langmuir*, 11, 2213-2220.
- Wang, W., Z. Zhou, Nandakumar, K., Masliyah, J.H., Xu, Z., 2005, An induction time model for the attachment of an air bubble to a hydrophobic sphere in aqueous solutions, *International Journal of Mineral Processing*, 75, 69-82.
- Yaminskii, V.V., Yushchenko, V.S., Amelina, E.A., Shchukin, E.D., 1983, Cavity formation due to a contact between particles in a nonwetting liquid, *Journal of Colloid Interface Science*, 96(2), 301-306.
- Yang, C., Dabros, T., Li, D., Czarnecki, J. and Masliyah, J.H., 1999, Analysis of fine bubble attachment onto a solid surface within a framework of classical DLVO theory. *Journal of Colloid Interface Science*, 219, 69-80.
- Yang.C, Dabros.T, Li.D, Czarnecki.J, Masliyah.J, 2001, Measurement of Zeta potential in aqueous solution by microelectrophoresis method, *Journal of Colloid Interface Science*, 243, 128-135.

Yang, C, Dabros, T, Li, D, Czarnecki, J, Masliyah, J.H., 2003, Kinetics of micro-bubble - solid interaction and attachment, *AIChE Journal*, 49 (4), 1024-1037.

Yoon, R.H., Yordan, J.L., 1986, Zeta-potential measurements on micro-bubbles generated using various surfactants, *Journal of Colloid and Interface Science*, 113 (2), 430-438.

Yoon, R.H., Luttrell, G.H., 1989, The effect of bubble size on fine particle flotation, *Mineral Processing and extractive Metallurgy Reviews*, 5, 101-122.

Yoon, R. H., Luttrell, G. H., Laskowski, J., 1989, *Frothing in flotation*, Gordon and Breach, New York.

Yoon, R.H., Yordan, J.L., 1991, Induction time measurements for the quartz–amine flotation system, *Journal of Colloid Interface Science*, 141 (2), 374–383.

Yoon, R., Mao, L., 1996, Application of extended DLVO theory, IV derivation of flotation rate equation from first principles, *Journal of Colloid Interface Science*, 181, 613-626.

Yoon R. H., Flinn, D. H., Rabinovich, Y. I., 1997, Analyzing electric double layers with the atomic force microscope, *Journal of Colloid Interface Science*, 185, 363-370.

Yoon, R.-H., Aksoy, B.S., 1999. Hydrophobic forces in thin water films stabilized by dodecylammonium chloride, *Journal of Colloids and Interface Science*, 211, 1–10.

Yordan, J.L., 1989. *Studies on the Stability of Thin films in Bubble–Particle Adhesion*. PhD Thesis, Virginia Polytechnic Institute and State University.

Zhang, L. Y., Z. Xu, Masliyah, J. H., 2003, Langmuir and Langmuir-Blodgett films of mixed asphaltene and a demulsifier, *Langmuir*, 19, 9730-9741.

Zhang, X. H., Maeda, N., Craig, V. S. J., 2007, Physical properties of nano-bubbles on hydrophobic surfaces in water and aqueous solutions, *Journal of Physical Chemistry C*, 111 (15), 5743 -5749.

Zhou, Z. A., Hussien, H., Xu, Z., Czarnecki, J., Masliyah, J.H., 1998, Interaction of ionic species and fine solids with a low energy hydrophobic surface from contact angle measurement, *Journal of Colloid Interface Science*, 204, 342-349.

Zukoski, E. E. 1966, Influence of viscosity, surface tension, and inclination angle on the motion of long bubbles in closed tubes, *Journal of Fluid Mechanics*, 25, 821–837.

Appendix A. Derivation of Plesset equation

I am interested in the response of a bubble on the tip of capillary to a time varying pressure pulse. For this purpose, I will start with the well known Rayleigh-Plesset equation and I will try to modify it for our system.

At time $t \leq 0$, a curvature of bubble with radius R_0 is at rest in an incompressible, viscous liquid. The hydrostatic pressure is P_h and pressure inside the line is $P_{(s)}$ and is a constant.

At time $t \geq 0$, a pressure $P_{(t)}$, which varies with time is superimposed on $P_{(s)}$, so that the gas pressure inside the bubble is $P_{(p)} = P_{(s)} + P_{(t)}$. Consequently, the bubble radius will change to some new value $R_{(t)}$.

During this process, the liquid will acquire a kinetic energy of:

$$dE_k = \frac{1}{2} \rho \int_R^\infty 4\pi r^2 \left(\frac{dr}{dt}\right)^2 dr \quad (A-1),$$

where r is the radial coordinate. Using the liquid incompressibility condition

$$\left(\frac{dr}{dt}\right) / \left(\frac{dR}{dt}\right) = \frac{R^2}{r^2} \quad \text{in the above equation, we will obtain:}$$

$$dE_k = 2\pi\rho R^3 \left[\frac{dR}{dt}\right]^2. \quad \text{This energy change is equal to the work done by}$$

pressure pulse:

$$\int_{R_0}^R (P_l - P_h) 4\pi r^2 dr = 2\pi\rho R^3 \left[\frac{dR}{dt}\right]^2 \quad (A-2)$$

If the hydrostatic pressure in a liquid of surface tension γ is P_h then the internal pressure of bubble of radius R_0 at $t = 0$, will be $P_{(s)} = P_h + \left[\frac{2\gamma}{R_0} \right]$.

After introducing a pressure pulse and changing the bubble inside pressure to the P_b , the bubble radius will change to R , and the gas pressure within the bubble will be $P_b = (P_h + \frac{2\gamma}{R_0}) \left[\frac{R_0}{R} \right]^{3\kappa}$, assuming this gas is Ideal gas, κ is the polytropic index of gas, which takes a different value depending on whether the gas behaves isothermally, adiabatically, or with intermediate characteristics.

Therefore, the pressure in the liquid immediately beyond the bubble wall be $(P_h + \frac{2\gamma}{R_0} + P_t) \left[\frac{R_0}{R} \right]^{3\kappa} - \frac{2\gamma}{R}$. In fact, the hydrostatic pressure in the layer

of water adjacent to the bubble is $P_L = (P_h + \frac{2\gamma}{R_0}) \left[\frac{R_0}{R} \right]^{3\kappa} - \frac{2\gamma}{R} - \frac{4\mu \left(\frac{dR}{dt} \right)}{R}$

Portisky (1952) shows that the final term, containing the viscosity μ of the liquid, is required to ensure continuity of normal stress at the bubble wall.

Now we will put equation for P_L in the above integral and differentiate with respect to t will give:

$$R \frac{d^2R}{dt^2} + \frac{3}{2} \left(\frac{dR}{dt} \right)^2 = \frac{1}{\rho} \left[\left(P_h + \frac{2\gamma}{R_0} \right) \left(\frac{R_0}{R} \right)^{3\kappa} - \frac{2\gamma}{R} - \frac{4\mu}{R} \frac{dR}{dt} - P_h - P_{(t)} \right] \quad (A-3)$$

$$R \frac{d^2R}{dt^2} + \frac{3}{2} \gamma \left(\frac{dR}{dt} \right)^2 = \frac{1}{R} \left[\left(P_0 + \frac{2\gamma}{R_0} + P_p \right) \left(\frac{R_0}{R} \right)^3 - \frac{4\mu}{dt} - P_0 - P_{(p)} \right] \quad (\text{A-4})$$

$$R \frac{d^2R}{dt^2} + \frac{3}{2} \gamma \left(\frac{dR}{dt} \right)^2 = \frac{1}{R} \left[\left(P_0 - \frac{2}{R_0} - P_L - \frac{4\mu}{dt} \right) \right] \quad (\text{A-5})$$

Appendix B. Effect of inclination angle on added mass force

As a body starts to move in a fluid, some of the surrounding fluid moves as well. When the body accelerates, it causes acceleration to the surrounding liquid. It is then clear that more force is required to accelerate the body in the fluid. The added mass force is considered as an “imaginary” added mass to the body. Here, the added mass force will be derived by considering the hydrodynamic force acting on the object as it accelerates. Let us consider in cylindrical coordinates a sphere of radius R , accelerating at rate of \dot{U} in z direction in an inviscid media. We can evaluate the hydrodynamic force in the z direction by integrating the dynamic pressure over the area projected in the z direction, Figure B.1:

$$F_z = \int P dA_z \quad (B-1),$$

where

$$dA_z = 2\pi R^2 \sin\theta \cos\theta d\theta \quad (B-2).$$

The potential axisymmetric flow around a sphere is given by:

$$\phi = U \cos\theta \frac{R^3}{2r^2} \quad (B-3).$$

The non-steady state Bernoulli equation is given by:

$$P = -\rho_L \left[\frac{\partial\phi}{\partial t} + \frac{1}{2} |\nabla\phi|^2 \right] \quad (B-4).$$

Using Equation (B-3) yields:

$$\left. \frac{\partial \phi}{\partial t} \right|_{r=R} = \dot{U} \frac{R}{2} \cos \theta \quad (\text{B-5})$$

and

$$\left. \frac{1}{2} |\bar{\nabla} \phi|^2 \right|_{r=R} = \frac{1}{2} \left| \bar{\nabla} \left(-U \cos \theta \frac{R^3}{2r^2} - U \sin \theta \frac{R^3}{2r^2} \right) \right|_{r=R}^2 = \frac{1}{2} \left[U^2 \cos^2 \theta + \frac{1}{4} U^2 \sin^2 \theta \right] \quad (\text{B-6}).$$

From equations (A-1) and (A-4) one can obtain:

$$\begin{aligned} F_z &= \int_0^\pi \left[-\rho_L \left[\frac{\partial \phi}{\partial t} + \frac{1}{2} |\bar{\nabla} \phi|^2 \right] \right] 2\pi R^2 \cos \theta \sin \theta d\theta \\ &= \int_0^\pi \left[-\rho_L \left[\dot{U} \cos \theta \frac{R}{2} + \frac{1}{2} (U^2 \cos^2 \theta + \frac{1}{4} U^2 \sin^2 \theta) \right] \right] 2\pi R^2 \cos \theta \sin \theta d\theta \\ &= -\rho_L 2\pi R^2 \dot{U} \frac{R}{2} \underbrace{\int_0^\pi \sin \theta \cos^2 \theta d\theta}_{=2/3} \\ &\quad - \rho_L 2\pi R^2 \frac{1}{2} U^2 \underbrace{\int_0^\pi \left[\sin \theta \cos^3 \theta + \frac{1}{4} \sin^3 \theta \cos \theta \right] d\theta}_{=0} \\ &= -\frac{2}{3} \rho_L \pi R^3 \dot{U} \quad (\text{B-7}), \end{aligned}$$

where \dot{U} is the acceleration of the body. The negative sign indicates that the force is in the negative z-direction, i.e., opposing the acceleration.

Thus, the body must exert this additional force.

By considering Newton law the apparent added mass (m_a) is given by:

$$m_a = \frac{2}{3} \rho_L \pi R^3 = \frac{1}{2} \rho_L V_b \quad (\text{B-8}).$$

In the inclined micropipette case shown in Figure B.2, the direction of the added mass force will be inclined and only the vertical component of this force will affect the force balance equation.

The vertical component of the added mass force becomes:

$$F_v = \frac{1}{2} V_b \dot{U} (\cos \alpha). \quad (\text{B-9}).$$

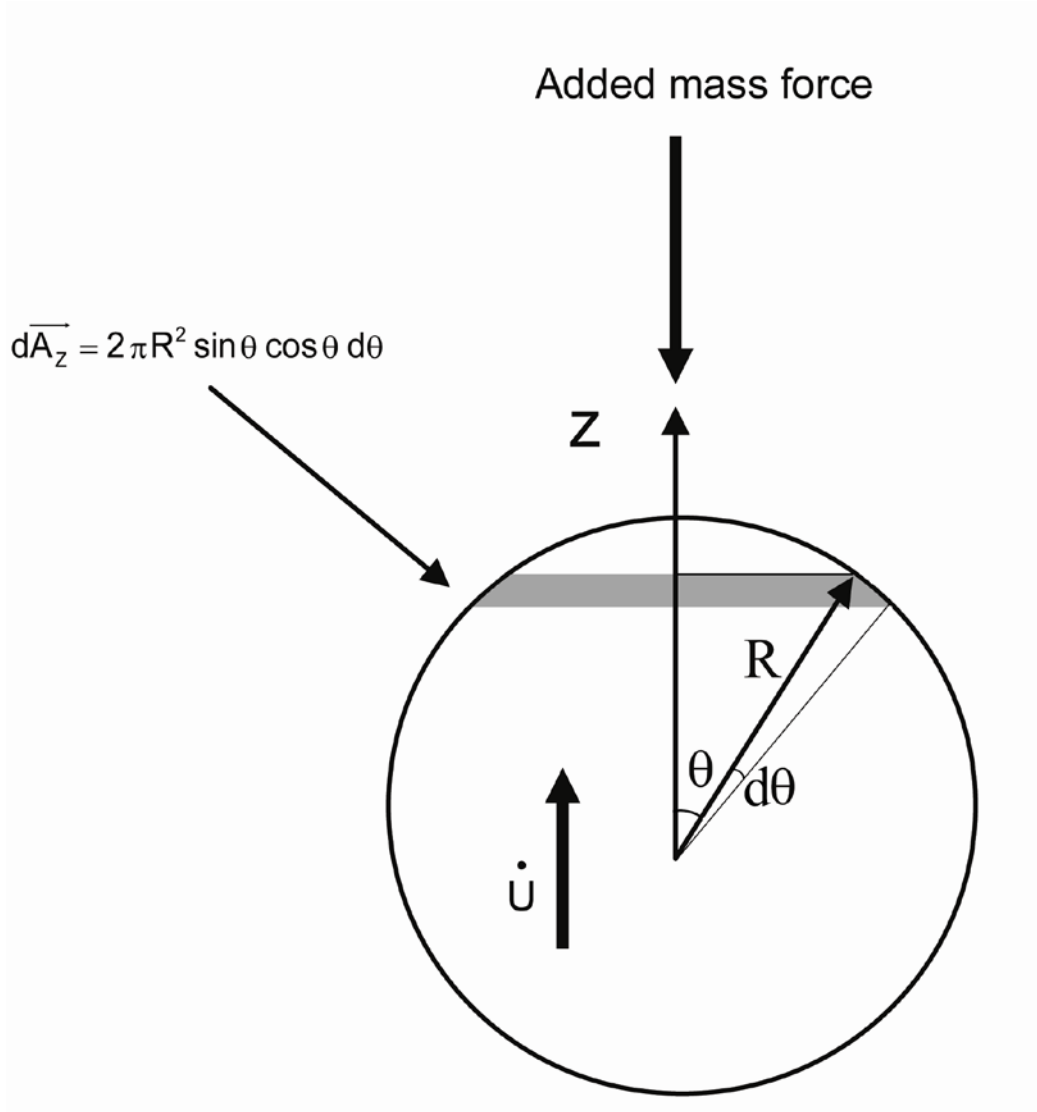


Figure B.1 Added mass force on a spherical bubble.

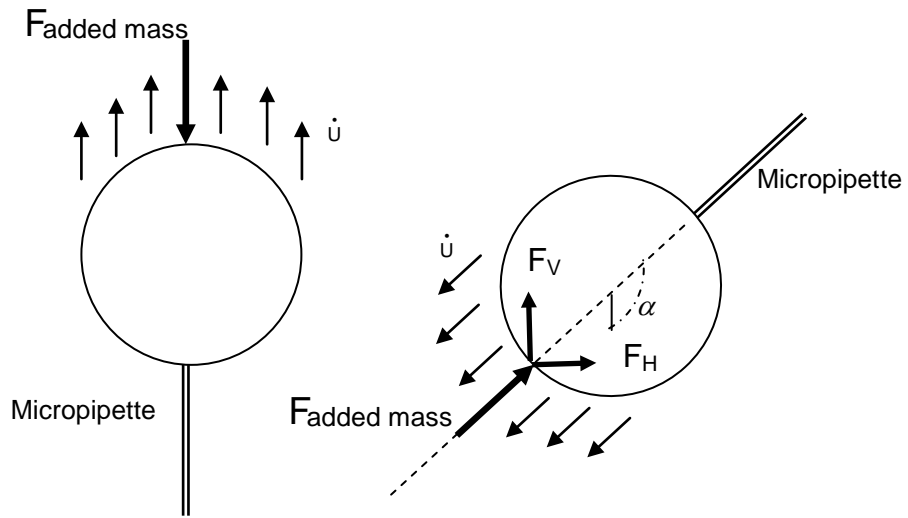


Figure B.2 Effect of inclination on added mass force.

Appendix C. Derivation of Induction time equation

In order to analyse and interpret the experimental data, a simple expression is derived for induction time. For the simplicity of the model, the tangential velocity component is ignored in this model. The problem is to describe the motion of a rising bubble in a quiescent fluid towards a planar plate.

The fluid in this model is a Newtonian fluid. The separation distance between the bubble and collector surface is assumed small compared to the size of the bubble. As it is shown in Figure C.1, a cylindrical coordinate system (r, φ, z) can be defined.

As mentioned earlier, the bubble is assumed spherical and the deformation of both, the bubble and collector surface is ignored. In this system, due to axial symmetry of the film, the coordinate system reduced to (r, z) . Close to the origin of the coordinates, the bubble surface can be described locally as (Vinogradova, 1995):

$$z = H = h + \frac{1}{2} \frac{r^2}{R_b} + o(r^4) \approx h + \frac{1}{2} \frac{r^2}{R_b} \quad (\text{C-1})$$

The governing equations are the continuity and Navier–Stokes equations.

Continuity equation:

$$\frac{1}{r} \frac{\partial}{\partial r} (r v_r) + \frac{\partial v_z}{\partial z} = 0 \quad (\text{C-2})$$

Navier–Stokes equation in r-direction:

$$\rho \left(\frac{\partial v_r}{\partial t} + v_z \frac{\partial v_r}{\partial z} + v_r \frac{\partial v_r}{\partial r} \right) = -\frac{\partial P}{\partial r} + \mu \left[\frac{\partial^2 v_r}{\partial z^2} + \frac{1}{r} \frac{\partial}{\partial r} \left(r \frac{\partial v_r}{\partial r} \right) \right] \quad (\text{C-3})$$

Navier–Stokes equation in z-direction:

$$\rho \left(\frac{\partial v_z}{\partial t} + v_z \frac{\partial v_z}{\partial z} + v_r \frac{\partial v_z}{\partial r} \right) = -\frac{\partial P}{\partial z} + \mu \left[\frac{\partial^2 v_z}{\partial z^2} + \frac{1}{r} \frac{\partial}{\partial r} \left(r \frac{\partial v_z}{\partial r} \right) \right] \quad (\text{C-4})$$

With an order of magnitude analysis these equations are simplified to:

$$\frac{\partial P}{\partial r} = \mu \frac{\partial^2 v_r}{\partial z^2} \quad (\text{C-5})$$

$$\frac{\partial P}{\partial z} = 0 \quad (\text{C-6})$$

This analysis is well developed as lubrication theory (Cameron, 1966; Schulze, 1984; Wang et al., 2005) and it is often referred to as lubrication approximation. The boundary conditions on the bubble and collector surfaces are, at the surface of bubble:

$$v_r = 0 \quad (\text{C-7})$$

$$v_z = -v_h \quad (\text{C-8})$$

At $z = 0$ (the collector surface), for all r , no slip boundary condition gives:

$$v_r(0) = 0 \quad (\text{C-9})$$

$$v_z(0) = 0 \quad (\text{C-10})$$

The symmetry assumption of pressure distribution results in:

$$\left. \frac{dP}{dr} \right|_{r=0} = 0 \quad (C-11)$$

Integrating equation (C-5) twice using the above stated boundary conditions, the velocity along the r-direction becomes:

$$v_r = \frac{1}{2\mu} \frac{\partial p}{\partial r} (z^2 - zH) \quad (C-12)$$

Substitution of v_r into the continuity equation results in:

$$v_z = -\frac{1}{2\mu} \frac{1}{r} \frac{\partial}{\partial r} \left[r \frac{\partial P}{\partial r} \left(\frac{z^3}{3} - \frac{z^2 H}{2} \right) \right] \quad (C-13)$$

Rearranging of equation (C-13) leads to:

$$\frac{d}{dr} \left[r \frac{dP}{dr} \left(\frac{z^3}{3} - \frac{z^2 H}{2} \right) \right] = -2\mu v_z r \quad (C-14)$$

If we only consider the fluid pressure close to the bubble surface ($z = H$), the integration of equation (C-14) leads to:

$$\frac{dP}{dr} = 6\mu v_h \frac{r}{H^3} = 6\mu v_h \frac{r}{\left(h + \frac{1}{2} \frac{r^2}{R_b} \right)^3} \quad (C-15)$$

Integrating of the above equation using the boundary condition leads to:

$$\text{As } r \rightarrow \infty, P = 0 \quad (C-16)$$

The pressure close to bubble surface can be written as:

$$P = -\frac{3\mu R_b v_h}{\left(h + \frac{1}{2} \frac{r^2}{R_b}\right)^2} \quad (\text{C-17})$$

The hydrodynamic resistance force acting on the bubble surface can be evaluated by integrating the total stress on the surface at $z = 0$.

$$F_z = -\int_0^{R_b} \left\{ -P + 2\mu \frac{dv_z}{dz} \right\} 2\pi r \, dr \quad (\text{C-18})$$

Applying the order of magnitude analysis to the above equation by considering the pressure term being much larger than the second term leads to:

$$F_z = -\int_0^{R_b} (-P) 2\pi r \, dr = -\frac{6\pi\mu v_h R_b^2}{h} \quad (\text{C-19})$$

The hydrodynamic fluid resistance on the bubble (F_z) is equal to the net driving force (F). The velocity of film thinning becomes:

$$v_h = \frac{dh}{dt} = \frac{F}{6\pi\mu R_b^2} h \quad (\text{C-20})$$

Induction time can be estimated by integration of above equation. The integration range starts from an initial distance between the bubble and collector, to a critical thickness, h_{cr} . The critical thickness is the distance at which the liquid film ruptures spontaneously.

$$t_{\text{induction}} = \int_{h_o}^{h_{cr}} \frac{6\pi\mu R_b^2}{F} \frac{dh}{h} \quad (\text{C-21})$$

$$t_{\text{induction}} = \frac{6\pi\mu R_b^2}{F} \ln\left(\frac{h_{\text{cr}}}{h_o}\right) \quad (\text{C-22})$$

This model is useful for the evaluation and analysis of the induction time without considering surface forces.

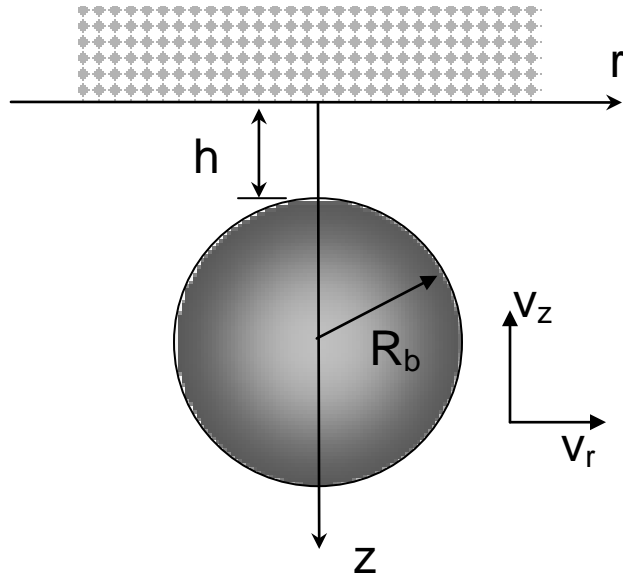


Figure C.1 Schematic of gas bubble approaching a planar collector surface.